HAL
open science

Semiconductor nanowires for ultimate magnetic objects : growth mechanism

Marta Orrù

To cite this version:

Marta Orrù. Semiconductor nanowires for ultimate magnetic objects : growth mechanism. Materials Science [cond-mat.mtrl-sci]. Université Grenoble Alpes, 2017. English. NNT : 2017GREAY061 . tel-01743730

HAL Id: tel-01743730

https://theses.hal.science/tel-01743730v1

Submitted on 26 Mar 2018

HAL is a multi-disciplinary open access archive for the deposit and dissemination of scientific research documents, whether they are published or not. The documents may come from teaching and research institutions in France or abroad, or from public or private research centers.

L'archive ouverte pluridisciplinaire **HAL**, est destinée au dépôt et à la diffusion de documents scientifiques de niveau recherche, publiés ou non, émanant des établissements d'enseignement et de recherche français ou étrangers, des laboratoires publics ou privés.

Communauté UNIVERSITÉ Grenoble Alpes

THÈSE

Pour obtenir le grade de

DOCTEUR DE LA COMMUNAUTÉ UNIVERSITÉ GRENOBLE ALPES

Spécialité : **NANOPHYSIQUE**

Arrêté ministériel : 25 mai 2016

Présentée par

Marta ORRU

Thèse dirigée par **Joël CIBERT** et
codirigée par **Edith BELLET-AMALRIC**

préparée au sein de **l'équipe mixte CNRS-CEA Nanophysique et Semiconducteurs à l'Institut Néel, à l'INAC,**
et à **l'École Doctorale de Physique de Grenoble**

Nanofils semiconducteurs: vers des objets magnétiques ultimes, mécanisme de croissance

Thèse soutenue publiquement le **26 Septembre 2017**,
devant le jury composé de :

Dr. Thierry BARON
Directeur de recherche CNRS, CEA, LETI, Grenoble, Président du jury
Dr. Silvia RUBINI
Chargé de recherche IOM-CNR, Trieste, Rapporteur
Dr. Michel GENDRY
Directeur de recherche CNRS, INL Lyon, Rapporteur
Dr. Frank GLAS
Directeur de recherche CNRS, C2N, Marcoussis, Examinateur

Acknowledgments

Well, the time has come for acknowledgments. :)

First I would like to thank my supervisors Edith Bellet-Amalric and Joël Cibert for giving me the opportunity to prepare my PhD in Grenoble. During these three years they never stopped motivating me. They always had time for meetings, guiding me with positive and rich discussion all the time of research and also during the manuscript redaction.

A very special gratitude to labex-LANEF for funding this project.

I would like to thank all the people involved in the characterization of the samples: David Ferrand, Fabrice Donatini, Gilles Nogues, Mathieu Jeannin, Alberto Artioli and Kimon Moratis for optics and a big thank to Martien den Hertog, Eric Robin, Catherine Bougerol and Nicolas Mollard for TEM.

Working in NPSC group has been very fruitful for my experience, I spent a very good time during these three years and I would like to thank all the people in the group, in particular Regis André, Serge Tatarenko, Henri Mariette for discussion and feedback about MBE growth. A big thanks also for their technical support to Didier Boilot, Yann Genuist, Yoann Cure, and Jean Dussaud also for sharing his office with me. Lucien Notin for help at AFM and Eva Monroy for the training at microbonding at INAC.

I would like also to thank people who trained me at the Nanofab clean-room and helped me with technical issues, in particular Thierry Crozes, and all the technical staff in Nanofab. And for their help and fruitful discussion about electrical measurements Laurent Villa, Cyril Beigne, Fabrice Donatini, Yann Genuist, Moïra Hocevar.

Also thanks to all the nice people I had the chance to meet, in particular Thibault Cremel, again Alberto Artioli, Mathieu Jeannin and Kimon Moratis, Daria Beznasiuk for good time at Montpellier MBE conference, Zihua Fang, Caroline Lim, Anna Moutkarova, Luca Readelli, Siew Li Tan, and all the PhD students and post-docs.

I am also grateful to my family and friends, and Alessandro for his moral support through writing this thesis and my life in general.

Résumé en français

Le concept fondamental de la nanospintronique à base de semi-conducteurs repose sur la possibilité de combiner les propriétés magnétiques du spin de l'électron avec les propriétés électriques des semi-conducteurs au sein d'une nanostructure unique. Cette possibilité ouvre la voie à la réalisation d'un quantum bit, c'est-à-dire un dispositif pour le contrôle de l'état de spin d'un électron ou d'un état cohérent de plusieurs spins.

Une possible méthode pour implémenter ce type de dispositif est la préparation de semi-conducteurs magnétiques dilués par l'introduction dans le semi-conducteur de métaux de transition appropriés, tels que le Mn, à faible concentration. Parmi les semi-conducteurs magnétiques dilués les plus connus figurent le (Ga, Mn)As et le (Cd, Mn)Te. Le dopage électrique de type p induit dans ces matériaux un état ferromagnétique par interaction d'échange entre les trous et les spins, avec une température de Curie de 200K pour le (Ga, Mn)As [1] et 3K pour le (Zn, Mn)Te [2]. Par rapport au matériaux III-V, l'avantage des semi-conducteurs magnétiques dilués II-VI est que le dopage électrique et magnétique peuvent être maîtrisés séparément, parce que les ions de Mn ne sont pas des dopants électriques.

Toutefois, quand les dimensions d'un objet ferromagnétique sont réduites au niveau du nanomètre, on atteint la limite super-paramagnétique: les spins peuvent aléatoirement changer d'état entre *up* et *down*, résultant en un état paramagnétique, au-dessus d'une temperature de blocage. La réalisation d'un semi-conducteur magnétique dilué de dimension nanométrique demande donc le confinement des trous par la structure de bande du semi-conducteur, ainsi que le contrôle de l'anisotropie par la déformation de la structure cristalline. Parmi un grand nombre de nanostructures qui font l'objet de recherche, les nanofils semi-conducteurs représentent un choix intéressant. Ils peuvent être fabriqués par méthode bottom-up avec des techniques de déposition de vapeur comme l'épitaxie par jets moléculaires, utilisée ici. La croissance axiale est favorisée par une nanoparticule de catalyseur métallique permettant de composer des hétérostructures en alternant différents semi-conducteurs. La géométrie des hétérostructures peut être axiale, avec un changement de matériau dans le sens vertical, ou radiale, par la croissance de structures cœur/coquille.

Le nanofils de semi-conducteurs II-VI représentent un système modèle pour la réali-

sation de ces structures parce que les hétérostructures axiales permettent un confinement des charges (boîte quantique), et celles radiales (cœur/coquille) permettent de contrôler la déformation.

A l'état actuel de la recherche sur les nanofils, les majeurs défis sont la maîtrise de la croissance des hétérostructures et le contrôle du dopage électrique. Dans ce contexte, mon travail de Thèse s'est focalisé sur trois principaux axes de recherche : la croissance par épitaxie par jets moléculaires des nanofils de ZnTe catalysés par des nanoparticules d'Au, la maîtrise du rapport de forme des boîtes quantiques de CdTe inséreés dans les fils de ZnTe, et le dopage azote des fils de ZnTe.

Ce manuscrit est organisé en quatre chapitres :

Le Chapitre 1 résume les propriétés des semi-conducteurs II-VI et des semi-conducteurs magnétiques dilués. La méthode de croissance par épitaxie par jets moléculaires est également expliquée, ainsi que les principales techniques de caractérisation utilisées dans ces travaux.

Le Chapitre 2 est dédié à la croissance des nanofils de ZnTe. La méthode de croissance est vapeur-solide-solide en partant de catalyseurs solides d'or. Il a été démontré que la préparation de ces catalyseurs a une grande influence sur la dispersion des temps d'incubation de fil à fil au sein du même échantillon: quand les nanoparticules d'or sont préparées sous vide, la variabilité de longueurs des nanofils est de l'ordre de 10. Pendant mes travaux j'ai proposé une nouvelle méthode basée sur la préparation du catalyseur d'Au sous flux de Zn. Ceci a supprimé la variabilité des temps d'incubation, réduisant la dispersion des longueurs sur un même échantillon à un facteur 2, et augmentant le taux de succès des fils verticaux de 20% à 80%. Des mesures complémentaires de diffraction des rayons X ont fourni des informations supplémentaires sur l'importance de l'orientation relative entre le catalyseur d'Au et le substrat ZnTe(111)B.

Le Chapitre 3 porte sur la croissance des boîtes quantiques de CdTe dans les nanofils ZnTe. Le rapport de forme des boîtes quantiques de CdTe est un moyen pour maîtriser leur état fondamental (entre trou léger et trou lourd). Ceci peut être obtenu en contrôlant le temps de croissance des boîte quantiques, mais demande (1) la suppression de la croissance latérale (responsable de la formation de boîtes parasites) et (2) la reproductibilité d'un échantillon à l'autre, basée sur une maîtrise de la température de croissance avec une précision meilleure que 10 degrés. Ceci a été validé dans nos conditions de croissance par une étude croisée de croissance d'hétérostructures de ZnTe avec multiples boîtes quantiques de CdTe et de caractérisation par microscopie électronique à transmission. Les résultats expérimentaux sont comparés avec un modèle prenant en compte la géométrie des flux de croissance et une possible re-évaporation du Cd depuis le cata-

lyseur ou du CdTe par les parois du nanofil.

Le dopage azote des nanofils de ZnTe /ZnTe:N cœur/coquille est présenté au Chapitre 4. La méthode de dopage avec un plasma azote pendant la croissance est très efficace pour le dopage des couches de ZnTe. Mon travail a initialement consisté à mettre au point cette même méthode pour les nanofils ZnTe, mais la morphologie des nanofils en a été lourdement perturbée au point de bloquer la croissance axiale. La solution utilisée a été donc une géométrie des nanofils cœur/coquille, avec dopage azote seulement pour cette dernière. Je présenterai les résultats des croissances par épitaxie par jets moléculaires et des caractérisations des nanofils de ZnTe /ZnTe:N cœur/coquille. Des transistors à effet de champ basés sur des nanofils isolés ont été preparés pour la caractérisation électrique. Nous avons obtenu des fils de ZnTe/ZnTe:N cœur/coquille présentant des densités de charges de 6×10^{18} trous/cm^3 à température ambiante, du même ordre que la densité critique de Mott pour le ZnTe.

Introduction

Semiconductor nanospintronics is based on the possibility to combine the magnetic properties of the electron spin and the properties of semiconductors (electronics functions) in a single nanostructure. As an example, controlling a single electron in a quantum dot (QD) opens the way towards the realization of devices for the manipulation of a single spin (quantum computing), using as a quantum bit the electron spin, or a coherent superposition of up and down states. With optical manipulation in mind, the selection rules of the electron-hole recombination must be fully controlled, and this requires a complete control of the hole envelope function.

A different approach consists in preparing diluted magnetic semiconductors (DMS), introducing an appropriate transition-metal (such as Mn) at a level of a few per cent. The most studied DMS are (Ga, Mn)As and (Cd, Mn)Te, where Mn is substituted to Ga or Cd. P-type carrier-controlled ferromagnetism in Mn-doped semiconductors has been observed in III-V (in GaMnAs with a critical temperature of 200K [1]) and in II-VI (in ZnMnTe with a critical temperature of 3K [2]). The advantage of II-VI DMS with respect to III-V DMS compounds is that the Mn ions are not electrical dopants, allowing us to control separately the electrical doping (hole concentration) and the Mn concentration. However, shrinking the dimensions of ferromagnetic DMS, would lead to the so-called *super-paramagnetic limit* where magnetization can randomly flip direction, above a blocking temperature. The spin carriers interactions in nano-DMS must be optimized, and this requires an efficient method to confine the holes (band engineering) and to control the anisotropy (strain engineering) in order to block the polarization.

Among the variety of nanostructures that are investigated nowadays, semiconductor nanowires (NWs) have attracted great attention since the 2000's, due to their potential applications. Semiconductor NWs can be prepared by a bottom-up approach using vapor deposition techniques, where a metal catalyst promotes the axial growth using the so-called vapor-liquid-solid or vapor-solid-solid method (named after the liquid or solid state of the metal catalyst). This technique allows the growth of new heterostructures, with the possibility to combine materials even with a high lattice mismatch. NW heterostructures are called axial if the composition is changed along the axial direction, like in NWs embedding an insertion of another semiconductor material at some point

along the length, or radial, like in core/shell heterostructures. Making a QD (axial heterostructure) requires nevertheless controlling both axial and radial growth.

II-VI semiconductor NWs are thus a model system offering the possibility to engineer the wavefunction, with the realization of axial heterostructures for the confinement of charge carriers, and the strain, using radial heterstructures, in well-chosen heterostructures containing the magnetic impurities. However, this requires an optimal growth of NW-based heterostructures, and the possibility to control the doping level, which is a major challenge in present NW research.

In this context, my PhD project has been devoted to three main investigation axes: the growth by molecular beam epitaxy of Au-catalyzed ZnTe NWs, the control of the aspect ratio of CdTe QDs embedded in ZnTe NWs, and the nitrogen doping of ZnTe NWs. The outline of this manuscript is the following:

Chapter 1 presents very shortly the properties of II-VI semiconductors and of diluted magnetic semiconductors. Molecular beam epitaxy, used for the growth of NWs is also presented, as well as the main characterization techniques used in this work.

Chapter 2 is devoted to the growth of ZnTe NWs. ZnTe NWs are grown in the vapor-solid-solid growth mechanism, as observed by in-situ RHEED. The gold catalyst preparation is important to control the incubation time. In particular the problem of an incubation time different from NW to NW has been evidenced upon preparation of the gold catalyst by dewetting under vacuum, leading to a factor of more than 10 in the length dispersion on the same sample. A method of preparation of gold particles under Zn flux is demonstrated to solve this problem, leading also to the improvement of the yield of vertical NWs from 20% (for preparation of gold under vacuum) up to 80% (for preparation of gold under Zn flux). X-ray diffraction measurements confirm that with both methods the gold catalysts are in epitaxy with the ZnTe (111)B substrate, but the main relative orientation with respect to the ZnTe(111)B growth substrate is different in the two cases.

Chapter 3 is dedicated to the systematic study of the growth of CdTe QDs in ZnTe NWs. The aspect ratio of CdTe QDs is an important way to control the QD ground state (between light hole and heavy hole). Since the diameter is fixed by the contact area of the catalyst with the NW, we can control the length by changing the growth time of the QDs, but it also requires (1) the suppression of the lateral growth (giving parasitic QDs) and (2) a precise control of the growth temperature within 10°C. This was demonstrated in our growth conditions with a coupled study of growth of multi-QD-NW CdTe-ZnTe heterostructures and of TEM and EDX characterization. The results are discussed using a geometrical model taking into account the flux geometry in our growth chamber, but

also the re-evaporation of Cd from the catalyst and of CdTe from the NW sidewalls in our temperature range.

Chapter 4 is concerned with the doping of ZnTe:N NWs using Nitrogen plasma. This method is very efficient for the doping of 2D layers of ZnTe grown by molecular beam epitaxy. My initial target was to adapt this same method for NW doping, but the morphology of ZnTe NWs is affected when the growth is done in presence of the Nitrogen plasma. The solution we adopted was the growth of core/shell ZnTe NWs with a nitrogen doped shell. Thanks to the method of preparation of gold catalyst under Zn flux explained in Chapter 2, with a yield of 80% of vertical NWs, core/shell ZnTe/ZnTe:N NWs have been grown. The results of the growth and characterization of nitrogen doped ZnTe/ZnTe:N core/shell NWs will be presented. Single NW based field-effect transistor were realized by electron beam lithography for electrical characterization. The doping level has been estimated from room temperature characterization of single nanowire-based field-effect devices. We were able to obtain ZnTe/ZnTe:N core/shell NWs showing a p-type carrier density of 6×10^{18} holes/cm^3 at room temperature, of the same order as the Mott critical density in ZnTe.

Contents

Acknowledgments **iii**

Résumé en français **v**

Introduction **ix**

1 Properties of II-VI semiconductors and methods **1**
1.1 Properties of II-VI semiconductors 2
1.1.1 Diluted magnetic semiconductors 2
1.1.2 State of the art of II-VI nanowires 4
1.2 Molecular Beam Epitaxy 6
1.2.1 The II-VI MBE facility 6
1.2.2 The nitrogen plasma source 8
1.2.3 Reflection High Energy Electron Diffraction 9
1.3 Characterization techniques 10
1.3.1 Scanning electron microscopy 10
1.3.2 Transmission electron microscopy 11
1.3.3 Energy-Dispersive X-ray spectrometry 12

2 Growth of ZnTe nanowires **15**
2.1 ZnTe NW growth by molecular beam epitaxy 16
2.1.1 Substrate preparation 16
2.1.2 Gold catalyst preparation 17
2.1.3 The VSS growth of ZnTe NWs 20
2.2 The problem of incubation time 26
2.2.1 The marker technique 26
2.3 Dewetting under Zn flux 30
2.3.1 Series A 30

2.3.2 Series B 32
2.3.3 Series C 34
2.4 XRD measurements on gold catalyst 38
2.5 Conclusion 41

3 Growth of ZnTe/CdTe nanowire/quantum dot heterostructures 43
3.1 Introduction 44
3.2 Growth by molecular beam epitaxy of ZnTe/CdTe NW/QD 45
3.3 Characterization of thin CdTe QDs 49
3.4 Growth of CdTe QDs as a function of temperature 53
3.5 Growth of CdTe QD as a function of time 60
3.6 Discussion and conclusion 64

4 Doping of ZnTe nanowires with nitrogen Plasma 73
4.1 Overview 75
4.2 Doping of ZnTe(100) 2D layers 75
4.3 Effects of doping on the morphology of ZnTe NWs 77
4.3.1 Growth of ZnTe:N NWs 77
4.3.2 Effects of the nitrogen plasma on the growth mechanism 79
4.3.3 Growth of core/shell ZnTe/ZnTe:N NWs 83
4.3.4 Photo-luminescence of core/shell ZnTe/ZnMgTe:N NWs 84
4.4 Fabrication of NW-FET 86
4.5 Characterization of core/shell ZnTe/ZnTe:N NWs 90
4.5.1 Model of the NW-FET 90
4.5.2 The 4-probe method 91
4.5.3 Resistance along a cone-shaped NW with 4 contacts 93
4.5.4 Growth conditions of ZnTe/ZnTe:N core/shell NWs 95
4.5.5 Measurements on the nominally undoped ZnTe NWs reference sample 95
4.5.6 Measurements on the ZnTe/ZnTe:N NWs with shell growth temperature of 350°C 97
4.5.7 Measurements on the ZnTe/ZnTe:N NWs with shell growth temperature of 290°C 99
4.6 Discussion and conclusion 103

Conclusions and Prospects 105

Appendices 109

Appendix A 111

Appendix B 113

CHAPTER 1

Properties of II-VI semiconductors and methods

Contents

1.1 Properties of II-VI semiconductors **2**

1.1.1 Diluted magnetic semiconductors 2

1.1.2 State of the art of II-VI nanowires 4

1.2 Molecular Beam Epitaxy **6**

1.2.1 The II-VI MBE facility 6

1.2.2 The nitrogen plasma source 8

1.2.3 Reflection High Energy Electron Diffraction 9

1.3 Characterization techniques **10**

1.3.1 Scanning electron microscopy 10

1.3.2 Transmission electron microscopy 11

1.3.3 Energy-Dispersive X-ray spectrometry 12

This Chapter gives a short overview of the basic properties of II-VI semiconductors in section 1.1, introducing the concept of diluted magnetic semiconductors and magnetic polaron. The state of the art of II-VI NW growth and more particularly of ZnTe NWs is presented in section 1.1.2. The second part is dedicated to the methods used in this work: in section 1.2 we will present molecular beam epitaxy growth method, and a related important in-situ characterization technique in section 1.2.3. Then electron microscopy based characterization methods will be presented in section 1.3. Concerning NW doping, the electrical characterization of NWs is explained in Chapter 4.

1.1 Properties of II-VI semiconductors

II-VI semiconductors have important applications for various optoelectronic devices such as light-emitting diodes and laser diodes operating particularly in the green spectral range, and photovoltaic cells. Wide-bandgap II–VI compounds such as ZnSe, CdSe, ZnTe, and CdTe (see Fig. 1.1) have a direct bandgap, with energy in the visible range. The use of ternary compounds allows one to tune their light-emission properties over a continuous range of band gap energies, as shown in Fig. 1.1. In their bulk form, the stable crystal structure can be either zinc-blende (ZB) (ZnSe, ZnTe, CdTe) or wurtzite (ZnO), or the two can be stable (ZnS, CdS, CdSe). For ZnTe nanowires instead both crystal structures are stable [3].

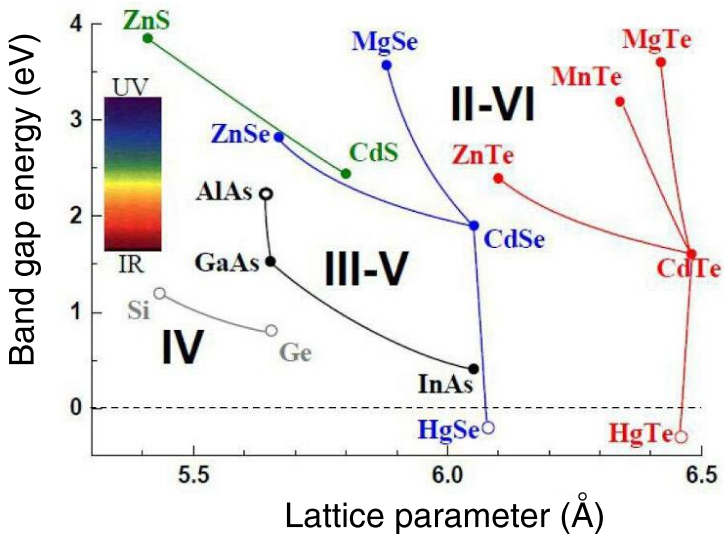

Figure 1.1: Band gap energy at T= 4K as a function of the lattice parameter for different II-VI semiconductors from [4]. Filled and empty symbols correspond respectively to semiconductors with direct and indirect band gap.

For this work, we considered Tellurides (Te based compound semiconductors), in particular ZnTe and CdTe with direct band gap of 2.26 eV and 1.44 eV respectively at room temperature.

1.1.1 Diluted magnetic semiconductors

Diluted magnetic semiconductors (DMS) are semiconductor compounds ($A_{1-x}Mn_xC$) obtained when a fraction of the cations is substituted by a magnetic impurity (usually Mn). This class of semiconductors are attracting great attention as candidates for semiconductor-based spintronics for two reasons: (1) the usual properties of the semiconductor are preserved (such as electrical doping, electrical transport, optical properties, and the possibility to fabricate heterostructures and nanostructures combining several semiconductors); (2) hole-mediated ferromagnetism appears with p-type doping.

The most studied DMS are (Ga, Mn)As and (Cd, Mn)Te, where Mn is substituted to Ga or Cd. Since (Ga, Mn)As is ferromagnetic and can be inserted into semiconductor devices, several functions of spintronics have been realized already. Carrier controlled ferromagnetism in Mn-doped semiconductors has been observed in III-V (in GaMnAs with a critical temperature of 200K [1]) and in II-VI (in ZnMnTe with a critical temperature of 3K [2]). One objective is now to reduce the size of the active DMS. With that in mind, II-VI DMS have two advantages with respect to III-V's :

- while the Mn impurity in GaAs is both magnetically and electrically active (Mn substituting Ga in GaAs is an acceptor), Mn substituting Cd or Zn in a II-VI does not dope the semiconductor. This allows us to control separately the carrier concentration (e.g. by nitrogen doping) and the introduction of magnetic impurities.

- while the Mn impurity is introduced into III-V's with difficulty - by epitaxy at very low temperature, much lower than the temperatures used for the growth of nanostructures such as quantum dots and nanowires - Mn can substitute Cd or Zn in a II-VI up to 100% Mn, using molecular beam epitaxy at temperatures suitable for the growth of nanostructures.

As a result, the fabrication of ultimate magnetic objects based on a modulation-doped (nitrogen in the barriers), electrically controlled (FET structure), quantum dot incorporation a II-VI DMS (CdMnTe) appears feasible. A quantum dot containing one or a small number of carriers will be much easier to control electrically than a metallic ferromagnetic cluster of the same size. First examples of quantum dots exhibiting a magnetic polaron (few % Mn) [5, 6] or even a single Mn atom [7, 8] have been fabricated using the so-called Stranski-Krastanow method.

The magnetic polaron is formed due to the interaction of a carrier, for instance from optically created exciton (electron-hole pair) as in Ref. [9], with the localized spins, creating a local magnetization. The optical properties of the magnetic polaron have been studied in 3D, 2D and single QD DMS [4, 9]. Fig. 1.2 illustrates this concept. Stranski-Krastanow process severely limits the combination of materials and the shape of quantum dots, and the built-in strain. Quantum dots in nanowires are more flexible.

Very important progress has been done in the growth of NWs including QDs, providing huge flexibility in the engineering of strain in the quantum dot: both unstrained and strained quantum dots can be designed; the strain is obtained by the proper design of a shell layer around the structure, and can thus be tuned quite freely. A few groups have started to grow nanowires incorporating (Ga,Mn)As, but the growth of such objects is difficult since the growth conditions adapted to the fabrication of nanowires (high temperature, $>500°C$) and the incorporation of Mn (low temperature, $<250°C$) are not compatible. The fabrication of (CdMnTe) quantum dots in ZnTe NWs have been achieved in the group [10], demonstrating the possibility to obtain the formation of magnetic polaron [9] with engineering of confinement and strain thanks to the presence of a

ZnMgTe shell around the (CdMnTe) quantum dot.

Our results, and those of our Warsaw group[11], have demonstrated both the great potential of these nanostructures and the need to achieve a precise control of their growth.

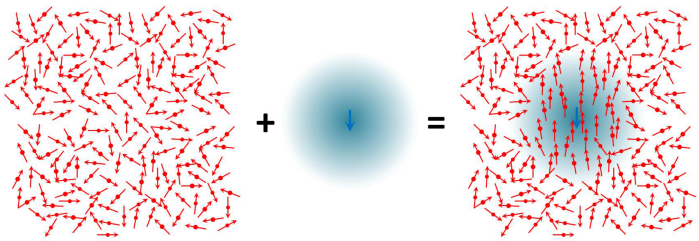

Figure 1.2: Illustration of the magnetic polaron formation from [10]

1.1.2 State of the art of II-VI nanowires

As stated previously II-VI based nanowires structures offer many advantages when dealing with the engineering of the wavefunctions.

When analyzing the state of the art on II-VI based NWs, most of the studies concern binary semiconductor compound NWs ZnO, ZnS, CdS, CdSe studied mainly for photonics, with an emphasis on photovoltaics and light emission (electroluminescence). In contrast the reports on the growth of ZnTe nanowires are relatively limited.

ZnTe NWs are generally grown via chemical methods using metal-catalyst particles. It includes physical vapor solid transport [12, 13, 14, 15], metal organic chemical vapor deposition [16], metal organic vapor phase epitaxy [17], electro-chemical deposition [18], and MBE [19, 20, 3]. Only few groups in the world are involved in MBE tellurides NWs growth: The Polish Academy of Science in Warsaw and our group.

The optimal temperature for the growth of II-VI thin films with high optical quality is between 300 and 350°C, however most of the reported growth temperatures of ZnTe Au-catalyzed NWs are above 500°C which is usually detrimental to the NWs optical properties [21].

To lower the growth temperature different approaches were used. One possibility is to use a different catalyst in order lower the eutectic temperature as for example including Sn[17]. Another choice is to grow the NWs directly on GaAs or Si which gives rise to Ga-Au (340°C) or Au-Si (363°C) eutectic alloys. This option is used by the Polish group. They reported the growth of high density ZnTe NWs along different orientations of the GaAs substrates [19, 20]. The NW growth is performed under Zn-rich conditions in the 360-450°C range using elemental cells: Zn and Te sources. The NWs grow preferentially along the <111> axis independently of the substrate orientation with a diameter over 20nm. However the presence of Ga in the Au nanoparticle can be a source of impurities during the growth. All the nanowires grown by this group as well as with the other techniques exhibit a Zinc-blende structure.

As started with the work of Pamela Rueda-Fonseca, the approach in our group is different. First we chose to grow the NWs on a thick ZnTe (111)B buffer layer (over 200 nm) to separate the Au nanoparticles from the GaAs(111)B substrate. Second we use a ZnTe effusion cell to explore the growth conditions close to stoichiometry, by adding an additional flux with elemental cells [3]. Finally we deposit a very thin gold layer in order to lower the density and the diameter of the NWs. Low temperature growth conditions (350°C) and a control of the cation: anion flux ratio allows us to grow nanowires with different morphologies (cone or cylinder-shaped NW) which correspond to different crystal structures (Zinc-blende or Wurtzite).

Concerning the axial (Cd,Mn)Te/ZnTe or radial ZnTe/ZnMgTe NW heterostructures only our group and the group of Warsaw have published results. In the case of the Polish group the ZnMgTe shell is grown at much lower temperature (-100/-150°C) with respect to the NW. The shell thickness is in the range of 30 nm and mainly in epitaxy with the core but other orientations are also observed due to the low growth temperature[22] and the sidewalls are rough.

CdTe nanowires have also been grown under various conditions such as close–space sublimation [23] and MBE [24] with a particularly large Cd and Te flux.

For the CdTe insertions the results from our group will be presented in Chapter 3 and an analysis of the growth mechanism is performed.

To grow the CdTe insertion the Polish group systematically decreases the substrate temperature from 40 to more than 100°C. For the higher temperatures a significant Zn, Cd intermixing at the interfaces is observed [25] which is most likely related to the vapor-liquid-solid mechanism with a high Cd-Zn content in the droplet. By reducing the temperature of the CdTe segment a change from an axial to a radial growth occurs with a coexistence of both growth directions for intermediate temperatures[26]. The insertions have a diameter of about 50 nm and an aspect ratio ranging from 1 to 2. For long insertions a kink is observed in some cases but the CdTe is always defect free.

1.2 Molecular Beam Epitaxy

Molecular Beam Epitaxy (MBE) is an ultra high vacuum crystal growth technique used to prepare epitaxial films. Epitaxy (from from the Greek $\epsilon\pi\iota$, meaning 'above', and $\tau\alpha\xi\iota\varsigma$, meaning 'in ordered manner') is the process in which a crystalline film is formed over a crystalline substrate as the result of deposition of new material. During MBE growth one or more thermal beams of atoms or molecules react with a heated crystal surface under ultrahigh-vacuum (UHV) conditions, with total pressure of the order of 10^{-10} Torr. The most important surface processes occurring during epitaxial growth by MBE are: adsorption of the atoms or molecules impinging on the substrate surface; dissociation of the adsorbed molecules and surface diffusion of the adatoms; incorporation into the growing crystal; thermal desorption of the species non incorporated into the crystal lattice. Evaporation can take place concurrently.

1.2.1 The II-VI MBE facility

The MBE machine used to grow the samples studied in this work consists of an ensemble comprising a RIBER 32P II-VI chamber connected under UHV to a MECA2000 III-V chamber, a picture is in Fig. 1.3.

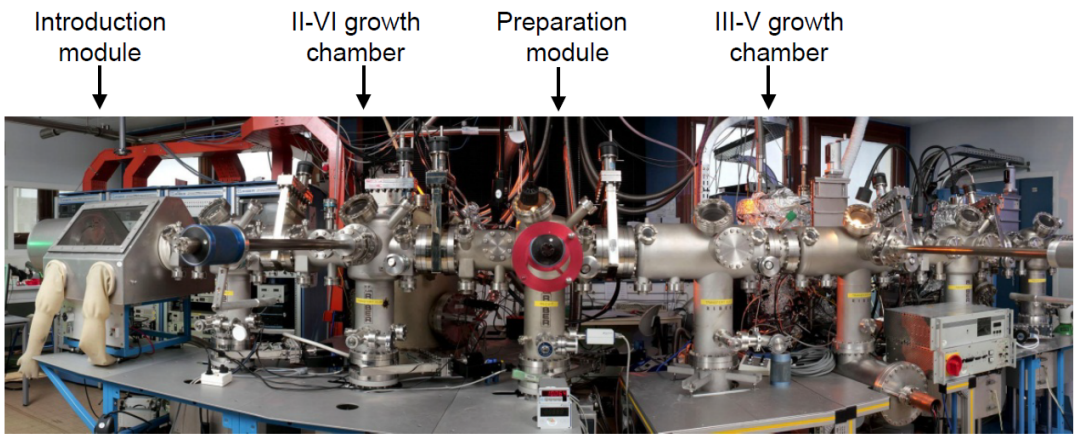

Figure 1.3: Picture of the II-VI and III-V MBE chambers, connected under ultra high vacuum, used for the epitaxial growth of the samples in this manuscript.

The II-VI MBE chamber is dedicated to the growth of tellurides and selenides, a scheme is presented in Fig. 1.4. The III-V chamber is dedicated to the deoxidation process of GaAs substrates and it contains an Au effusion cell that is used for the deposition of a thin layer of Au (to form the catalyst particles).

- different source cells that supply all atoms necessary for the growth and the doping of the semiconductors, are disposed radially in front of a heated substrate. In our Riber 32P MBE chamber there are 8 solid source cells and the nitrogen plasma source 1.4. Source material purity is extremely important, so rigorous outgassing procedures are essential after any air exposure.

- Each cell is provided with an externally controlled mechanical shutter for rapid changing of the beam species, so as to alter abruptly the composition of the growing film.

- Thermal insulation among cells is ensured by the use of a liquid nitrogen cryopanel. Also the chamber walls are covered with another liquid nitrogen cryopanel to provide secondary pumping of the active residual gases. The composition of the background vacuum (pressure in 10^{-11} Torr range) is controlled using a mass spectrometer.

- The substrate holder provides heating to the substrate, and it enables its rotation in its plane. The rotation of the substrate during growth is important to average out any deviation in thickness uniformity. In the back of the substrate manipulator an ion gauge is usually mounted, such that either the gauge or the substrate, but not both simultaneously, can be rotated in front of the cells. When the ion gauge is rotated in front of the heated cells, it is used for the measurement of the incident beam flux.

- the substrate itself is usually glued on the Moly-block with liquid In (GaAs wafer) or Ga (II-VI wafer) by surface tension, providing excellent heat transfer. The Moly-block is a Mo metal block which is heated by radiation. The sample temperatures are measured by a thermocouple in direct contact with the Moly-block. The major requirement is that the temperature across the substrate is uniform and reproducible to within $\pm 5°$C. Nevertheless possible temperature variations form one Moly-block to another have to be taken into account.

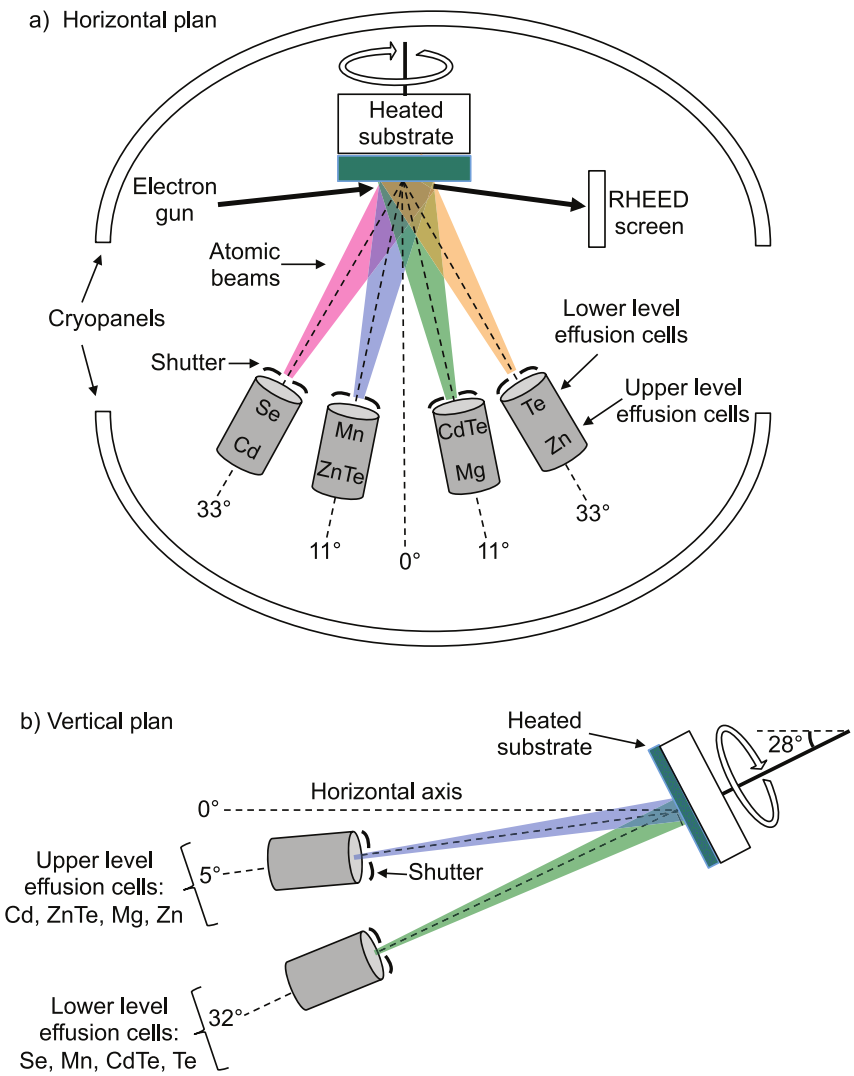

Figure 1.4: Scheme of the II-VI MBE chamber used for in this work. The angles of the effusion cells with respect to the sample normal are indicated. Scheme taken from [10].

1.2.2 The nitrogen plasma source

The nitrogen plasma source is mounted in the viewport at 0° of Fig. 1.4, it is constituted of the following parts:

- the source itself thermalized by the water circulation;
- a flux valve with a vernier control mechanism;
- an impedance;
- a RF generator;
- a N_2 introduction valve connected to a mass flow.

The plasma discharge is realized in the cavity with N_2 supply by an inductive circuit cooled by water. The plasma cavity has holes allowing to species formed in the plasma

to effuse towards the valve. The valve can move forward or backward to control the flux. The source is fed by a commercial RF generator RFX600.

1.2.3 Reflection High Energy Electron Diffraction

RHEED provides several types of information about a surface: its crystallographic symmetry (from the symmetry of the diffraction pattern), the extent of long-range order (from the sharpness of the pattern), and whether growth is proceeding in a 2D or a 3D mode. Both MBE chambers are equipped with a Reflection High Energy Electron Diffraction (RHEED). A mono-energetic beam of electrons of high energy (30 keV) is directed at grazing incidence (0.5°-3.0°) toward the sample surface. The electrons penetrate a few layers into the surface, giving the diffraction pattern of the surface lattice. The experimental setup requires only an electron gun and a fluorescent screen. The pattern image is then captured by a CCD camera. Examples of RHEED patterns are shown in Fig.s 2.1 and 2.5. In the MBE growth chamber, RHEED is used for monitoring:

1. the thermal cleaning of the substrate surface before growth,
2. the initial stages of epitaxial growth,
3. the changes in the surface structure when the growth conditions are changed.

One of the most important applications of RHEED is measuring the growth rate for layer-by-layer epitaxy. RHEED oscillations are used to determine growth rates. The intensity of the 0-order diffracted beam is recorded as a function of time during growth. What is observed is an oscillating behavior of the intensity. An example is shown in Fig. 1.5, taken during the growth of GaAs(100). The maxima in the reflectivity correspond to atomically smooth surfaces, i.e. before deposition of a layer, and when deposition is complete. The reflectivity minima correspond to the most disordered surfaces. The period of the oscillations corresponds exactly to the growth time of a layer of GaAs in the [001] direction (i.e. one layer of Ga plus one layer of As). There is a decaying exponential decrease in intensity oscillations because the overall surface roughness gradually increases as more and more layers are deposited.

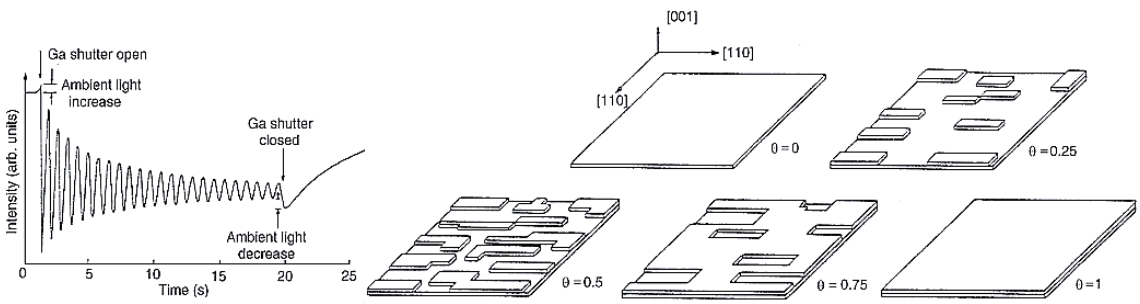

Figure 1.5: Growth rate of GaAs(100) by RHEED oscillations. θ is the fractional coverage.

1.3 Characterization techniques

The main characterization techniques used in this work are based on electron microscopy. Electron microscopy allows one to observe nanometer-sized objects using an electron beam as a probe. Depending to the electron beam acceleration voltage (between 1kV and 30 kV in scanning electron microscopy (SEM) and up to 300 kV in transmission electron microscopy (TEM)), the interaction of the beam with the sample produces: backscattered electrons, secondary electrons, Auger electrons, characteristic X-rays, and other photons of various energies. These signals can be used to study different properties, like surface topography, crystallography, chemical composition, and others, taking into account the different physical processes involved in their production. Fig.1.6 shows some of the signals that can be studied.

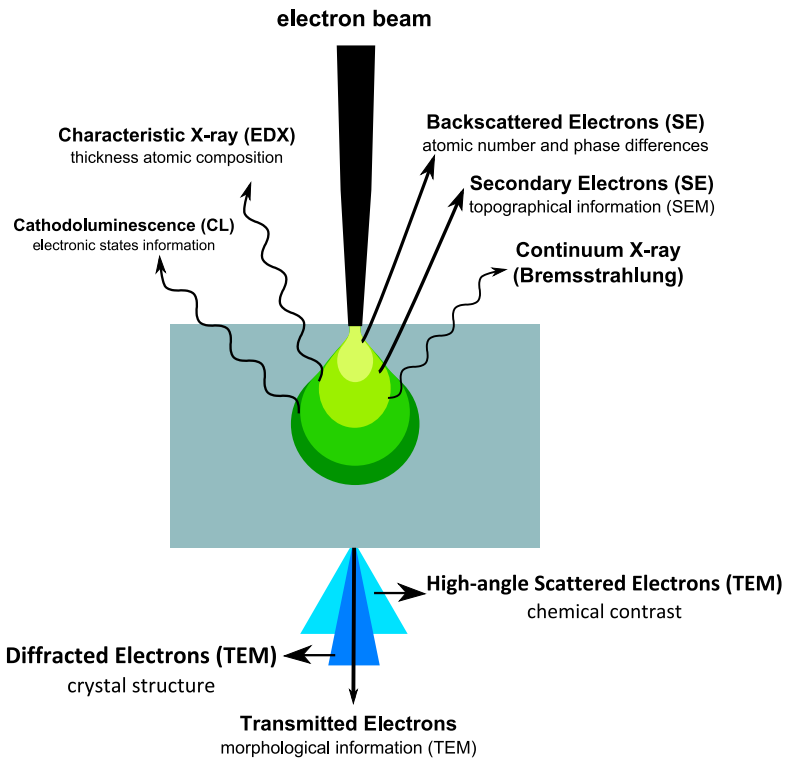

Figure 1.6: Simplified schematics of the interactions between an incident electron beam and a solid sample.

1.3.1 Scanning electron microscopy

In the scanning electron microscope (SEM) a finely focused electron beam is used as a probe. For the collection of images the probe is swept on a raster scan and point by point the signal coming from the sample is recorded as a gray value in a pixel. The energy of the electrons in the beam can be changed from 0 to 30 keV. The most interesting for imaging are the secondary and back-scattered electrons, because they are sensitive to differences in surface topography. Additionally, the contrast of the image generated

with secondary electrons is not only linked to the topography of the surface, but it is also linked to large changes in the chemical composition. For example, large changes in atomic number Z can produced a chemical contrast between the ZnTe NWs and the Au catalyst in top of them (Z_{Zn} = 30, Z_{Te} = 52 and Z_{Au} = 79).

The image magnification can be changed to have large view of the surface of the sample (useful to gain information on the distribution and density of the NW or Au particles) or a detailed information on the size and the morphology of individual objects (for example the Au particle or NW diameter). In this work we systematically observed as-grown samples using a SEM Zeiss U55 operated at 10kV and at a working distance of 4 mm. The resolution of this microscope is of the order of 1 nm. The SEM images were taken in top view or from the side of the sample (sample tilted at 65° and 90°).

1.3.2 Transmission electron microscopy

Transmission Electron Microscopy (TEM) is an essential tool for the characterization of the structural properties of the NWs. It allows us to determine: the NW crystal structure, their crystallographic direction, the NW dimensions with nanometric precision, the NW chemical composition and the possible presence of defects or twin boundaries. The acceleration voltage is up to 300 kV, and the sample thickness should be low enough (less than 100nm) so that electrons can completely traverse the sample.

In TEM the sample is illuminated with a parallel electron beam and an image of the illuminated zone is obtained whereas in STEM a small focused probe is scanned over the sample and the intensity on the detector at each point is recorded to form the image. TEM characterization allows one different imaging techniques: Bright-field (BF) detection consists in collecting transmitted electrons that have not been scattered nor diffracted (detector placed in the same axis as the microscope); in the Dark-Field (DF) detection mode the diffracted electrons are used (detector placed around the central detector); in High-Angle Annular Dark-Field (HAADF) electrons scattered at high angles are detected by an annular detector placed at a larger angle from the microscope axis. HAADF images show a chemical contrast since scattering at high angles is roughly proportional to the square of the atomic number of the element Z. Hence, heavier atoms have a signal more intense than lighter atoms (for example: Te atoms will be brighter than Zn atoms). Note that the diffraction pattern of the sample can also be observed.

Since the sample thickness has to be low, (S)TEM samples need a preparation. The most used way to prepare a nanowire sample is to disperse the nanowires on a holey carbon grid, by placing the grid on the as-grown substrate and move it around gently. This was used mostly for the preparation of samples for TEM-EDX studies (section 1.3.3).

To observe nanowires as-grown on the growth substrate in the TEM we used the cleaving method [27, 28] where a small wedge is cleaved or broken from the as-grown sample, and then it is sticked tilted to a Cu holder, so that the substrate surface is

parallel to the electron beam. This technique is relatively fast, and if the nanowires are in epitaxial relation with the substrate it is possible to align all of them simultaneously on the same zone axis. With this configuration, we are sure that no part of the nanowires is missing because it has been broken during the harvesting process. The disadvantages of this sample preparation is that long and/or thin nanowires may vibrate slightly under the electron beam far away from the substrate, this seems to be caused by electrostatic interaction between the (charged) sample and the electron beam. HRTEM is not possible under this conditions.

The High Resolution TEM (HRTEM) images presented in this work were acquired by Martien den Hertog (Fig.s 2.8 and 2.10) and Catherine Bougerol (Fig. 2.17).

1.3.3 Energy-Dispersive X-ray spectrometry

The Energy-Dispersive X-ray spectrometry (EDX) uses the X-ray spectrum emitted by the scattering of the electron beam. The spectrum is composed of the characteristic lines of the elements detected (allowing one to retrieve the chemical composition of the sample), and of a continuum background. Characteristic X-rays are generated when the interaction of the electron beam with the specimen atoms causes the ejection of another electron from an inner shell. The atom may relax radiatively to its ground state, with the emission of a X-Ray photon. Bremsstrahlung radiation is produced when the electrons are decelerated in the electric field of the sample atoms and the energy lost in the deceleration is emitted as a photon, forming a continuous spectrum (background under the characteristic peaks). Once a photon is created with a specific energy, it is impossible to determine whether it is a continuum or a characteristic X-ray. Thus, the background intensity sets a limit to the minimum amount of an element that can be detected.

A first qualitative analysis consists of identifying the lines observed on a raw spectrum of the sample (which element is present or not). As a result, EDX measurements are very useful to detect the presence and the location of the quantum dots inserted in NWs. Obtaining quantitative information needs instead complex analysis. EDX measurements of a NW deposited over a holey carbon grid are made in the form of hyper-maps, composed of an EDX spectrum for each pixel. The first step is to identify each peak and to determine and subtract the background. This is performed using the QUANTAX-800 software from BRUKER to obtain the net intensity of the characteristic X-rays (L-lines of Te and Cd, and K-lines of Zn and O) generated by the elements present along the beam axis (in the NWs presented here, we mainly detect: Te, Zn, Cd, Au, O).

The conversion of the net X-ray intensity into concentration, that is, quantification, was performed using the zeta-factor method [29, 30]. This analysis allows one to calculate the number of atoms per unit of length or the concentration of atoms of a specific element averaged under the beam path. This requires a calibration of the spectrum with respect to the intensity of reference samples, with well known thickness and concentra-

tion.

For each pixel i, the average concentration is $C_{i,j}$ of element j present along the beam axis is related to the net X-ray intensity $I_{i,j}$ by:

$$C_{i,j} = I_{i,j}\zeta_j A_{i,j} / \sum_{j^r=1}^{m} I_{i,j^r}\zeta_{j^r} A_{i,j^r} \tag{1.1}$$

with ζ_j the zeta-factor of the element j, and $A_{i,j}$ the absorption correction term for element j at pixel i. The zeta-factor ζ_j for the Te and Cd L-lines and the Zn and O K-lines are directly measured on the same equipment, at the same operating conditions, using the reference samples. The absorption correction terms $A_{i,j}$ are estimated from a simple model that takes into account the direction of the X-ray emission relative to the position of the detectors, knowing the thickness, density, and mass absorption coefficient of the material through which the radiation travels [30].

In the case of a core/shell nanowire, the cross section can be modeled by a series of nested ellipses, rectangles or hexagons[30]. The process for reconstructing the cross-section can be divided into three steps:

- first the appropriate cross sectional model is selected by comparing the thickness profile calculated from Eq. 1.1 with the thickness profile simulated for elliptical, hexagonal, and rectangular cross sections. For the NWs presented in Chapter 3, the hexagonal section gives the best fit. Then the orientation of the sample and the dimension of the first hexagon is adjusted to find the best fit to both profiles.

- second, the number of hexagons is determined, and their dimensions are evaluated from the concentration profiles. These estimates do not represent the final diameters but a first set of data for the simulation.

- third, the local concentrations are determined and the dimension of the hexagons adjusted by minimizing the compositional differences between the profiles calculated from Eq. 1.1 and simulated.

The EDX maps and the quantitative analysis presented in this work (Chapter 2 and 3) were done by Eric Robin. This technique allowed us to observe multicore-shell structures and to determine the shape, concentration and position of the CdTe QDs. The quantitative results obtained using this technique will be discussed in Chapter 3.

CHAPTER 2

Growth of ZnTe nanowires

Contents

2.1 ZnTe NW growth by molecular beam epitaxy 16
2.1.1 Substrate preparation 16
2.1.2 Gold catalyst preparation 17
2.1.3 The VSS growth of ZnTe NWs 20
2.2 The problem of incubation time 26
2.2.1 The marker technique 26
2.3 Dewetting under Zn flux 30
2.3.1 Series A 30
2.3.2 Series B 32
2.3.3 Series C 34
2.4 XRD measurements on gold catalyst 38
2.5 Conclusion 41

This chapter is devoted to the ZnTe NW growth by molecular beam epitaxy. A short introduction is given on the standard procedure used before this work in section 2.1. Then the evidences of the problem of a different incubation time from NW to NW are explained in section 2.2, and a new method for the preparation of the gold catalyst is proposed in section 2.3. The last section 2.4 is dedicated to complementary XRD measurements on the gold catalyst.

2.1 ZnTe NW growth by molecular beam epitaxy

The growth procedure of ZnTe NWs by molecular beam epitaxy was firstly investigated in the NPSC group by Pamela Rueda-Fonseca during her Ph.D.[10, 3, 31]. In this section I recall the standard procedure for the NW growth that I used at the beginning my project. It consists of three subsections about substrate preparation 2.1.1, the formation of gold catalyst by dewetting 2.1.2, and ZnTe NW growth 2.1.3.

As stated previously in order to master the complex axial/radial nanowires based structures it is essential to control and understand the growth mechanism of the Au-catalyzed ZnTe nanowires. The main parameters needed are:

- The NW diameter should be small enough to ensure quantum confinement (of the order of the Bohr diameter, which corresponds to 12.4 nm in ZnTe);
- A very low density to avoid competition between NWs or shadowing effects, and possibly allows one to perform micro-photoluminescence on the as-grown sample;
- A high vertical yield to control the incoming fluxes and therefore the growth speed;
- High crystalline quality for optics measurements.

2.1.1 Substrate preparation

Semiconductor NWs are found to grow preferentially in the [111]B direction, so to obtain vertically oriented NWs it is more convenient to start from a (111)B surface. For all the NW samples grown in this work, I started from 300 nm thick ZnTe(111)B pseudo-substrates grown over deoxidized GaAs(111)B wafers. The growth of a ZnTe(111)B pseudo-substrate offers several advantages:

- to **avoid impurity incorporation** of foreign atoms like Ga or Si in the gold nanoparticles during their formation by dewetting, and then in the NWs during growth, since the eutectic temperatures of AuSi (363°C) and AuGa (340°C) are of the same order as the annealing temperature, while in our case the dewetting and growth temperatures are relatively low (350-400°C range) and indeed below the eutectic point of both AuZn (682°C) and AuTe (447°C) [32].
- to **avoid the formation of defects at the base of the NWs**. Even if the NWs are ideal systems to accommodate a lattice mismatch in the axial direction, thanks to the possibility to relax the strain radially[33], the heteroepitaxy of NWs on a highly mismatched substrate leads to the formation of structural defects.
- **to control the size and density of Au nanoparticles**. The dewetting of gold on a ZnTe(111)B surface was studied previously [10]. By changing the annealing temperature, the size of the gold catalyst can be modified. The density of the gold nanoparticles, which corresponds to the density of NWs, can be changed by changing the quantity of gold [10].

Experimental procedure for the substrate preparation

The GaAs(111)B substrates are fixed on the molyblocks using melted In. The molyblocks are then introduced into the UHV transfer modulus and annealed at 350°C for about 2 hours for outgassing. Then the wafers are transferred to the III-V chamber and annealed at 400°C, afterwards the temperature is raised to 650°C under a direct As flux between 8×10^{-6} and 1×10^{-5} Torr. The oxide evaporation is monitored using the RHEED pattern formed on a phosphor screen. At the beginning the pattern is not visible due to the presence of the oxide layer, at the deoxidation temperature a pattern appears, and it becomes clear after several minutes at this temperature, and the typical GaAs(111)B surface reconstruction appears (2×2 and $\sqrt{19} \times \sqrt{19}$).

Then the temperature is lowered and the sample is transferred to the II-VI chamber for the growth of the ZnTe(111)B layer. The ZnTe flux is previously calibrated on a ZnTe(100) reference sample to have a growth speed of 0.25ML/s at 340°C from RHEED oscillations. As all fluxes are calibrated from RHEED oscillations on a (100) reference substrate, we will use the (100) ML as unit of flux.

The GaAs deoxidized wafer is introduced in the II-VI chamber and its temperature is raised to 260°C. The optimal 2D layer growth for ZnTe in the (111)B orientation is obtained when the temperature is low and the flux is stoichiometric. Then the growth of the ZnTe (111)B layer is started. The growth time is 1 hour. This procedure was optimized by Pamela Rueda-Fonseca during her Ph.D.[10]. The lattice mismatch between GaAs and ZnTe, 7.7%, is relaxed already after the growth of less than 3 ML. The (111)B surface promote the formation of twins[10], with domains rotated by 180° around the [111] axis. The thickness of the buffer layer is about 300 nm.

At the end of the growth the ZnTe(111)B surface is smoothed by thermal annealing a 420°C under a Te flux of at least 1×10^{-6} for a few seconds. The RHEED pattern reveals the formation of the typical $(2\sqrt{3} \times 2\sqrt{3})$R30 surface reconstruction[10]. Then the temperature is decreased to 300°C under the Te flux to keep the surface reconstruction, then in the vacuum to 100°C.

2.1.2 Gold catalyst preparation

ZnTe NW growth is promoted by gold nanoparticles formed by dewetting of a submonolayer thick gold film. The gold is deposited on the sample surface using an effusion cell installed in the III-V chamber. This is generally done after two days from the deoxidation of the GaAs(111)B substrates to have a better vacuum in the chamber, otherwise the residual As pressure is too high.

The standard amount of gold I used for the preparation of my samples is 0.2ML according to the gold effusion cell calibration[10]. The gold effusion cell is heated at 1090°C and the flux is checked using an ion gauge placed in front of the substrate holder, and it is generally of 1.3×10^{-9} Torr. The GaAs/ZnTe(111)B substrate is transferred into

the III-V chamber and exposed to gold flux for 30 s at room temperature.

Then the sample is transferred back to the II-VI chamber for the dewetting and the NW growth. To obtain the gold catalyst, the sample is heated to 350°C for 5 minutes.

In Fig. 2.1 the RHEED pattern of the $[11\bar{2}]$ azimuth is shown as a function of the annealing temperature during the dewetting procedure. At 150°C and 200°C only the lines corresponding to the ZnTe(111)B substrate are visible. The temperature at which the spots corresponding to the presence of solid Au nanoparticles appear, and the dewetting starts, generally depends on the amount of Au deposited, and it decreases with the quantity of gold. For 0.2 ML, the dewetting generally starts at 225°C, the first spots start to appear (see the image at 250°C) and become brighter and brighter up to 350°C. After the stabilization at 350°C, we observe the formation of a gold induced surface reconstruction [10]: it is only observed when the ZnTe(111)B substrate has been previously smoothed under Te, as described in section 2.1.1.

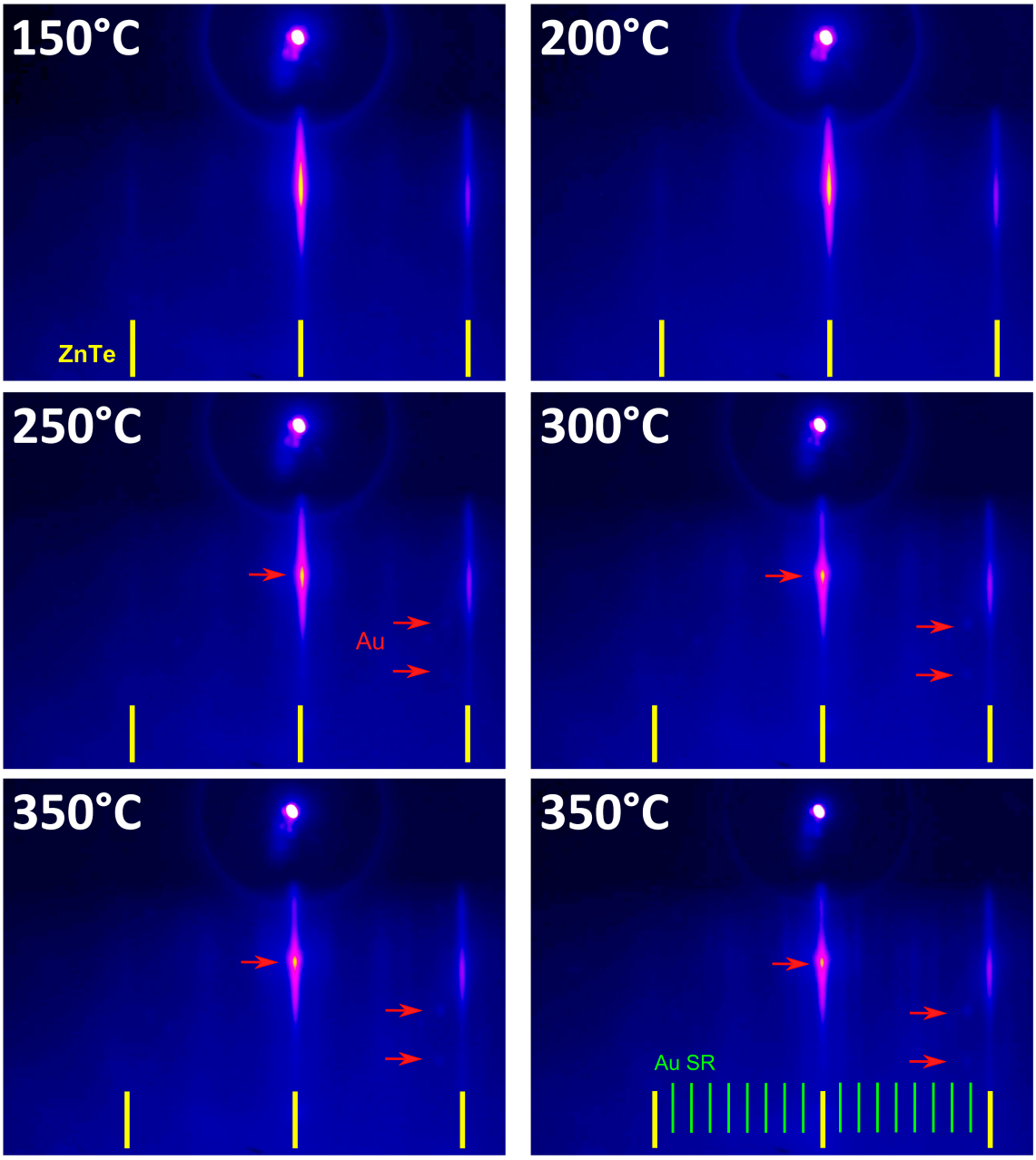

Figure 2.1: Evolution of the RHEED pattern recorded on the azimuth $[11\bar{2}]$ at different temperatures during the annealing of a 0.2 ML thick gold film on ZnTe(111)B substrate. After 2 minutes at 350°C a gold induced surface reconstruction [10] is also clearly visible.

Fig. 2.2(a) shows atomic force microscopy (AFM) and 2.2(b) SEM images of gold nanoparticles on ZnTe(111) buffer layer. AFM is more suitable to measure the height of the nanoparticles (the diameter measured in this way present a systematic error due to the convolution between the diameter of the nanoparticle and the AFM tip). The histogram in Fig. 2.2(c) shows the nanoparticle height dispersion in the sample. Instead SEM allows to better measure the diameter of the nanoparticles, see the histogram in Fig. 2.2(d).

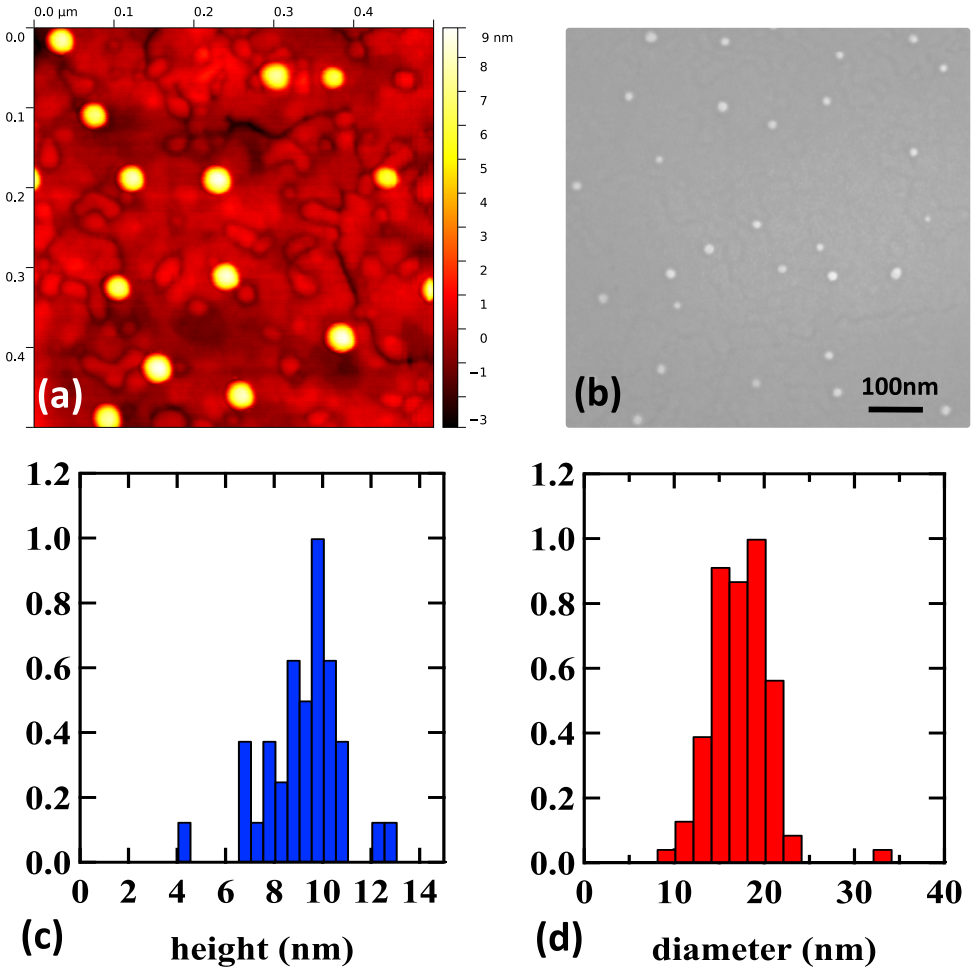

Figure 2.2: (a) AFM topography of the ZnTe buffer layer with the gold nanoparticles after dewetting at 350°C. (b) SEM image of the same sample. Statistical analysis of many images allow to obtain respectively the histograms of (c) the height distribution and of (d) the diameter of the nanoparticles on the sample The histograms (c) and (d) are normalized to 1.

2.1.3 The VSS growth of ZnTe NWs

Vapor–solid–solid (VSS) process has recently received attention as an alternative to vapor–liquid–solid (VLS) to grow NWs. In comparison with common VLS growth with liquid catalyst, VSS growth can prevent the catalyst species from incorporating into nanowires with deep-level impurity, and achieve compositionally abrupt interfaces by restraining the so-called reservoir effect. However, VSS growth still remains much less understood. As already explained in section 2.1.1, the temperature of the eutectic formation for AuTe and AuZn are much higher than the temperatures we use during the dewetting of Au and growth of ZnTe NWs. The growth mechanism for the ZnTe NWs is VSS. This is confirmed by the presence in the RHEED pattern of spots corresponding to the presence of solid gold nanoparticles during dewetting, Fig. 2.1, and during the growth, Fig. 2.5.

To explain the peculiarities of the growth of ZnTe NWs, I will consider sample M3194. The exact growth recipe and further analysis of this sample will be considered in the next section, 2.2, which deals with the incubation time problem.

Experimental procedure

After the formation of the solid gold catalyst by dewetting explained in section 2.1.2, and 5 minutes of annealing at 350°C to stabilize the system, the growth of the NWs is started at the same temperature. It is possible to grow ZnTe NWs in stoichiometric conditions, by exposing the sample to the flux from the solid ZnTe compound effusion cell, or under Te rich conditions, adding an excess of Te flux from the Te solid effusion cell (more information on the II-VI MBE in section 1.2.1). A Zn excess instead, inhibits the growth[3]. ZnTe NWs can be grown with different values of flux, ranging from 0.5 to 2 ML/s as calibrated on the ZnTe(100) reference sample. At the same time as the axial growth of the NWs, the flux on the substrate contributes to the growth of a two-dimensional layer, that can be determined by SEM images of a cleaved edge of the sample.

Peculiarities of ZnTe NWs morphology and growth mode

In the case of stoichiometric growth conditions, ZnTe NWs show polymorphism. In fact two different types of NWs grow on the same sample: cone-shaped NWs (tapered) with a crater at the base, and cylinder-shaped NWs with an hexagonal pyramid at the base. Indeed they have different crystal structures (ZB and WZ respectively, TEM images are shown in the next section 2.2) and, as shown in the SEM image of Fig. 2.3 they are found homogeneously distributed over the whole sample. In case of growth in excess of Te, only the cone-shaped NWs are found[3].

The ZB ZnTe NWs are cone-shaped due to radial growth on the sidewalls, while the WZ ZnTe NWs do not present radial growth. The tapering angle of the cone-shaped ZnTe NWs can be reduced by increasing the growth temperature to 375°C. This will be important for the growth of Nitrogen doped ZnTe NWs, as explained in section 4.3.3.

Even if these two types of NWs are grown under the same conditions, their morphology, crystal structure and length distributions are very different. In Fig. 2.4 we show the results on the statistical analysis over many SEM images of the NWs of the sample M3194 shown in Fig. 2.3. Between the shortest and the longest ZB NW there is a difference in length by a factor of ten [31].

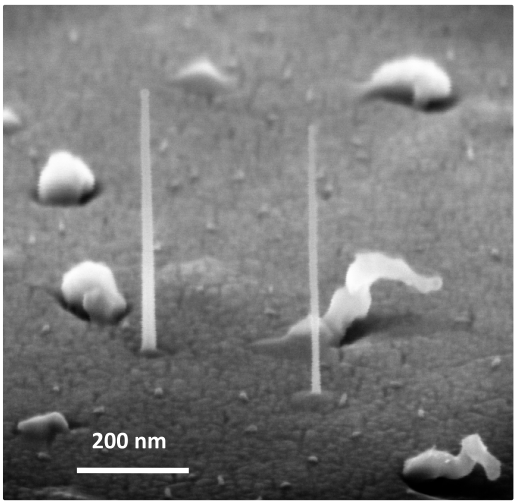

Figure 2.3: SEM image of the sample M3194, grown in stoichiometric conditions. It is possible to observe a cone-shaped NW, with a deep around its base, a cylinder-shape NW, with a pyramid at its base, and seven ill-formed objects.

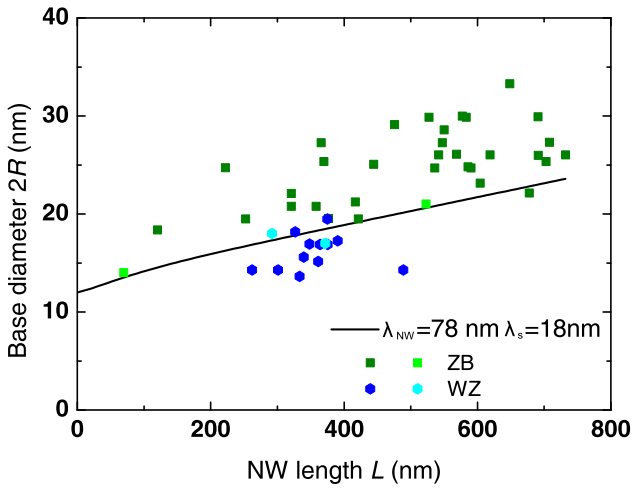

Figure 2.4: SEM data on the diameter at the base as a function of the length, for the NWs of the sample M3194 grown at 350°C with stoichiometric ZnTe flux. Green squares mark cone-shaped (tapered) zinc-blende NWs, blue hexagons cylinder-shaped wurtzite NWs; light colors are used for data obtained from TEM images, shown in section 2.2. The solid line is calculated using the diffusion-driven growth model[31].

The length distribution of the WZ NWs (cylinder-shaped) identified by blue hexagons is quite compact and the base diameter matches the typical gold particle diameter (no radial growth). The green squares correspond to the ZB NWs (cone-shaped) and in this case we observe a broad distribution of their length, with a factor of 10 between the longest and the shortest NWs. Such a large dispersion cannot be explained by the distribution of gold catalyst size, as shown in Fig. 2.2; the base diameter and the NW length are in fact correlated. This correlation has been modeled during the PhD of Pamela Rueda-Fonseca [10] using a diffusion driven growth model [31]. In these type of models [34, 35, 23], the morphology (length and shape) of the nanowires is directly related to

different values of the diffusion length on the substrate and along the NW sidewalls.

In the case of ZnTe NWs, different assumptions are made to describe the growth of the nanowires:

- The density of Au droplets (and hence the density of NWs on the substrate) is low enough that we can consider a single isolated NW.
- The NW is perpendicular to the substrate surface.
- The temperature is low enough that re-evaporation is negligible: that implies that the diffusion length is defined by the incorporation of adatoms on the substrate or on the NW facets.
- The NW growth rate is significantly larger than that of the 2D layer, hence we consider only the contribution of adatoms diffusing from the substrate and the NW sidewalls to the gold particle. The contribution of the direct flux onto the Au droplet is not too different from the contribution to the 2D layer away from the NW and their difference can be neglected.

The diffusion-based NW growth model adapted to these conditions is described in reference [31]. It assumes complete trapping at the tip of the NW (catalyst acting as a perfect sink). It involves the general solution of the diffusion equations of adatoms on the NW sidewalls in 1D, and on the substrate surface in 2D with a circular symmetry. It results in simple analytical relationships between the length L of the NW (axial growth) and the thickness h of the 2D layer far from the NW (growth in the absence of catalyst) on one hand, and between L and the radius R at the NW basis (lateral growth) on the other hand:

$$\frac{h}{R_0} = \frac{1}{2}\frac{\pi}{\tan\alpha}\ln\frac{1+\frac{\tan\alpha}{\pi}\left(\frac{\lambda_{NW}}{\lambda_s}\right)^2\left[\cosh\left(\frac{L+\widetilde{\lambda_s}}{\lambda_{NW}}\right)-1\right]}{1+\frac{\tan\alpha}{\pi}\left(\frac{\lambda_{NW}}{\lambda_s}\right)^2\left[\cosh\left(\frac{\widetilde{\lambda_s}}{\lambda_{NW}}\right)-1\right]} \tag{2.1}$$

$$\frac{R-R(0)}{R_0} = \frac{1}{2}\frac{\pi}{\tan\alpha}\left(\frac{\lambda_s}{\lambda_{NW}}\right)^2\ln\frac{1+\frac{\tan\alpha}{\pi}\left(\frac{\lambda_{NW}}{\lambda_s}\right)^2\left[\cosh\left(\frac{L+\widetilde{\lambda_s}}{\lambda_{NW}}\right)-1\right]}{1+\frac{\tan\alpha}{\pi}\left(\frac{\lambda_{NW}}{\lambda_s}\right)^2\left[\cosh\left(\frac{\widetilde{\lambda_s}}{\lambda_{NW}}\right)-1\right]} \tag{2.2}$$

where λ_s and λ_{NW} are the diffusion lengths on the substrate and along the NW sidewalls, respectively, R_0 is the radius of the contact area between the gold catalyst and the NW tip, and $R(0)$ is the initial radius of the gold nanoparticle. We have replaced the ratio of lateral to substrate flux by its value $\frac{\tan\alpha}{\pi}$. The effective diffusion length $\widetilde{\lambda_s}$ as defined in [31], depends on R and varies with the growth time, but the variations of $\widetilde{\lambda_s}$ for R from 10 to 35 nm are small, so it is kept constant in the calculation. This parameter influences mainly the growth when NWs are short, when the NWs are longer, it is $\widetilde{\lambda_s}+L$ that dominates the growth.

In the plot of Fig. 2.4, the solid black line is obtained using the diffusion driven growth model of reference [31]. In the legend are reported the parameters describing

the diffusion length of adatoms on the NW facets (λ_{NW}) and on the substrate respectively (λ_s). As will be discussed in section 2.2, such a large length dispersion cannot be explained without taking into account an incubation time different from NW to NW [31].

This corresponds to the observation by RHEED of a delay in the growth start. Fig. 2.5, shows the sequence of RHEED pattern recorded when the ZnTe NW growth in stoichiometric conditions was started at 350°C (the rotation of the sample is set with the MBE manipulator). Particular diffraction spot attributed to ZB or WZ ZnTe NWs, start to appear only after 1 min and 2 min respectively from the growth start.

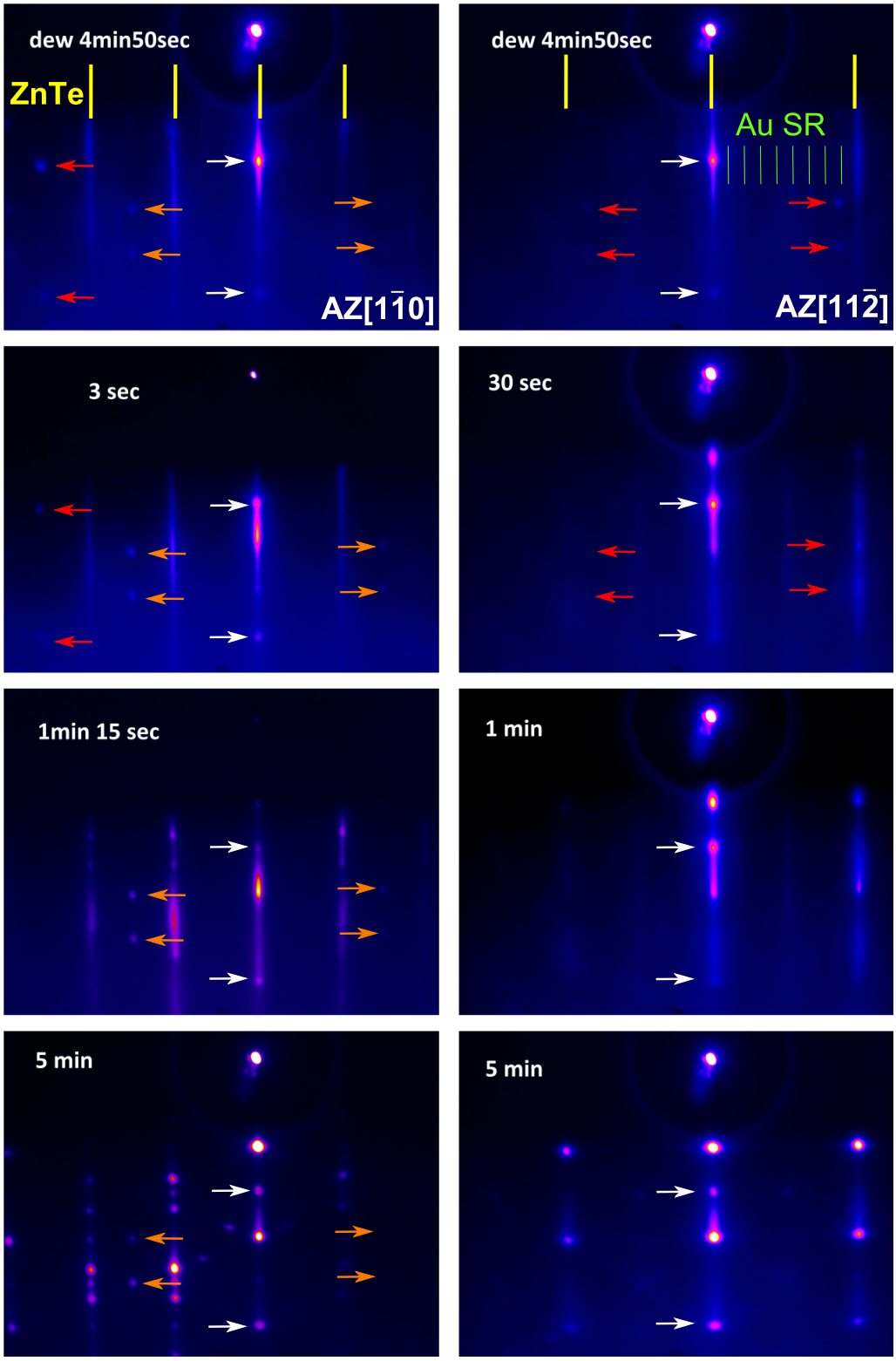

Figure 2.5: Evolution of the RHEED pattern recorded on the azimuth [11$\bar{2}$] (left) and [1$\bar{1}$0] (right) at different times during the growth of ZnTe NWs on ZnTe(111)B substrate. The orange and red arrows identify two families of Au diffraction spots with different orientation (see section 2.4). The white arrows belong to both families.

2.2 The problem of incubation time

Incubation times are often observed during the nucleation of semiconductor NWs usually grown by the vapor-liquid-solid (VLS) method using metal nanoparticles as catalyst. GaAs NWs[36] start to grow vertically on top of Si substrates after the formation of 3D GaAs islands. In the case of Si NWs, the incubation time is dependent on the catalyst diameter[37] and gives rise to NWs with a broad length distribution. Ge NWs are catalyzed by AuGe nanoparticles[38], so the delay is drastically reduced when a Ge layer is added on the gold film used to form the catalyst by dewetting. GaN NWs show instead an incubation-time-dependent morphology[39]. In the case of ZnTe nanowires, after the formation of the solid gold catalyst in vacuum, we observe by RHEED long incubation times for nanowire nucleation, growth of badly formed objects (loss of nanowires), and a length dispersion over a factor of ten on the same sample, Fig. 2.4.

2.2.1 The marker technique

The main evidence to the presence of an incubation time was obtained after the analysis of sample M3194, whose morphology and statistical analysis was already discussed in the previous section 2.1. In fact in order to obtain a precise information on a single NW, we used a marker technique, adapted from [40]. In sample M3194, during the growth of the ZnTe NW (stoichiometric Zn+Te flux from the ZnTe cell at 350°C), we inserted 10 thin CdTe markers (stoichiometric Cd+Te flux from the CdTe cell) without changing the growth temperature, forming a periodic crystal structure, as shown in Fig. 2.6. The last ZnTe part was grown for half time with respect to the others ZnTe parts.

Figure 2.6: Growth recipe of sample M3194, with 10 CdTe sections used as markers. The experimental procedure is explained in section 2.1.3

The EDX image of Fig. 2.7 of a NW deposited on a grid clearly reveals 7 regularly spaced CdTe insertions (and another one at the broken end). On such a broken NW, we cannot exclude that the two missing insertions were lost in the harvesting process. Probably this NW was not perpendicular to the substrate. Note the

Figure 2.7: EDX image of a NW deposited on a holey carbon grid (composite of 5 higher resolution images). Colored areas are those where the Cd (red), Zn (yellow), Au (cyan) or O (black) signal exceeds an arbitrary threshold.

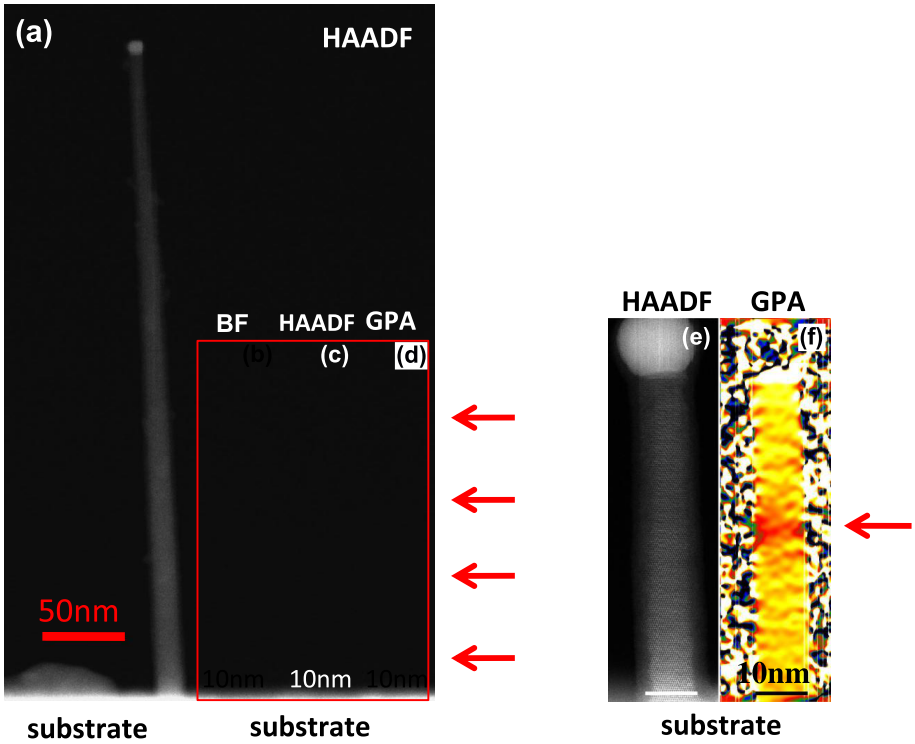

Figure 2.8: (a) HAADF image of a complete NW (NW1) with the ZB structure on the substrate (visible at the bottom, white area). (b) BF and (c) HAADF images of the bottom part of the same NW with (d) GPA analysis showing four small regions with a height of around 4 nm with larger lattice spacing (red arrows). (e) HAADF STEM image and (f) GPA analysis of a second NW on the same sample (NW2) that also has the ZB structure but is much shorter. The GPA analysis shows only one region with larger lattice spacing (red arrow).

To exclude any effect of harvesting, the sample was cleaved into a thin slice and isolated NWs were found in the thinner part of the slice. These as-grown NWs were observed by scanning transmission electron microscopy (STEM). Two cone-shaped NWs with a very different length (520 and 70 nm respectively) were observed and geometrical phase analysis (GPA) was applied to the high resolution images [31], allowing us to determine the crystal structure and local lattice parameter. The ZB structure was confirmed for both NWs. The topmost half of the longer NW (NW1 in Fig. 2.8) could not be analyzed due to vibrations and charging effects. In the lower half, four CdTe insertions are clearly identified. The period is 68 nm, with 64 nm for the ZnTe spacers and 4 nm (full width half maximum) for the CdTe insertions. On the shorter NW of Fig. 2.8, only one CdTe insertion is identified. In Fig. 2.10 we show TEM and GPA analysis for a WZ NW.

In none of the NWs it was possible to find 10 markers. Some markers are missing, but the present results rule out the harvesting effects. We can notice that in NW1 the spacing between the CdTe markers is constant and in NW2 the distance between the Au catalyst and the marker is about half the ZnTe spacing between the markers of NW1 (as in the growth recipe). So from NW to NW, a change in the growth speed cannot explain

such a long dispersion in length by a factor of 10 (see Fig. 2.4). This suggests that the incubation time observed can be long and different from NW to NW, and corresponds to *in-situ* RHEED observation of a delay in the growth start, see Fig. 2.5.

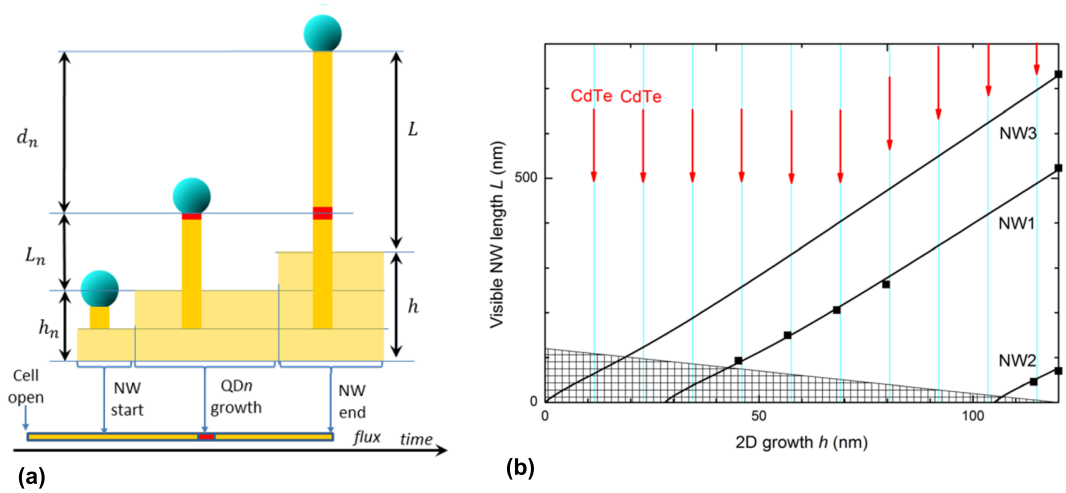

Figure 2.9: (a) Sketch of the growth of a NW with a CdTe insertion. (b)Plot of the visible length of NW1 and NW2 of Fig. 2, as a function of the 2D layer thickness; we plot (squares) L_n vs. h_n (as defined in (a), and marked here by the red arrows) at the time of insertion of CdTe, and L at the end of the growth, vs. h. NW3 is the longest NW observed by SEM on the same sample. The hatched triangle represents the masking by the 2D layer (i.e., the thickness $(h - h_n)$ remaining to grow after the formation of the CdTe insertion). The solid lines are the fit with the diffusion driven growth model, and different incubation times.

To describe the growth of a ZnTe NW we can use the sketch of Fig. 2.9(a). The NW growth occurs at the same time as the 2D layer regrowth. The total thickness of the parasitic 2D layer, $h = 120$ nm, was measured on a cleavage plane, using a 90° SEM image. By assuming a constant growth rate of the 2D layer, we can use it as a time scale for the growth recipe. In the sketch of Fig. 2.9(a), the length L is the visible length of the NW, a part of the NW being hidden by the parasitic growth of the 2D layer. At the moment of the growth of the CdTe insertion, the visible length L_n of the NW is obtained as $L_n = L + h - d_n - h_n$ and the corresponding thickness of the 2D layer h_n is deduced from the growth sequence. The visible length of the nanowire, L, the radius of the NW, the radius of the gold nanoparticle, and the radius of the gold-tip contact are available from the HAADF images of Fig. 2.8; the distance of several CdTe insertions from the tip, d_n, are measured on the GPA images.

Fig. 2.9 (b) plots $L(h)$ and $L_n(h_n)$ for the two NWs of Fig. 2.8. The black squares (from the right) are the NW visible length of the two NWs of Fig. 2.8, and the longest NW observed at SEM in Fig. 2.4. For NW1 and NW2 the others black squares are obtained as the measured position of the CdTe marker. The hatched part correspond to the NW part covered by the 2D regrowth at the end of the recipe. We assume that

the longest NW, NW3, started to grow at the beginning of the growth. In any case we couldn't have observed 10 markers due to the 2D layer regrowth.

Even without the lines obtained using the diffusion-driven growth model, with the same diffusion lengths as for Fig. 2.4, it is clear that the NWs started to grow after a significant incubation time. To apply the diffusion-driven growth model, we assumed that the gold nanoparticle was close to a full-sphere from the beginning of the growth, with the contact diameter 7.7 nm (NW1) and 7.9 nm (NW2), as measured on the HAADF image. The length measured for NW3 is well fitted keeping the same values of diffusion lengths, and assuming $2R_{tip} = 7.3$nm. With these values of the parameters, we deduce an incubation time for NW1 and NW2 (and assumed an immediate start for NW3).

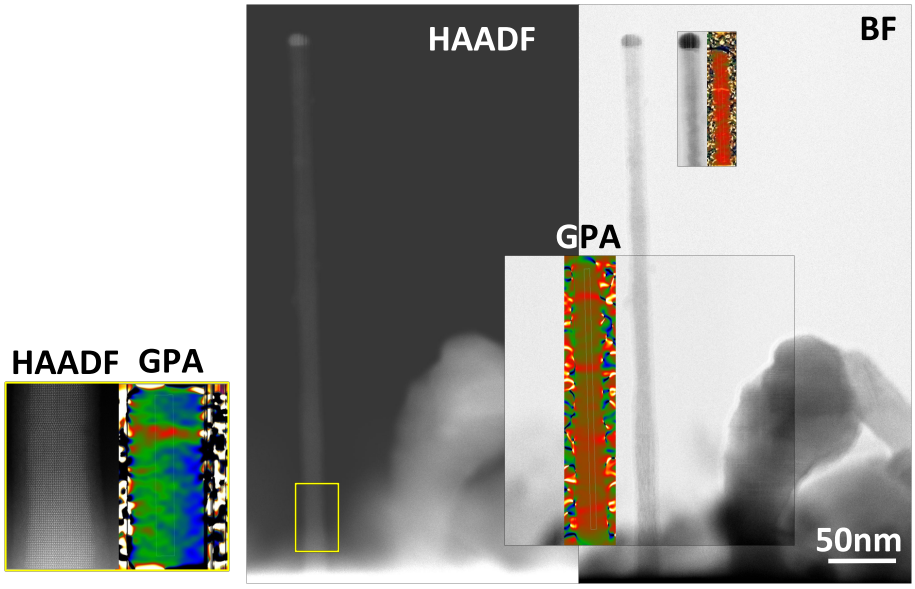

Figure 2.10: HAADF and brigth field (BF) image of a complete NW with the WZ structure, the substrate is visible at the bottom (white area). HAADF images of the bottom part of the same NW with the GPA analysis showing four small regions with a height of around 4 nm with larger lattice spacing (in red). For the top part GPA was obtained from BF image where 1 region has a larger lattice parameter.

For completeness we also show the TEM and GPA analysis of a WZ NW in Fig. 2.10. The NW total length is 372 nm, with an average spacing of 51 nm (thus containing 7 markers by extrapolation). WZ NWs have a lower growth rate with respect to ZB NWs, as shown in Fig. 2.4.

2.3 Dewetting under Zn flux

As mentioned in the previous section, in the case of VLS growth of semiconductor NWs such as GaAs NWs[36] on Si substrates, Si NWs [37], Ge NWs [38] and GaN NWs [39] a dispersion in the incubation time can have dramatic consequences, such as a broad distribution of the NW length [36, 37] or even different NW morphologies [39]. The presence of parasitic growth (the growth of ill-featured nanostructures [36, 41]) and consequently, the number of vertical NWs, can also be affected. Possible solutions involve a precise adjustment of the growth conditions (*e.g.*, in the autocatalytic growth of GaAs NWs on Si [41]) or a pre-treatment of the initial gold film in order to ensure a uniform saturation of all gold droplets [38]. This section is devoted to the investigation of the effects of a pre-treatment of the gold catalyst on the first stages of ZnTe NW growth. The validity of such a pre-treatment in the case of VSS growth mode has not been reported before. The results described in this section were recently published in Ref. [42]. I will show that the preparation of the Au nanoparticles is indeed a key parameter to control the incubation time in the VSS growth of ZnTe NWs.

The standard growth procedure for this study, explained in section 2.1, was modified during the dewetting procedure of section 2.1.2. The gold catalysts are formed by dewetting at 350°C for 5 min, and during this time the gold film is exposed to a Zn flux of 0.4ML/s ("Zn-dewetting": this is the main difference with respect to "vacuum-dewetting" as in Ref. [31] and the previous sections of this Chapter). In what follows I will use 0.4 ML/s of Zn for Zn-dewetting if it is not otherwise mentioned. Then the NW growth is started at the same temperature in stoichiometric conditions as explained in section 2.1.3. The present section describes the results obtained on three series of samples.

2.3.1 Series A

Series A explores the effect of adding a flux during dewetting and consists of 6 samples where, during the 5 min at 350°C, the gold catalyst was kept in vacuum, or exposed to a Te flux (0.5 ML/s) or to a Zn flux (0.1, 0.2, 0.4 and 0.8 ML/s)

In Fig. 2.11 we compare SEM images for two samples of series A: the sample in panels (a) and (c) represent the starting point of my PhD growth experiments, where the gold nanoparticles were prepared in vacuum as in Ref.[31], while the sample in panels (b), (d), (e) and (f) was grown after dewetting of the gold nanoparticles under a Zn flux of 0.8 ML/s. When the catalysts are prepared in vacuum, as in Fig. 2.11(a) and (c), the great majority of objects on the sample are not vertical NWs but ill-formed objects. Fig. 2.11(b)-(d) show that dewetting under Zn increases the number of vertical NWs (including both cylinder-shaped NWs with a pyramid at their base, Fig. 2.11(e), and cone-shaped NWs, Fig. 2.11(f)). The cone-shaped and cylinder-shaped NWs have different average lengths, as evidenced by the green dashed and blue dotted lines, and

the length dispersion within each family is small, which makes a contrast with the case of vacuum-dewetting [31].

By statistical analysis of SEM images, we measured an improvement of the yield of vertical NWs, from 20% (vacuum dewetting) to 80% (dewetting under a Zn flux of 0.8 ML/s). For all the samples of series A, the yield as well as the density of NWs are reported in Table 2.1. Te-dewetting results, at the most, in a moderate improvement, with 25% of vertical NWs for a Te flux of 0.5 ML/s. The effect of even a small Zn flux is clear; it somewhat saturates at higher values. Note that the density increases from about 1 to 12 vertical NWs per μm^2. This is due for a part to the elimination of most parasitic growth, but also to the increase of the total number of objects on the sample, by a factor of about 3. Such an increase is expected, if the nanoparticle shape is preserved, from the slight decrease of the diameter of the gold nanoparticles, see Table I, from an average of 18 nm (vacuum dewetting) to 13 nm (Zn flux of 0.8 ML/s).

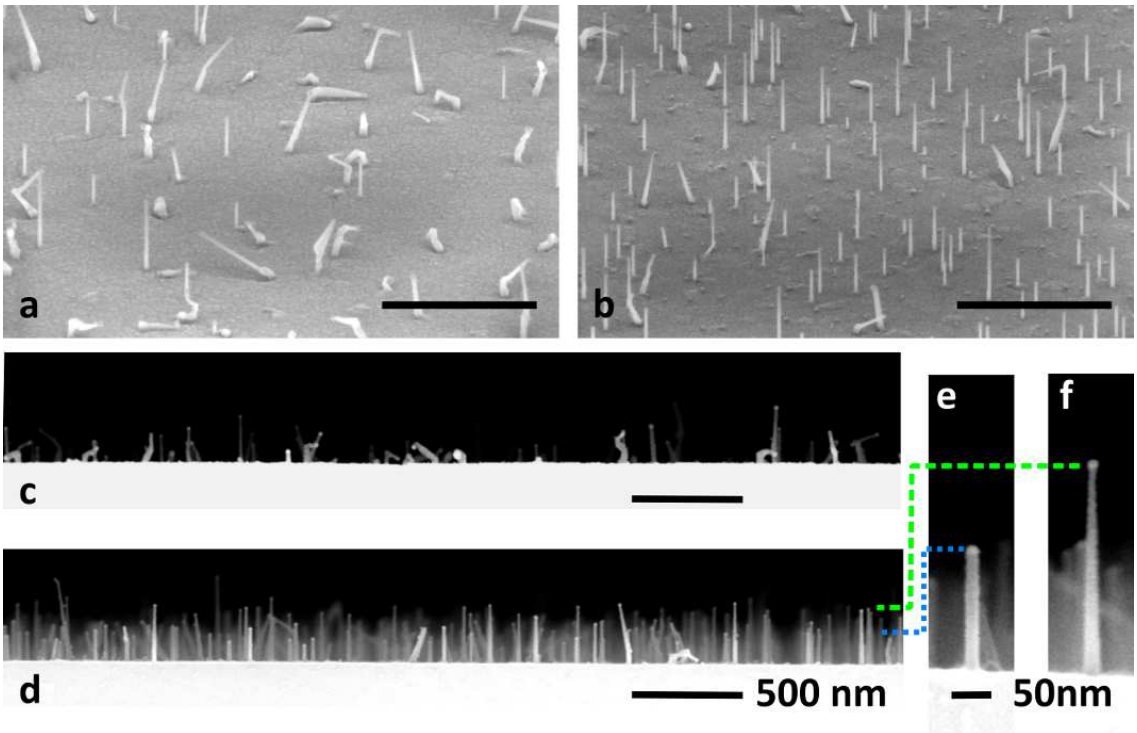

Figure 2.11: SEM images of as-grown ZnTe NWs tilted at (a-b) 65° and (c-d-e-f) 90°. For the sample in panels (a-c) the dewetting was done in vacuum while for the one in (b-d) a Zn flux of 0.8 ML/s was added. In panels (e-f) we show higher magnification images of the two kinds of NWs that are present on the samples, (e) cone-shaped and (f) cylinder-shaped with a pyramid at the base. The height of the cone-(cylinder-) shaped NWs is marked with a green dashed (blue dotted) line. The scale bar for panels (a-b-c-d) is 500 nm.

dewetting	yield (%)	density/μm^2	diameter (nm)
Zn 0.8 (ML/s)	80	13	13±1
Zn 0.4 (ML/s)	72	12	13±2
Zn 0.2 (ML/s)	71	12	14±2
Zn 0.1 (ML/s)	45	5	15±2
vacuum	20	1	18±2
Te 0.5 (ML/s)	25	2	17±2

Table 2.1: Summary of Series A. From the left the dewetting condition, the yield of vertical NWs, the density of vertical NWs, and the average diameter of the gold catalyst with the relative standard deviation.

In Appendix A more information of the analysis of this series can be found.

2.3.2 Series B

This series is devoted to the investigation of the effects of the Zn-dewetting on the incubation time. Series B involves a single sample with 5 CdTe markers, 4 embedded in the ZnTe NW and a last one at the end; it was grown at 375°C with an additional Te flux [31] (after Zn-dewetting at 350°C and a ramp of 2 min from 350 to 375°C under a Zn flux of 0.4 ML/s).

Fig. 2.12(a) shows the growth sequence. In Fig. 2.12(b), the horizontal axis is the total amount of ZnTe sent before a CdTe marker is inserted (position indicated by the red segments), normalized to 1 for the complete growth sequence. Data plotted at complete growth sequence display the visible length of the NW. It should be kept in mind that a 2D layer masks the bottom of the NWs: from a SEM image of a cleavage plane, we estimate this 2D layer to be $\sim$ 100 nm thick, with $\sim$ 70 nm of ZnTe, in agreement with the growth sequence and previous calibrations. Data at values < 1 display the position of each CdTe marker, with respect to the NW tip, as determined by the GPA analysis of the STEM images (6 NWS) or by EDX (2 NWs). These NWs can be identified as wurtzite or zinc-blende from their morphology, cone-shaped or cylinder-shaped with a pyramid at the basis; the crystal structure was directly confirmed on the STEM high-resolution images for 2 zinc-blende and 2 wurtzite NWs.

Two distinct features appear from these raw data, without further analysis: (1) the data of all NWs converge to a single point and (2) they are grouped in two families corresponding to the zinc-blende NWS and the wurtzite NWs, respectively. A direct, qualitative interpretation of these two features is that (1) the presence of a convergence point suggests an identical start of all NWs, its position along the vertical axis denoting the thickness of the 2D layer (*i.e.*, the total NW length should be measured from this position) and (2) the growth rate of wurtzite NWs is smaller than that of zinc-blende NWs, with a small dispersion within each family, in agreement with what found for WZ

NWs.

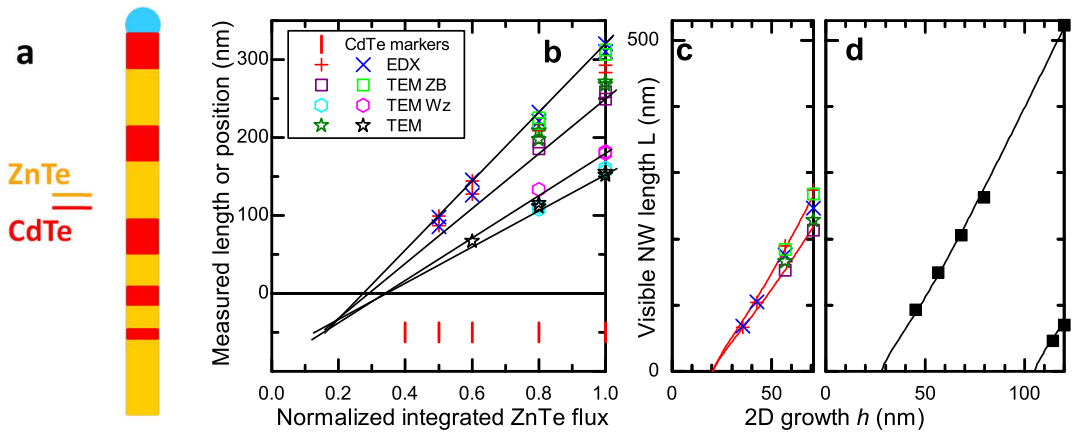

Figure 2.12: (a) Growth sequence; (b) raw data on the visible length of the NWs and the position of the CdTe markers, for different NWs, as measured by STEM and EDX, with respect to the amount of ZnTe sent at the time the marker was inserted (normalized to the whole growth sequence). For each marker, the position of the two interfaces (CdTe on ZnTe and ZnTe on CdTe) are indicated (note the limited growth of CdTe at this temperature [43]). The red segments indicate the positions of the markers. The black solid lines are eye-guides. (c) Same data analyzed along the diffusion-driven growth model of Ref. [31]: visible ZnTe NW length *vs.* the thickness of the ZnTe 2D layer, both at the time the marker was inserted. Solid lines are calculated with h_0=20 nm, $2R_{tip}$=7.8 nm and 9.3 nm, respectively, $\lambda_{NW} = 78$ nm and $\lambda_s = 18$ nm. (d) same plot for the data of Ref. [31]. Solid lines are calculated with h_0=28 nm and $2R_{tip}$=7.7 nm, and h_0=105 nm and $2R_{tip}$=7.9 nm, respectively, $\lambda_{NW} = 78$nm and $\lambda_s = 18$nm.

As in the previous subsection, a more detailed analysis can be obtained using the diffusion driven growth model of Ref. [31], as shown in Fig. 2.12(c)-(d). We consider only the zinc-blende NWs. Fig. 2(c) was deduced from the raw data in Fig. 2.12(b), as follows. The horizontal axis is the thickness of the 2D layer when taking into account the ZnTe contribution only. The small height of each CdTe marker was measured and subtracted from the raw data. Finally, knowing the position of each CdTe marker and the thickness of the 2D layer at the time the marker was grown, we can calculate the value of the NW length at this time. This is plotted in Fig. 2.12(c), and Fig. 2.12(d) is a reminder of the data of Fig. 2.9(b) for the sake of comparison. All solid lines are obtained using the diffusion-driven growth model of Ref. [31].

The most important fitting parameter is the ratio $\frac{\lambda_{NW}}{2R_{tip}}$ between λ_{NW}, the diffusion length on the NW sidewalls, and R_{tip}, the contact radius between the gold nanoparticle and the NW tip: it impacts the growth rate, *i.e.*, the slope in Fig. 2.12(c)-(d). A second important feature of the fitting lines is the position along the horizontal axis: it is determined by the value of the incubation time (expressed in 2D layer thickness, h_0), although it can be influenced by the value of the diffusion length on the substrate, λ_s (which changes the initial growth rate).

The behavior of the two samples is strikingly different. In the case of vacuum dewetting, Fig. 2.12(d), the radius R_{tip} was measured on the STEM high-resolution image of each NW, and the fit involves the same values of the diffusion length, λ_{NW}=78 nm, but markedly different values of the incubation time, h_0=105 nm for the shortest and h_0= 28 nm for the longest NW. In the case of Zn-dewetting, Fig. 2.12(c), the values of $\frac{\lambda_{NW}}{2R_{tip}}$ are not significantly affected and show a weak dispersion from NW to NW (but R_{tip} cannot be measured since the last sequence is a CdTe insertion, which significantly alters the nanoparticle shape). Fig. 2.12(c) thus confirms that the most dramatic effect of Zn-dewetting is the suppression of the dispersion in the incubation time.

2.3.3 Series C

A statistical analysis of pure ZnTe NWs, including a sample with a longer growth time, brings complementary information on the remaining length dispersion and its origin.

Series C is made of two samples grown after Zn-dewetting at 0.4ML/s, with a growth time equal to 10 and 40 min, respectively. Fig. 2.13(a) show a SEM image of the sample grown for 40 min and (b) the statistical analysis on the base diameter vs the NW length. Only a factor of two is present from the shortest to the longest NW, instead of the factor of 10 for sample in Fig. 2.4.

In Fig. 2.14 we again consider only the zinc-blende NWs of the two samples forming series C. Fig 2.14(a) displays two NWs which were included in the statistics: indeed we observe NWs with a nanoparticle at the tip forming a half-sphere (similar to the shape observed after dewetting), and other NWs with a nanoparticle forming a quasi-

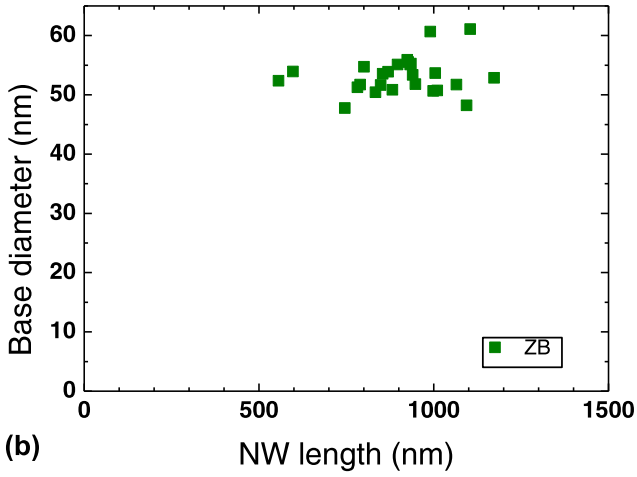

Figure 2.13: (a) 65°C tilted SEM images of as-grown NWs from series C and (b) SEM data on the diameter at the base vs. the length of ZB NWs.

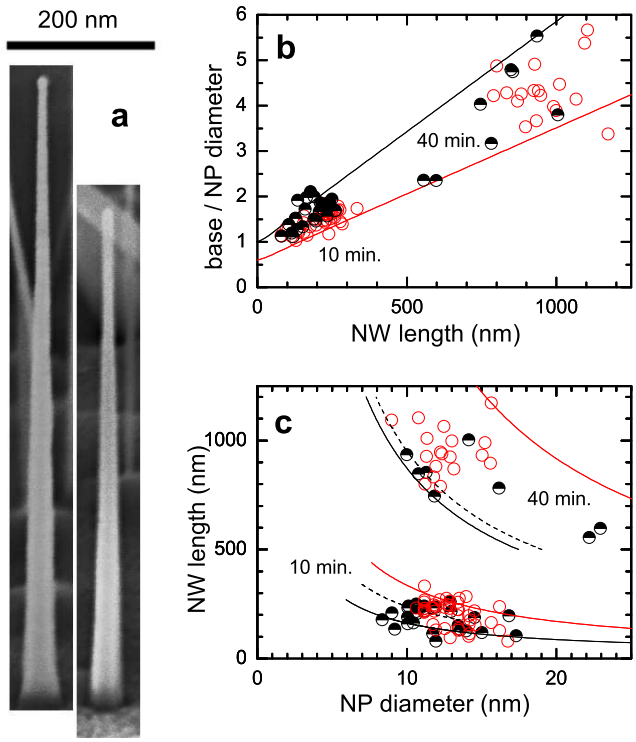

Figure 2.14: (a) 65°C tilted SEM images of cone-shaped NWs from series C, featuring the two characteristic shapes of the nanoparticle, almost full-sphere and half-sphere; (b) ratio of the base diameter to nanoparticle diameter, as a function of the NW length. (c) NW length *vs.* the nanoparticle diameter. The half-filled symbols identify the NWs with an half-sphere nanoparticle and the open symbols the full-sphere. The lines are calculated in the diffusion-driven model of Ref. [31], assuming half-sphere nanoparticles throughout the growth (black solid lines), or full-sphere with a tip radius 0.6 times the nanoparticle radius (red solid line) with an incubation time h_0=20 nm. The dotted line is calculated with no incubation time.

full-sphere. For the same volume of the nanoparticle, the diameter of the full sphere is slightly smaller (by a factor $\sqrt[3]{2}$), and the tip contact radius R_{tip} is much smaller. As the growth rate depends on R_{tip}, we thus expect an influence of both the nanoparticle volume and the nanoparticle shape.

In the frame of the diffusion-driven model [31], if the tip contact diameter is maintained during the whole process, a plot of the ratio between the base diameter and the tip diameter (i.e., the radial growth normalized to the initial diameter), as a function of the NW length, should follow a single curve, independent of the nanoparticle radius and possible incubation time (see Ref. [31]). If the nanoparticle keeps a half-sphere shape over the whole growth process, the relevant radius R_{tip} is simply the nanoparticle radius. Fig. 3(b) displays such a plot for about one hundred NWs of series C, with both half-sphere nanoparticles and quasi-full-sphere nanoparticles, as indicated. The average gold catalyst dimension with its standard deviation is 13±3 nm for the 40 minutes sample. The solid line is calculated for λ_{NW}=65 nm and λ_s=20 nm, the most significant parameter being actually $\lambda_s^2/\lambda_{NW}^3$: it sets the upper limit of the distribution of experimental data. If we now assume that the nanowire shape is full sphere, the tip radius is smaller than the nanoparticle radius, and the calculated curve has to be multiplied by the corresponding reduction factor, R_{tip}/R_{NP}. In Fig. 2.14(b), the curve with R_{tip}/R_{NP}=0.6 sets the lower limit. We observe that all observed NWs lengths are between the limits expected for the full sphere and half sphere catalyst particle respectively (black and red lines). However, no clear separation is visible between the NWs having a full sphere, and those having a half sphere catalyst particle. It appears therefore that catalyst particles can change shape during growth, or alternate between a full and a half sphere particle. This effect of the two possible shapes of the nanoparticle was already noticed in Ref. [31] and it is still present.

In order to evidence the possible influence of the nanoparticle size, Fig. 2.14(c) displays the NW length as a function of the nanoparticle diameter evaluated on the SEM images. In principle, the relevant radius here should be the tip radius R_{tip}. However we have here only a rather crude evaluation of the radius, due to a moderate resolution, and to the presence of an amorphous layer which is probably a mix of oxides and re-deposition. The lines are drawn using Eq. 1 of Ref. [31], with the same values of the diffusion lengths as in Fig. 2.14(b), and a common incubation time h_0=20 nm (and no incubation time for the dotted line). The effect of the nanoparticle size is present, although not dominant; it was completely hidden by the effect of the incubation time in Ref. [31].

To conclude, the diffusion-driven model, applied in Fig. 2.12(c) and Fig. 2.14, evidences that the presence of a Zn flux during the dewetting dramatically influences the first step of growth (incubation time) and not the characteristics of the growth once started. Note that this model is purely phenomenological; for instance, the diffusion lengths are not attributed to Zn or Te, and they are assumed to be constant throughout

the growth. A part of the remaining incubation time could be due to a very low value of λ_s at the beginning of growth.

One motivation to use VSS instead of VLS, is the small amount of constituents of the NWs which are expected to be present in the gold solid nanoparticles, as compared to gold liquid droplets. A new parameter however emerges in the case of VSS: the crystal structure of the nanoparticle, and its orientation with respect to the substrate and to the NWs. A complete study of gold nanoparticle on a Si(111) substrate has revealed [44] a very rich diagram, with nanoparticles of different shapes, sizes and orientation. We may expect similar features in the case of ZnTe, with possible effects on the first steps of growth of the NWs. This will be considered in the next section.

2.4 XRD measurements on gold catalyst

To gain further insight on the gold solid catalyst crystal structure and on the presence of an epitaxial relationship between the ZnTe(111)B substrate and the solid gold, I had the possibility to participate to X-Ray diffraction characterization using the diffractometer PHENIX (mesures in-Plane et Haute rEsolution de Nanostructures par dIffraction X).

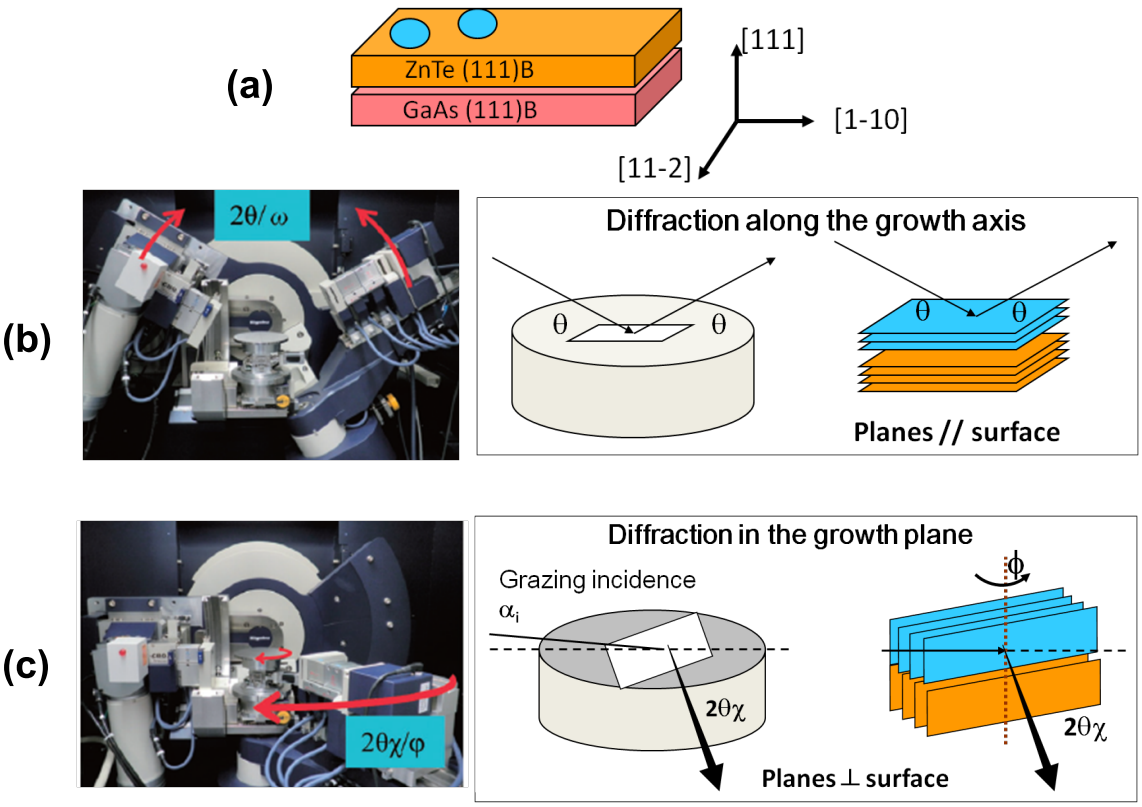

Figure 2.15: (a) sketch of the sample geometry with the GaAs(111)B wafer, the ZnTe(111)B buffer layer and the gold particles, with the indication of the reference crystal axis. Two kinds of geometry has been used: (b) out of plane diffraction, to probe the orientations of the crystal planes parallel to the surface or (c) in plane measurements, to probe the planes perpendicular to the surface.

In the in-plane geometry (as in the out-of-plane) two types of scans were analyzed:

- omega scan (noted phi scan in the reference manual) where only the sample is rotated with the detector fixed at a 2theta position. This type of scan gives the orientation(s) of the plane family with respect to the substrate. The width of the peaks results from a convolution between the effect due to the in-plane size of the nanoparticles and the dispersion of the orientation diagram;

- 2theta-theta scan (noted 2thetachi/phi scan in the reference manual) where both the sample and the detector move. This type of scan gives information about the

different families of planes present in-plane. The width of the each peak is related to the in-plane size of the nanoparticles.

For this study we have analyzed four samples: for two of them the gold nanoparticles were prepared by dewetting under vacuum, while for the other two were prepared under Zn-flux. For each of the two types of preparation for the gold nanoparticles, one sample was cooled down rigth after the dewetting, while for the other the growth of ZnTe NWs was done for 10 minutes.

From the 2thetachi/phi scan (not shown) only the Bragg peak corresponding to the (2-20) Au reflection was observed for the Au signal in the in-plane measurements. Figure 2.15 represents the phi scan of the 4 samples around this (2-20) Au reflection.

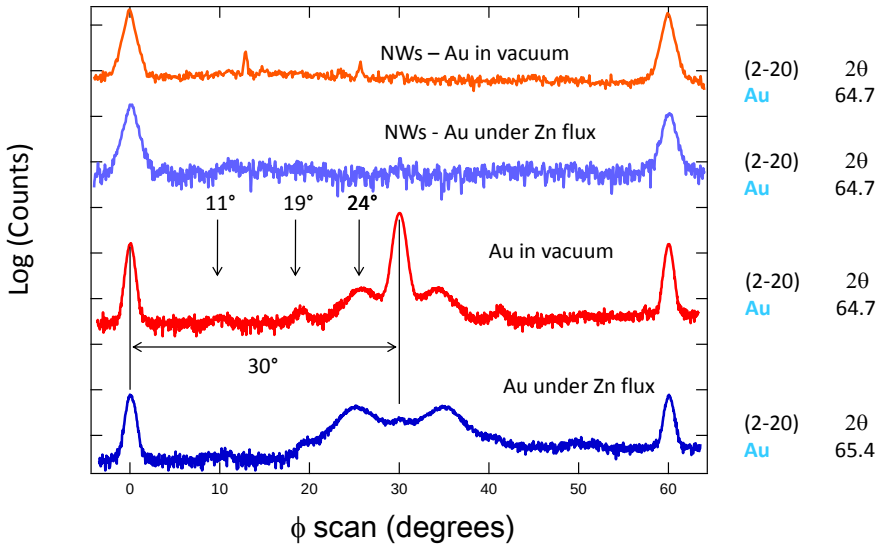

Figure 2.16: In-plane scans around the (2-20) reflection of Au for 4 different samples : 2 samples where the gold layer was dewetted under vacuum (red) or under "Zn-flux" (dark blue) and 2 samples stopped after 10 minutes of ZnTe NWs growth were the dewetting was modified; under vacuum (orange) or under Zn (light-blue). The 2theta position is indicated for each measurement on the right and for all the scans the phi angle of zero corresponds to the orientation of the ZnTe (2-20) planes of the buffer.

In Fig. 2.16 are shown the results of in plane geometry measurements. The two curves in dark color, red and dark blue, correspond to measurements on gold nanoparticles after vaccuum-dewetting and Zn-dewetting respectively. The orange and light blue curves correspond instead to the measurement done on the gold nanoparticle after a growth of 10 minutes, again for vaccuum-dewetting and Zn-dewetting respectively. For all the samples several peaks are observed. The $\phi = 0°$ angle corresponds to the (2-20) orientation of the ZnTe substrate. The $\phi = 0°$ peak is the dominant one in both

samples of NWs and in the Zn-dewetting sample. As revealed in the TEM FFT of figure 2.17 it corresponds to gold nanoparticles with the 3 crystallographic axis parallel to the ZnTe ones.

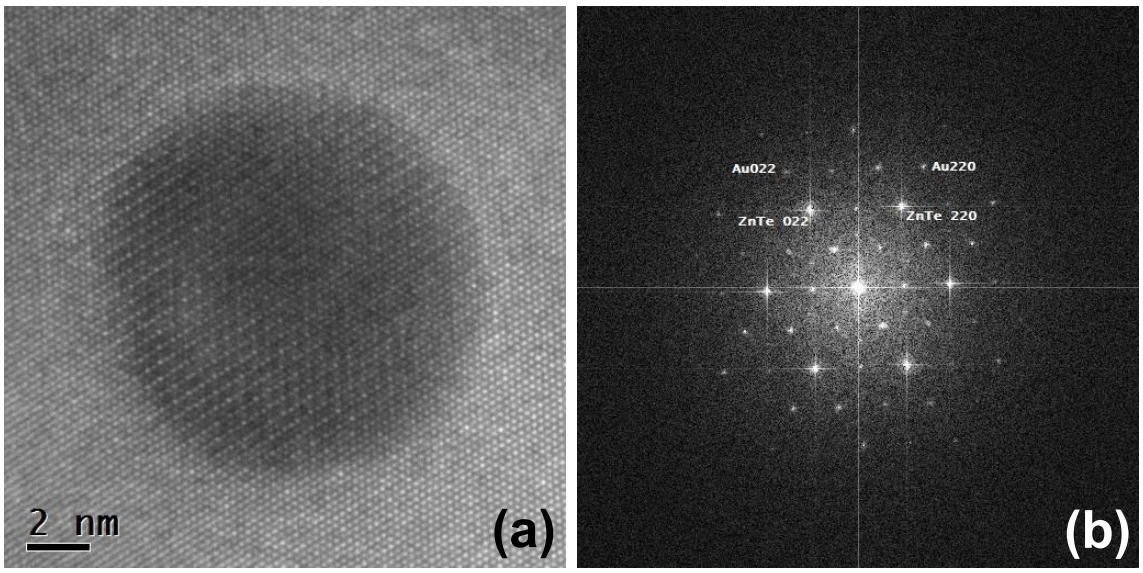

Figure 2.17: (a) Plan view high resolution TEM study along the ZnTe [111] zone axis of a sample after Zn-dewetting showing a crystalline Au nanoparticle of 12nm diameter, (b) corresponding Fast Fourier Transform revealing that the axis of the gold lattice are parallel to the ZnTe lattice.

On the contrary the dominant peak in the case of the vacuum-dewetted sample is a peak rotated by 30°, which corresponds to gold nanoparticles with the out of plane (111) axis aligned with the ZnTe substrate, but with a 30° rotation of the in-plane (2-20) and (22-4) axis. Others peaks can be observed for in plane rotation of $\phi = 11°$, 19° and 24°. As revealed by SEM and confirmed by TEM and 2theta/chi measurements (not shown) all the nanoparticles have the same size (12 nm as in Fig. 2.17) with a rather small dispersion images (see Appendix A). The difference in width from the phi scans comes from different orientation diagrams.

The presence of Zn during the dewetting can also be observed in the 2theta position of the Au(2-20) reflection. While it corresponds to pure Au (fcc lattice) for the dewetting in vacuum, it is shifted by 0.7 degrees for the Zn-dewetting.

The two main orientation of the gold particles at 0° and 30° are also observed in the in-situ RHEED images as shown in Fig. 2.5 where the diffraction spots corresponding to the 0° nanoparticles are indicated by orange arrows and the 30° nanoparticles by red arrows.

In conclusion we observe that after the dewetting several orientations of the Au nanoparticles are observed. The amount of each type depends on the dewetting procedure. On the contrary when the growth of the NWs is started only one orientation remains with the axis of the Au nanoparticles parallel to the ZnTe. This feature is not only confirmed by ex-situ in-plane X-ray diffraction but also by in-situ RHEED where

after 1 min growth the 30° rotated nanoparticles spots has disappeared but the 0° one remains all the growth time (see Fig. 2.5).

2.5 Conclusion

This study of the effect of Zn-dewetting was not scheduled initially in my PhD work. It was inspired by a talk at Euro MBE conference (see Ref. [45]) and the preliminary results were so encouraging that we decided to spend some time to optimize the process.

The result is a strong decrease of the length dispersion (from a factor of 10 to 2, with identified origins of the residual dispersion) and an increase of the vertical NWs up to 80 %. To our knowledge, this is the first time that such an homogeneity was obtained for MBE-grown ZnTe NWs, and the first time that a pre-treatment is applied to the catalysts in VSS method. It is unlikely that the interpretation usually proposed for VLS (the increase of the Zn content above the threshold of nucleation) be valid here. X-ray diffraction preliminary data identify a change of the relative orientation between the solid catalyst and the growth substrate.

CHAPTER 3

Growth of ZnTe/CdTe nanowire/quantum dot heterostructures

Contents

3.1 Introduction 44
3.2 Growth by molecular beam epitaxy of ZnTe/CdTe NW/QD 45
3.3 Characterization of thin CdTe QDs 49
3.4 Growth of CdTe QDs as a function of temperature 53
3.5 Growth of CdTe QD as a function of time 60
3.6 Discussion and conclusion 64

This Chapter deals with the ZnTe/CdTe NW/QD growth by molecular beam epitaxy. A short introduction is given in section 3.1. The experimental conditions along with the recipes used for the growth are detailed in section 3.2. Then, in the two sections 3.4 and 3.5, the experimental results about the temperature and the growth time dependence on the final length of the CdTe QD respectively are explained. The results are finally discussed in section 3.6 considering which are the different contributions to the growth rate for CdTe in the NW configuration.

3.1 Introduction

Nanowire-quantum dots (NW-QD) consist of nanometer sized insertions of a low energy gap semiconductor in a large energy gap nanowire. This kind of semiconductor heterostructure has attracted attention due to possible application as single photon sources at room temperature. The nanowire geometry allows to easily align several quantum dots to obtain their electronic coupling, which is more difficult to achieve using the Stransky-Krastanov growth method.

The main advantage of the CdTe/ZnTe system is the possibility to introduce magnetic Mn dopants into the crystalline structure to realize a diluted magnetic semiconductor (DMS). The possibility to form a magnetic polaron has already been demonstrated in the NPSC group during the PhD of Pamela Rueda and Alberto Artioli. Therefore, the control of the growth of optically active CdTe quantum dots in nanowires is an important step toward the control of the physical properties of Mn doped CdTe quantum dots.

A great opportunity is the possibility to choose the orientation of the polaron magnetic moment via the hole anisotropy, being able to control the quantum dot shape. In DMS alloys with a large spin orbit coupling, holes have a total kinetic momentum $J = 3/2$. In anisotropic quantum dots, the kinetic momentum degeneracy is lifted and the hole ground state is split into a heavy hole (S_z=$\pm 3/2$) and a light hole state (S_z=$\pm 1/2$). Flat quantum dots (L/D <1) promote heavy hole ground states with a large hole spin susceptibility along the growth axis. Elongated quantum dot (L/D >1) promote light hole ground state with a large hole spin susceptibility perpendicular to the growth axis [46, 47]. The control over the quantum dot shape would also give the opportunity to design the dipole associated to an electron-hole pair (through the nature of the hole), hence the selection rules of the optical transition, so that we can shape the emission diagram or obtain a lambda-configuration for the manipulation of a resident carrier through the charged exciton.

The control of the growth of NW-QD heterostructures is directly related to the quality of the interfaces between the two materials, which depends on the growth mechanism and control on the conditions used. The growth of sharp heterostructures in nanowire geometry using the VLS growth is challenging due to the reservoir effect: the residual atoms present in the liquid catalyst causes a broadening of the interfaces between the two heterostructure. It has been recently shown [48] that in the case of Ga catalyzed GaAs/GaP NWs grown by molecular beam epitaxy different effects have to be taken into account: since the solubility of As and P elements in liquid Ga at the growth temperature is low, the reservoir effect is also small and it is mainly due to the residual pressure of group V elements in the chamber. Indeed it is possible to reduce the interface extent from 15 ML to 2 ML with an appropriate switching of the fluxes [48]. The reservoir effect can also be used to improve the relative content of Al in $Al_xGa_{1-x}As$ insertions with a prefilling of the Ga catalyst with Al and reducing the growth rate by

lowering the As flux to 10% of its value [49].

The possibility to grow sharp interfaces was reported in the Si/Ge system using the VSS growth method [50]. In the case of VSS, the quantity of atoms present in the catalyst is much less and the reservoir effect is less important.

The growth of ZnTe nanowires with a CdTe insertion has been realized during the PhD of Pamela Rueda, in the VSS growth method. Important results were achieved in our group: the fabrication of CdTe QDs with different length (12 nm and 80 nm), single photon emission [9], light-hole emission [51, 52], insertion of Mn and observation of magnetic polaron associated to the light hole [9].

The remaining problems are:

- a true control of the growth rate of CdTe and of the interface sharpness;
- the elimination of the formation of lateral QDs [30, 26] which somehow poison the photoluminescence spectra introducing parasitic lines.

The objectives of this Chapter are thus:

- to obtain a systematic study on the growth of CdTe QD;
- to optimize the growth conditions preserving the shape of NW, without kink;
- to control the dimension and the aspect ratio of the CdTe QD;
- to achieve the control over the abruptness of interface;
- to avoid the radial regrowth which could give rise to parasitic QDs of not-controlled composition.

This study was started because different series of samples of ZnTe NWs embedding a single CdTe QD were prepared, and also series of samples embedding multi-QD structures, but a problem of reproducibility from sample to sample was found. In the following we will consider three samples that were analyzed in detail using TEM and EDX, that are representative of the essential properties of CdTe QD growth.

We will compare our results with the state of the art in the literature in section 3.6.

3.2 Growth by molecular beam epitaxy of ZnTe/CdTe NW/QD

For the growth of a CdTe QD in a ZnTe NW we tried to avoid complex growth sequences, so we used the optimal growth temperature for ZnTe NWs, exploring the range between 350 and 375°C. The procedure of growth of ZnTe was already described in the previous chapter, in section 2.1.3. The standard growth sequence for a CdTe axial heterostructure growth is to open the CdTe cell shutter right after the closure of the ZnTe cell without changing the growth temperature, and the same applies for the second

interface. In this way we avoid keeping the sample under vacuum at temperatures above 350°C, where the evaporation of atoms of Cd and Te is significant.

In this study I focused on the growth of multi-QD structure with different targets: first to grow CdTe QDs with different aspect ratio by changing the size of the QD. The diameter is determined by the contact area of the gold catalyst with the NW, so the parameter we can use to change the aspect ratio is the length of the CdTe QD (with the growth time); then the second important objective is to find which is the optimal temperature window for the growth of CdTe QD.

The results obtained in three samples will be considered here: a sample with thin CdTe QD insertions, another where the growth temperature was different for each CdTe insertions, and the third was grown changing the time for each CdTe insertion.

Growth conditions of sample M3194

Sample M3194, already presented in the previous chapter 2.1.3, was grown at 350°C using gold catalyst prepared by dewetting in vacuum. During the growth of the ZnTe NW (stoichiometric flux from the ZnTe cell), we inserted 10 thin CdTe sections (stoichiometric flux from the CdTe cell) without changing the growth temperature of 350°C, forming a periodic crystal structure. The flux for the CdTe compound cell was calibrated by RHEED oscillation on a reference sample of CdTe(100) as 0.5ML/s at 300°C. The growth time for the CdTe insertions was 20 seconds. Since we used stoichiometric growth conditions for the ZnTe, in this sample we can observe both WZ and ZB NWs. SEM images 2.3 can be found in the previous chapter.

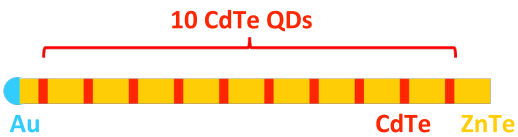

Figure 3.1: Growth recipe of sample M3194, with 10 CdTe sections used as markers. The experimental procedure is explained in section 2.1.3. The size of the CdTe sections was increased in this scheme to be clearly visible.

Growth conditions of sample M3372

Sample M3372 was prepared to study the effect of the temperature on the size of CdTe sections grown at different temperatures in the range of 25°C from 375 to 350°C. The flux for the CdTe compound cell was calibrated by RHEED oscillation on a reference sample of CdTe(100) as 0.5ML/s at 300°C. The growth time was equal to 90 seconds for all the CdTe parts, but it was changed for the ZnTe segments according to the recipe of Fig. 3.2, as a reference to identify the break point or missing sections for dispersed NWs. The expected length for ZnTe parts are calculated from the growth rate of ZnTe in sample M3194, considered in section 2.2.

After 5 minutes of dewetting of gold under Zn flux of 0.4ML/s at 350°C, the substrate temperature was rapidly increased up to 375°C under Zn flux, and the growth was started closing the Zn shutter and opening the ZnTe. After the first CdTe insertion, half of the ZnTe segment was grown, then the growth was stopped for 5 minutes to stabilize the temperature at 370°C, then it was restarted by growing the second half of the ZnTe segment. This was repeated for all the CdTe sections by steps of 5°C, in order to have the growth of each one at a different temperature, as indicated in the recipe of Fig. 3.2. Fig. 3.3 shows SEM images of the as grown sample.

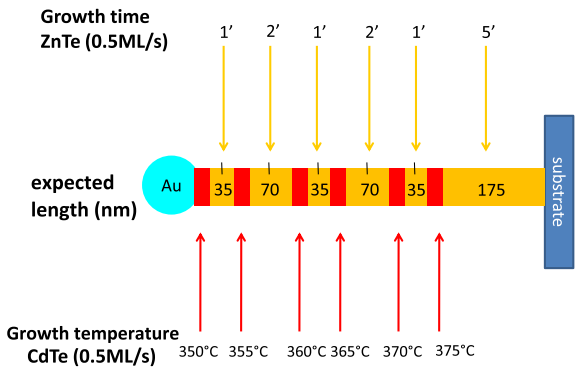

Figure 3.2: Growth recipe of sample M3372 with the growth times and the expected length, according to the measurement of the length of the ZnTe sections of sample M3194 (see Fig. 2.8). The growth was interrupted for 5 minutes in the middle of the ZnTe parts (black lines) to change and stabilize the temperature.

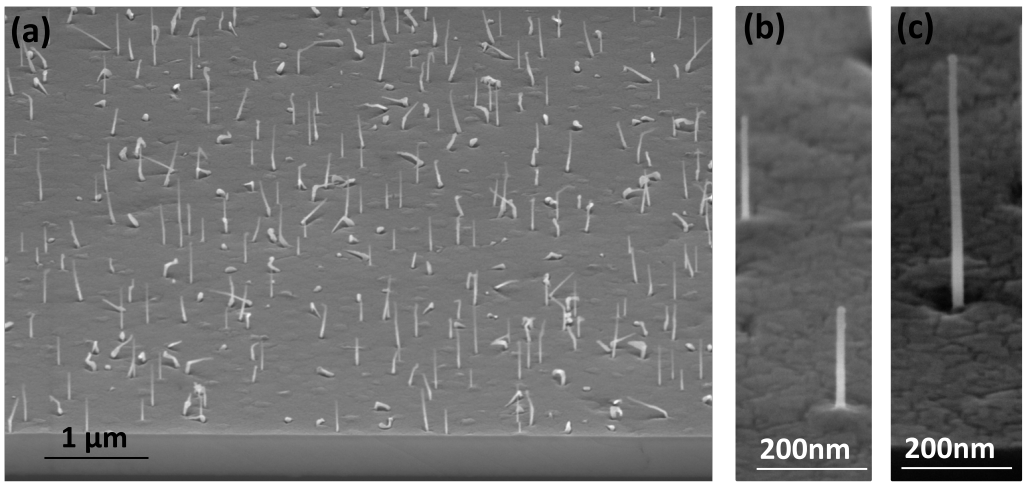

Figure 3.3: SEM Image of sample M3372, with the as grown sample tilted at 65°. The density of objects on the sample is low. Pictures (b) and (c) show WZ and ZB NWs respectively that can be distinguished from the presence of a pyramid or a deep at the base.

Despite the growth interruption during the ZnTe NW portions to change the temperature, the NWs are not perturbed by kinks, as can be observed by the SEM image of Fig. 3.3.

Growth conditions of sample M3330

Sample M3330 was used to study the relationship between the growth time and the length of the CdTe QDs. After 5 minutes of dewetting of gold under Zn flux of 0.4ML/s at 350°C, the substrate temperature was rapidly increased up to 375°C and the growth was started. Actually the temperature was probably lower, see discussion 3.6. In the scheme of Fig. 3.4 the growth recipe is explained. The growth sequence of ZnTe has been chosen as a reference to identify the break point or missing sections for dispersed NWs. The expected length for ZnTe parts are calculated from the growth rate of ZnTe in sample M3194, considered in section 2.2. The growth time of the first CdTe insertion was 20 s, 1 min for the second, and for each following CdTe part the time was doubled with respect to the previous up to 8 min.

The flux for the CdTe compound cell was calibrated by RHEED oscillation on a reference sample of CdTe(100) as 0.5ML/s at 300°C. In this case we used an excess of Cd during the growth of the QD to compensate the re-evaporation of Cd at this temperature. Fig. 3.5 shows SEM images of the as grown sample.

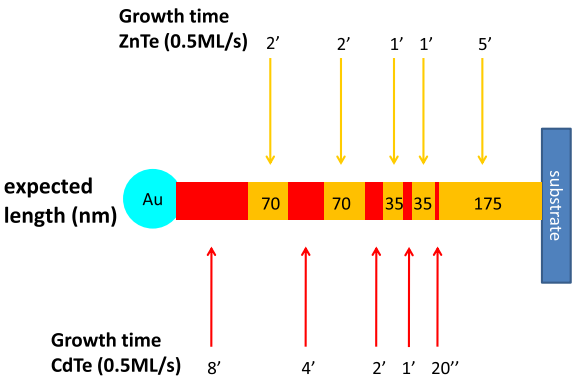

Figure 3.4: Growth recipe of sample M3330 with the growth times and the expected length, according to the measurement of the length of the ZnTe sections of sample M3194 (see Fig. 2.8).

The NWs were characterized using TEM, in particular to access the crystal structure and lattice parameter variations (GPA of HR images by Martien den Hertog) and the composition of the QD (EDX by Eric Robin). We will now describe the results.

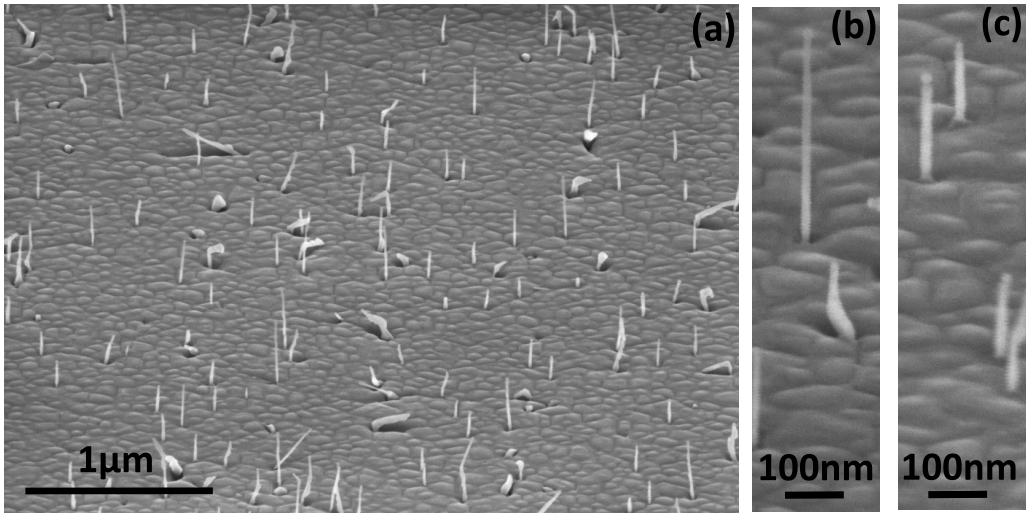

Figure 3.5: SEM Image of sample M3330, with the as grown sample tilted at 65°. The density of objects on the sample is low. Pictures (b) and (c) show ZB and WZ NWs respectively that can be distinguished from the presence of a deep or a pyramid at the base.

3.3 Characterization of thin CdTe QDs

NWs from sample M3194, as already discussed in section 2.2, have been characterized by TEM both with HR-EDX hypermaps, see Fig. 2.7, and with GPA of high resolution images, see Fig.2.8. The CdTe insertions in this sample were grown for a short time of 20 seconds, so they are very thin. In this section we are interested in the determination of the CdTe insertions dimension as well as on the abruptness of the ZnTe/CdTe interfaces, while in Chapter 2 the interest was the determination of the average distance between the CdTe insertions, used as markers.

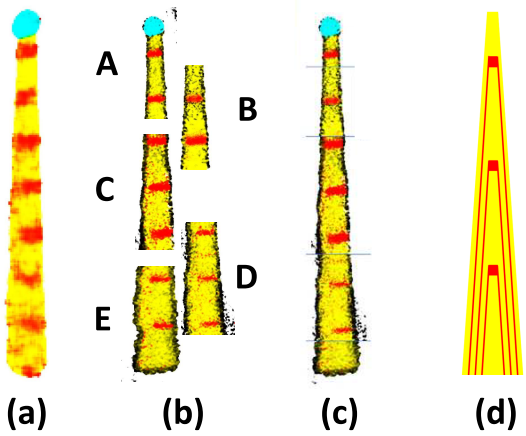

Figure 3.6: (a) low resolution EDX image of a NW (probably inclined) deposited on a holey carbon grid and (b) 5 high resolution images of the same NW corresponding to EDX hypermaps. Colored areas are those where the Cd (red), Zn (yellow), Au (cyan) or O (black) signal exceeds an arbitrary threshold. (c) composite EDX map reconstructed form the individual sections of (b); (d) geometrical model considered for data analysis.

At first I will consider the characterization with the EDX method. I have shown in Fig. 2.7 a composite EDX map of a NW (probably inclined) of sample M3194. Fig. 3.6 shows a more complete set of images for the same NW. The determination of the size of the QD region is challenging due to the difficulty of the hypermap analysis. In particular, the axial profiles of Cd concentration can be extracted from the high-resolution hypermap of Fig. 3.6 (b), using a proper integration region with uniform composition, as explained in Chapter 1.

For instance let us consider in Fig. 3.7 (a) (black points) the profile of a single insertion, the one at the top of the NW. The profile shows the Cd concentration, calculated considering that the region where the Cd EDX signal is integrated is smaller than the effective radius of the rich-Cd region (L_{Cd}) and it has been normalized with respect to the NW tip diameter $2R_0$, under the assumption that it is equal to the QD diameter. The ideal structure of the NW is shown Fig. 3.6 (d).

The profile shows an asymmetry with respect to the position and a simple Gaussian line-shape cannot fit our data. We use a line-shape for the interfaces taking into account the reservoir effect of the gold catalyst: we consider the convolution of an error function and an exponential tail, broadened by a Gaussian taking into account the experimental error of the measurements or a possible inter-diffusion broadening. The equation used for the curve fit (red line) of Fig. 3.7 (a) is:

$$g(x) = \frac{1}{2}\left[1 - \mathrm{erf}\left(\frac{x}{\sqrt{2}\sigma}\right)\right] + \exp - \left[\frac{x}{\tau} - \frac{\sigma^2}{2\tau^2}\right]\frac{1}{2}\left[1 + \mathrm{erf}\frac{1}{\sqrt{2}\sigma}\left(x - \frac{\sigma^2}{\tau}\right)\right] \tag{3.1}$$

where x is the position of the center on the insertion in nm in the line profile, τ is the exponential decay and σ is the Gaussian broadening.

For the top CdTe insertion the best fit is obtained for σ=2 nm, τ=3.5 nm. In Fig. 3.7 (b) the same data (black points) are compared with the model for a CdTe QD with a large thickness so that the Cd concentration reaches 100% in the CdTe insertion.

The plot of Fig. 3.8 shows the Cd concentration profile along the axial direction of the NW from the different EDX images of Fig. 3.6 (b). The sketch of Fig. 3.6 (d) is the geometrical model used to interpret the profiles: for each peak, the same line profile of Eq. 3.1 is used (as fitted for the top CdTe QD), multiplied by factor taking into account that the volume of the NW at the position of the CdTe QD is partially constituted of a ZnTe shell, while the increasing background takes into account the presence of a CdTe shell with increasing volume towards the base of the NW due to lateral regrowth. The agreement with experimental data is rather good and validates the line-shape used for the interface.

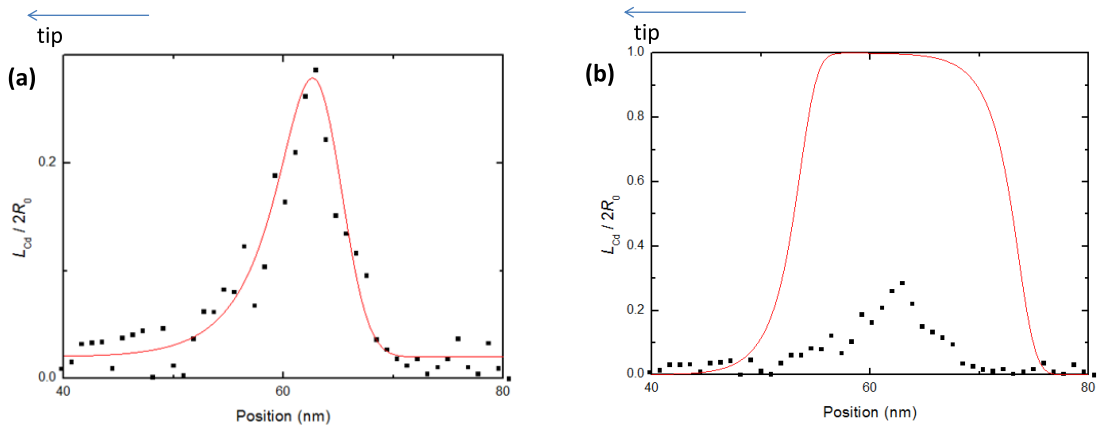

Figure 3.7: Cd concentration axial profile from EDX hypermaps of the top CdTe insertion of sample M3194, normalized as explained in the text for the effective diameter of the rich-Cd region. Black points (a) and (b) are experimental data . The red curve (a) is a fit obtained using equation 3.1, with an interface distance of 2.1 nm, a tail due to reservoir effect of 3.5 nm and a Gaussian broadening of 2 nm. The red curve (b) is calculated for a longer CdTe QD for the sake of comparison.

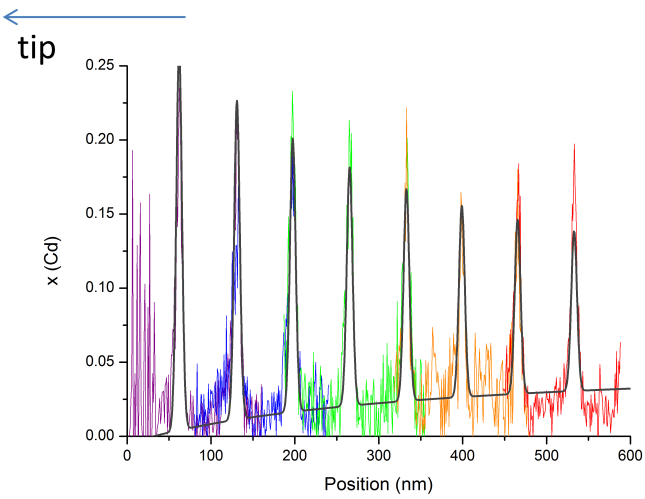

Figure 3.8: Cd concentration profile along the axial direction of the NW from the different EDX hypermaps of Fig. 3.6 (b). The curve fit for each peak uses equation 3.1, multiplied by a factor taking into account that the volume of the NW at the position of the CdTe QD is partially constituted of a ZnTe shell. The increasing background takes into account the presence of a CdTe shell.

As shown in Fig. 3.9 (c), the model of Eq. 3.1 describes as well the profiles from a HR-GPA image of NW2, shown in Fig. 2.8 (a). In this case the values for the interface distance and tail are smaller (interface distance of 1.4 nm and tail of 1.6 nm), probably because the NW analyzed by EDX was grown inclined (with different effective flux contributing to axial grow). Data are shown as a function of the lattice parameter of the crystal, equal to 0.352 nm for ZnTe and 0.372 for CdTe. The height of the peak (lattice parameter) confirms that this insertion is not constituted of 100% of CdTe. Note

the area in the reciprocal space (FFT of image 3.9(a), not shown) for insertions that are so small, determines the number of lattice planes over which the GPA (thus the difference in lattice spacing with respect to ZnTe lattice planes distance) is averaged. The resulting number of planes should not to be taken greater than the QD size (in real space) otherwise, since the integral under the peak remains constant, the lattice parameter in the CdTe region would be underestimated, nor too small, to avoid the prevalence of noise.

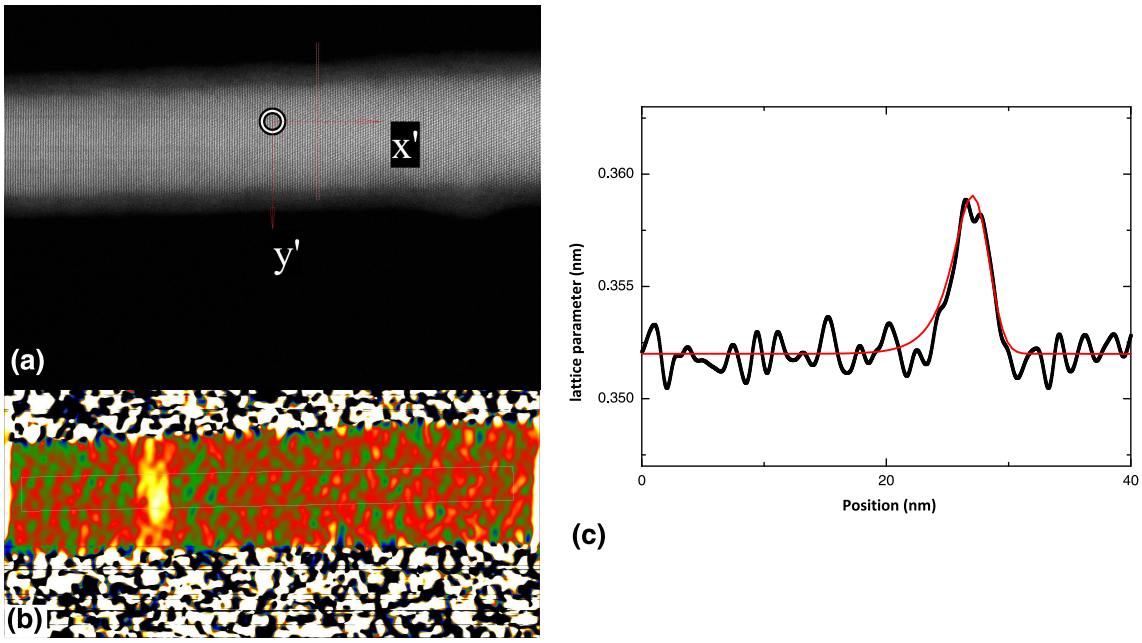

Figure 3.9: (a)HR-TEM image of NW of Fig. 2.8 (a). (b) corresponding GPA image obtained with a probe size of 6 MLs (c) black squares are experimental data of lattice parameter axial profile from GPA of a ZB NW. The curve fit (red curve) is obtained using equation 3.1, with an interface distance of 1.4 nm, a tail due to reservoir effect of 1.6 nm and a Gaussian broadening of 1 nm.

We can now use data from the fit of Fig. 3.7 (a) and 3.9 (c) to estimate the Cd concentration in the gold catalyst at the moment of the growth for the two CdTe QDs. This is done by calculating the ratio between the number of Cd atoms in the exponential tail and the number of Au atoms in the NP. This is equivalent to dissolve, in the gold nanoparticle, the Cd atoms of an equivalent cylinder of CdTe with height given by the tail integral. The number of Au atoms in the NP is calculated from the volume of the Au NP (quasi-full-sphere shape), multiplied by the number of Au atoms in the fcc unit cell (4 atoms) and divided by the volume of the unit cell (lattice parameter a_{Au}=0.4065 nm). In a similar way, the number of Cd atoms is obtained considering a cylinder of CdTe with height equal to the exponential tail integral (equal to tau) multiplied by the section of the NW to obtain the equivalent volume of CdTe, multiplied by the number of Cd atoms in the unit cell of ZB CdTe, divided by the unit cell volume (a_{CdTe}=0.648 nm).

- for NW of Fig. 3.7 (a), we obtain a concentration x=2%, with τ=3.5nm, d_{NP}=33nm and with d_{NW}=24nm, as measured from TEM images of the NW (not shown).
- for NW of Fig. 3.9 (c), we obtain a concentration x=1.5%, with τ=1.6nm, d_{NP}=13nm and with d_{NW}=7.5nm, also in this case measured from TEM images (Fig. 2.8 (a)).

We interpret this result by ascribing τ to the reservoir effect, that is expected to be small for a solid catalyst. The NW of Fig. 3.7 (a) is probably not vertical (the nanoparticle diameter is quite big and the shell regrowth is not symmetric), and the value obtained for the concentration is an upper limit. A tentative interpretation of σ could be also an inter-diffusion broadening, but the growth temperature is too low to induce bulk-type inter-diffusion; this could be enhanced during growth, and we have not the information if the interface is totally flat.

In summary we have shown that the analysis on the QD size requires: (1) the choice of the geometrical model for the NW, taking into account possible radial regrowth and (2) a model for the interface profile. From the interface profile model, attributing the exponential tail to the reservoir effect, we can estimate an upper limit of 2% of Cd concentration in the gold nanoparticle.

3.4 Growth of CdTe QDs as a function of temperature

In this section I will consider sample M3372 (growth recipe in section 3.2). In Fig. 3.10, we show EDX axial profiles for different NWs of this sample. The NWs were mechanically dispersed on a holey carbon grid from the as-grown sample. For each NW, the different CdTe insertions can be observed as a peak in the normalized Cd concentration (red curve) and a dip in the normalized Zn concentration (yellow curve). Corresponding EDX maps and TEM images are shown on the right. The curve fit are obtained with the model explained in the previous section 3.3, using an exponential tail (2 nm) broadened by a Gaussian (0.5 nm, HWHM 1.2 nm) for all the peaks, and the maximum intensities are obtained using a multiplicative factor that takes into account the presence of a shell, as shown in the geometrical model of Fig. 3.6 (d). Vertical lines are used as eye-guides to visualize the difference of the position of Cd peaks (note that the first interface (Au/CdTe) is aligned on the left vertical line for all graphs).

As it can be observed in Fig. 3.10, even if in the growth recipe the CdTe insertion were grown all for the same time, the length is quite different as a function of the temperature. A summary of the obtained length for ZnTe and CdTe is shown in Fig. 3.11. The length of ZnTe segments (with a factor 1/2 for the second one for which the growth time was doubled) of Fig. 3.11(a) presents two sets of data, with average values 29 nm and 38 nm. That can be related to a different contact area between the NP and the NW, as already mentioned with the half-sphere shape of the NP on the wurtzite NWs, and the random change between half-sphere and full-sphere for the zinc-blende NWs.

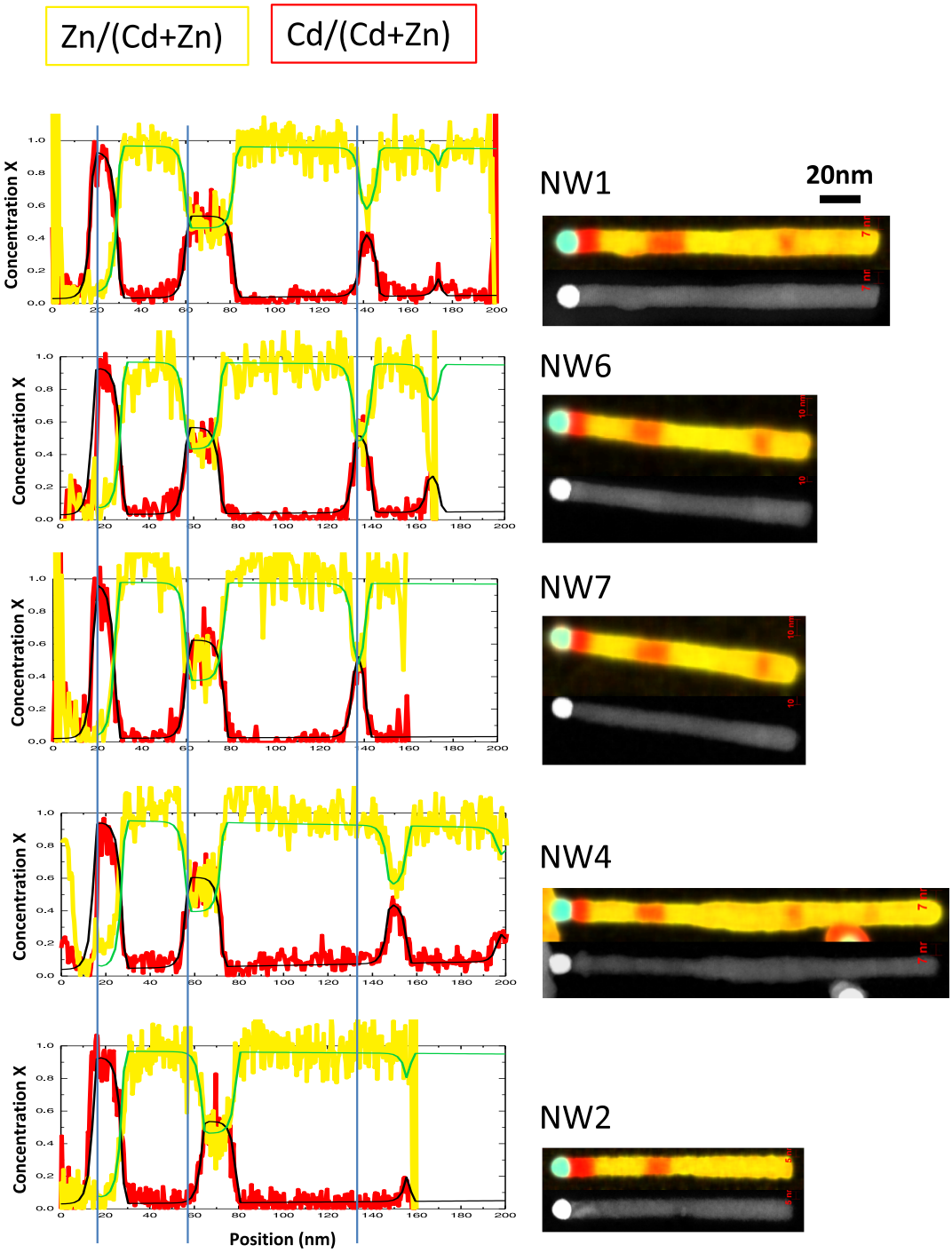

Figure 3.10: Axial profile for different NWs from sample M3372; experimental data of Zn (yellow line) and Cd (red line) concentrations normalized to Cd+Zn. The curve fit are calculated using an exponential tail (2 nm) broadened by a Gaussian (0.5 nm, HWHM 1.2nm) common to all. Maximum intensities are represented by a multiplicative factor. On the right, the corresponding TEM images and EDX maps with colors for different elements: Cd (red), Zn (yellow) and Au (cyan). The scale bar is the same for all the images.

The length of CdTe shows that the segment grown at 355°C is quite uniform, except for NW1. For all the NWs this is the longest CdTe segment. The one at 360°C is definitely shorter, particularly for NW2. The one at 365°C is even shorter. The effect of temperature is clear and strong. In any case we were able to observe the first CdTe insertion at 375°C, or the second one at 370°C. In spite of the lower temperature, the segment at 350°C is shorter. This is probably due to re-evaporation or re-dissolution of CdTe during the cooling of the sample after growth.

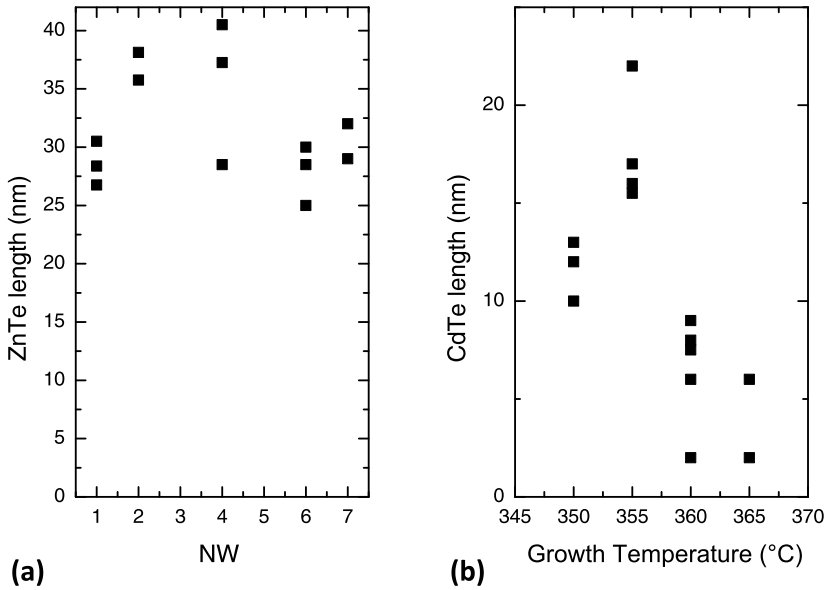

Figure 3.11: (a) ZnTe length per minute of different NWs and (b) CdTe length as a function of growth temperature determined from Fig. 3.10.

As explained in Chapter 1, the EDX raw data consist in a hypermap where each pixel is a spectrum integrated along the electron beam at a given position of the beam. From these spectra, the analysis extracts, for each position of the electron beam, the number of atoms of Cd, Te, Zn, O, Au present over the length of the electron beam. A proper calibration using the method of ζ-factors, allows one to translate this into an equivalent length of pure material. From that we can obtain: the total thickness of the NW crossed by the e-beam, by summing over all elements and the relative amount of the different elements, integrated over the e-beam, by calculating the proper ratio. We can also build a model and adjust the shapes, sizes and compositions in order to fit these data.

In Fig.s 3.12, 3.13 and 3.14 we can find the radial profiles measured on NW6. The top image is the EDX color map of the element distribution in the NW. In the image 3.12, the HR-EDX hypermap at the region 3, is analyzed, from the right to left, below the QD, in the CdTe QD and over the QD region. The Zn, Cd, and Te profiles represented by blue open circles, are obtained from the hyper-map by integrating the EDX spectra for the corresponding element along the line profile shown by the blue arrow, in the NW volume indicated by the blue box. We are assuming that inside the box the NW has a

uniform composition in the axial direction. The radial profiles are fitted using a model for the NW geometry. We assume a core shell structure with hexagonal section, like in Fig. 3.6 (d). As shown by the blue fit curves, the elemental profiles can be fitted with shells of different composition and thickness. The three different elements are fitted at the same time. By summing over all elements the plot giving the total NW thickness is obtained (black open circles) while the black curve is the profile obtained with the shape of an hexagon oriented as shown.

The results in the plots at the bottom of the figure, give the NW structure that best fit the experimental data. The concentration of Cd in each shell is indicated as well as the number of Cd atoms in a nm thick slice. Fig.s 3.13 and 3.14 show the results for the others CdTe QDs of NW6. The analysis of this NW evidences:

- a rich-Te shell around the NW that has probably prevented the sample from oxidation;
- in region 3, the presence of a CdTe/ZnTe/CdTe shell around the ZnTe bottom segment, and at the CdTe region, the presence of a $Cd_{0.85}Zn_{0.15}Te$ core surrounded by different shells;
- for region 2, in Fig. 3.13 also a $Cd_{0.87}Zn_{0.13}Te$ core;
- in region 1 below the gold nanoparticle shown in Fig. 3.14, it is possible to observe that the shape of the QD when approaching the surface of the NW, is elongated toward the bottom with a CdTe almost pure shell around a $Cd_{0.86}Zn_{0.14}Te$ core.

Probably the resolution of EDX is not enough to measure the actual thickness of the CdTe shell due to lateral regrowth, but the integrated Cd content corresponds to less than 1 ML of CdTe. Shells much richer in Cd (corresponding to up to 7 ML of CdTe) have been measured in previous samples, grown with a strong lateral flux [30].

The main results of this section are:

- a strong effect of temperature ove a very small window, indeed much smaller than the reproducibility from Molyblock to Molyblock;
- the very small thickness to which the CdTe shell can be decreased.

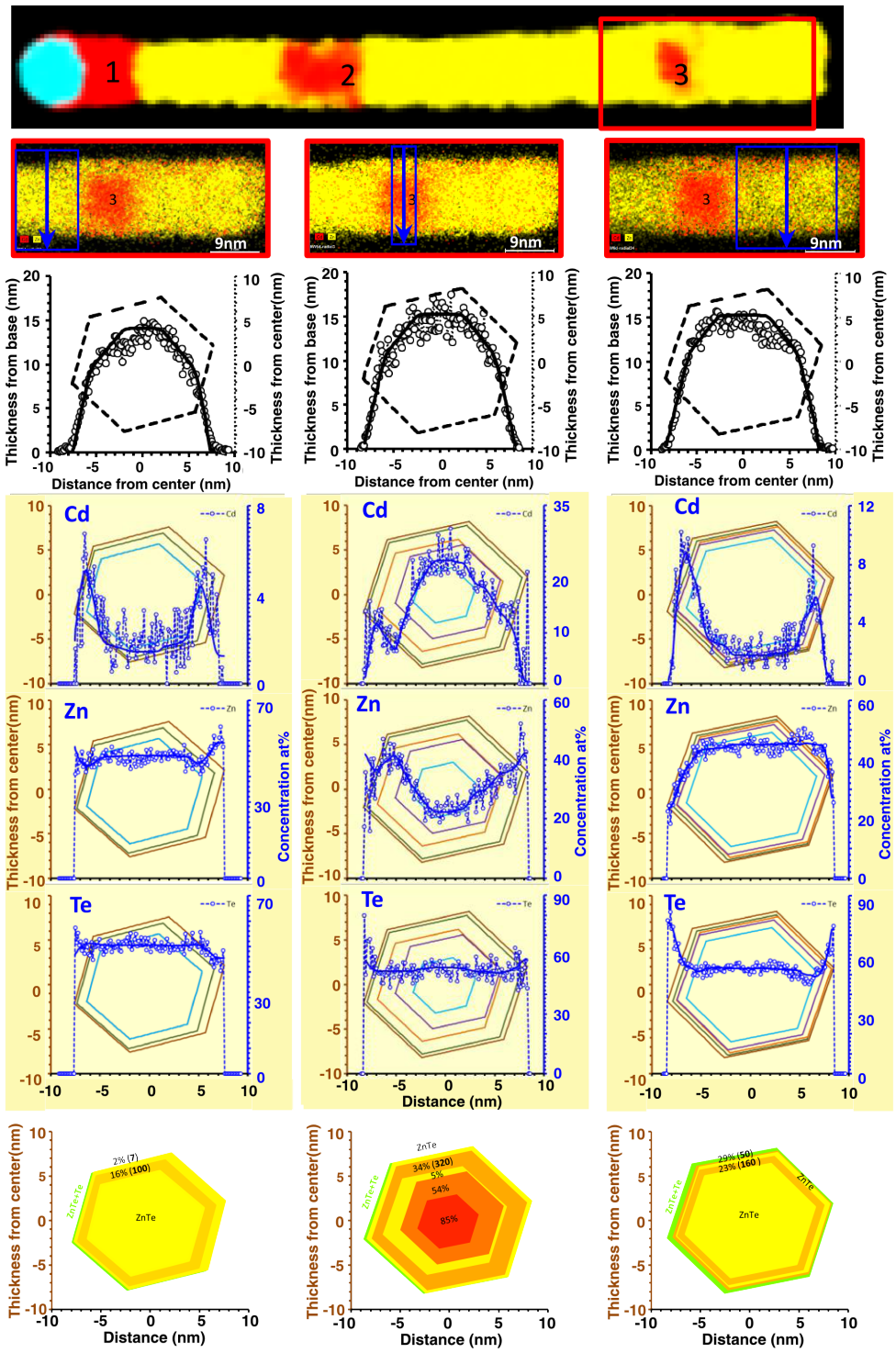

Figure 3.12: EDX image of NW 6 from sample M3372. Analysis of region 3. Colored areas are those where the Cd (red), Zn (yellow), Au (cyan) or O (black) signal exceeds an arbitrary threshold. The blue curves are the radial profiles measured on HR-EDX hypermaps (indicated by blue arrows and integrated in the blue boxes). A geometrical model with hexagonal section and different shell is used to reconstruct the structure of the NW by fitting of the radial profiles for the different elements.

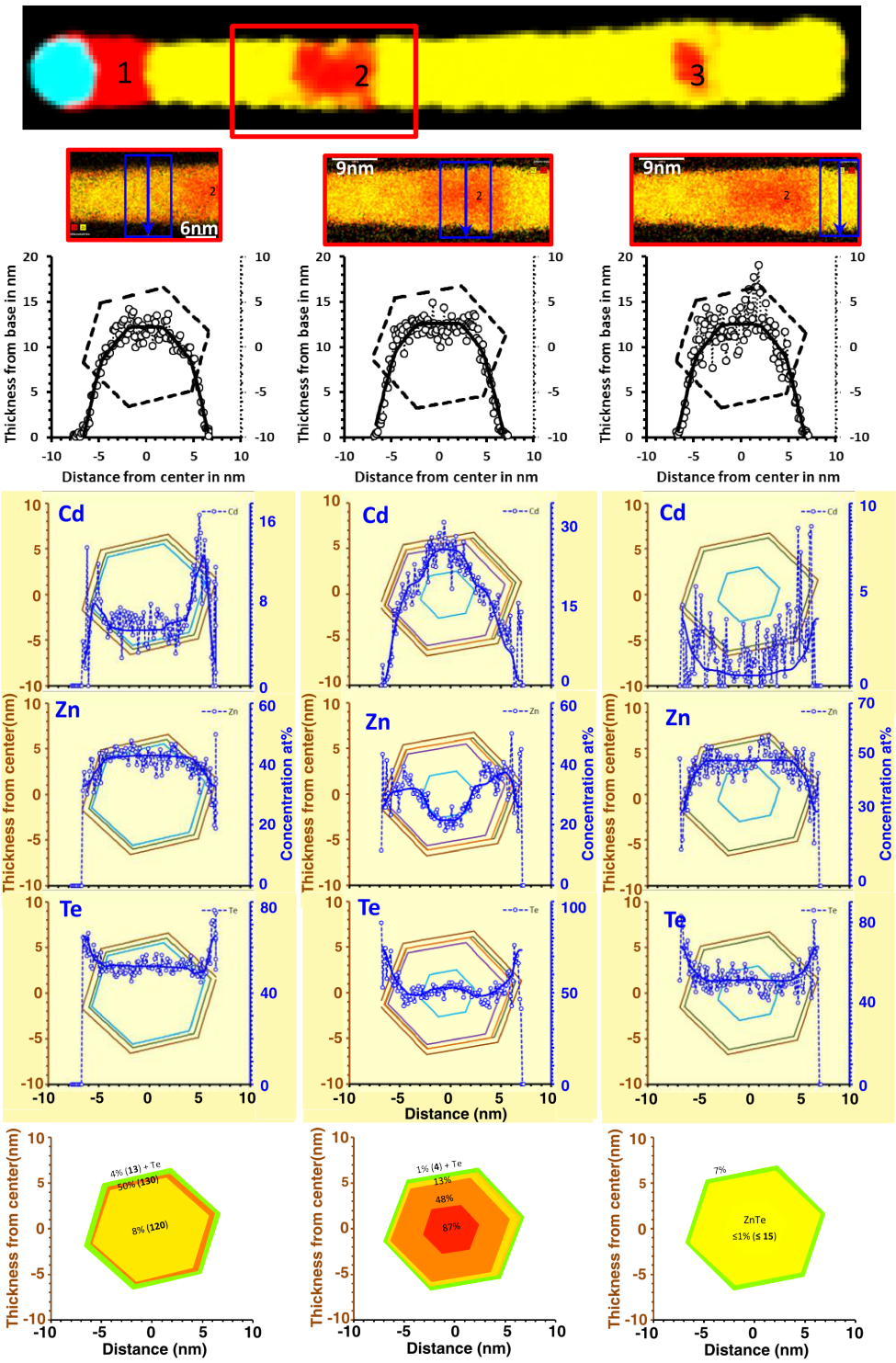

Figure 3.13: EDX image of NW 6 from sample M3372. Analysis of region 2. Colored areas are those where the Cd (red), Zn (yellow), Au (cyan) or O (black) signal exceeds an arbitrary threshold. The blue curves are the radial profiles measured on HR-EDX hypermaps (indicated by blue arrows and integrated in the blue boxes). A geometrical model with hexagonal section and different shell is used to reconstruct the structure of the NW by fitting of the radial profiles for the different elements.

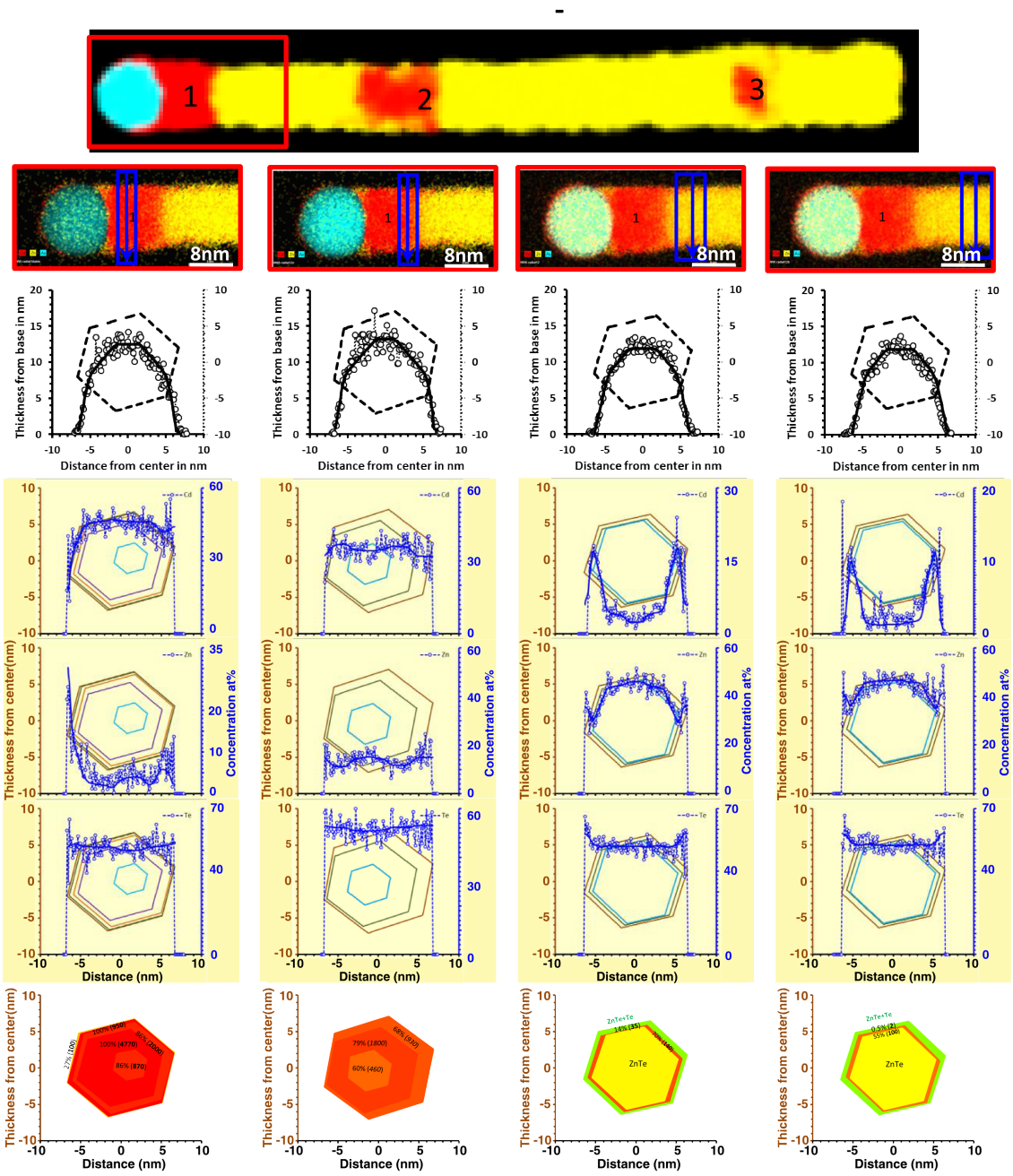

Figure 3.14: EDX image of NW 6 from sample M3372. Analysis of region 1. Colored areas are those where the Cd (red), Zn (yellow), Au (cyan) or O (black) signal exceeds an arbitrary threshold. The blue curves are the radial profiles measured on HR-EDX hypermaps (indicated by blue arrows and integrated in the blue boxes). A geometrical model with hexagonal section and different shell is used to reconstruct the structure of the NW by fitting of the radial profiles for the different elements.

3.5 Growth of CdTe QD as a function of time

Sample M3330 was grown at a fixed temperature, but the growth time of the CdTe segments was changed, as shown in the sketch of Fig. 3.4. The temperature is determined within an error of ±10°C in the growth chamber; this range of temperature is quite large compared with the results on the previous section. The nominal growth temperature of sample M3330 was 375°C, but probably the real temperature was lower.

The as grown NWs were mechanically dispersed on a holey carbon grid and analyzed by EDX. In Fig. 3.15 are shown the EDX color map of a NW, with the plot of the Cd concentration from a profile extracted along the growth axis. Starting from the gold catalyst (left of the image) towards the right, the CdTe QDs with growth time of 8, 4 and 2 minutes are visible. The NW is broken in the correspondent QD with growth time of 1 minute. To obtain quantitative information about the length of the CdTe insertions, we used for the curve fitting the interface line shape of Eq. 3.1 and the geometrical model of Fig. 3.6. The line-shape was the same for all peaks, with τ=3 nm and σ=2 nm.

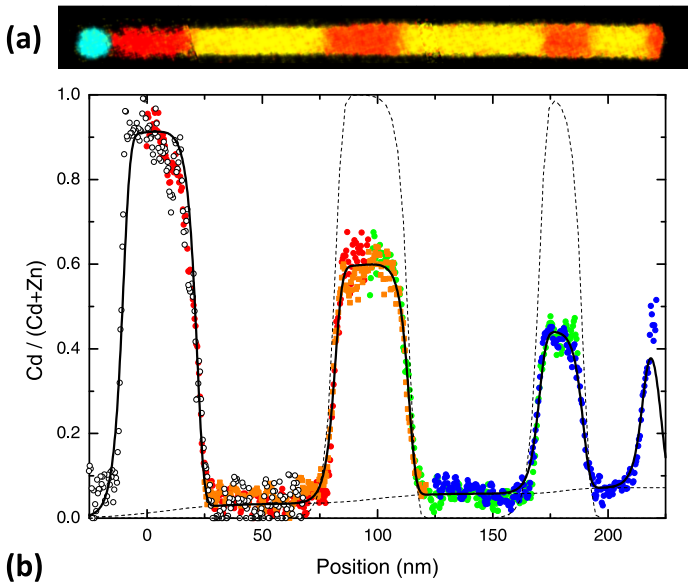

Figure 3.15: (a) EDX image of a NW from sample M3330. CdTe QDs with growth time of 8, 4, 2 and 1 minute (where the NW is broken) are visible. Colored areas are those where the Cd (red), Zn (yellow), Au (cyan) or O (black) signal exceeds an arbitrary threshold. (b) axial profiles of the Cd relative concentration measured for different HR-EDX hypermaps. The curve fit are calculated using an exponential tail (3 nm) broadened by a Gaussian (2 nm).

The curve fit allows us to estimate the length of the segments of CdTe as the distance between the two interfaces, equal to 32 nm (for corresponding growth time of 8 and 4 minutes), and 19 nm (for growth time of 2 minutes). The last CdTe segment is broken so the points (blue dots) at the right-side end are not significant. The last QD close to the nanoparticle is shorter than what expected from the recipe (this was the case also for the NWs of sample M3372, see Fig. 3.10).

The dashed line represent the peak amplitude in the case of a pure CdTe segment. In this NW, the multiplicative factor used to describe the height of the peaks, corresponds only partially to the presence of a ZnTe shell. In fact, the first CdTe segment has a composition of $Cd_{0.9}Zn_{0.1}Te$, the second $Cd_{0.75}Zn_{0.25}Te$, and the third $Cd_{0.5}Zn_{0.5}Te$, as it can be observed from the EDX radial profiles for the same NW in Fig.s 3.16 (b) and 3.17 (a) and (c). Hence the Cd concentration is higher for the last grown CdTe Qd, and decreases towards the bottom of the NW. The fact that the width of the radial Cd profile in the QD is larger and larger (see Fig. 3.17 (c) to Fig. 3.17 (a) and Fig. 3.16 (b)) suggest that it could be due to a radial interdiffusion. A similar feature appears in Fig. 3.12, as a Cd-rich shell around the QD, as compared to the Cd shell on both sides. However an axial diffusion cannot be ruled out.

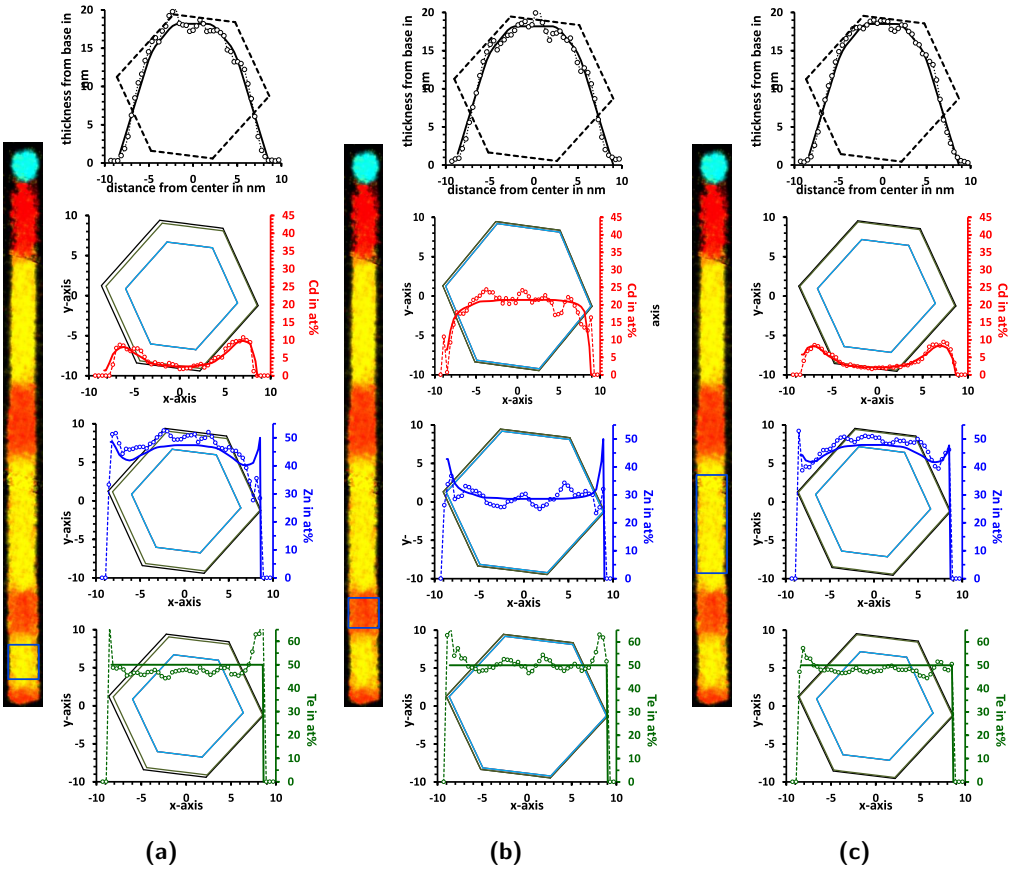

Figure 3.16: EDX radial profiles of the same NW from sample M3330 as in Fig. 3.15. Colored areas are those where the Cd (red), Zn (yellow), Au (cyan) or O (black) signal exceeds an arbitrary threshold. The element concentration are measured on HR-EDX hypermaps (integrated in the blue boxes). A geometrical model with hexagonal section and different shell is used to reconstruct the structure of the NW by fitting of the radial profiles for the different elements.

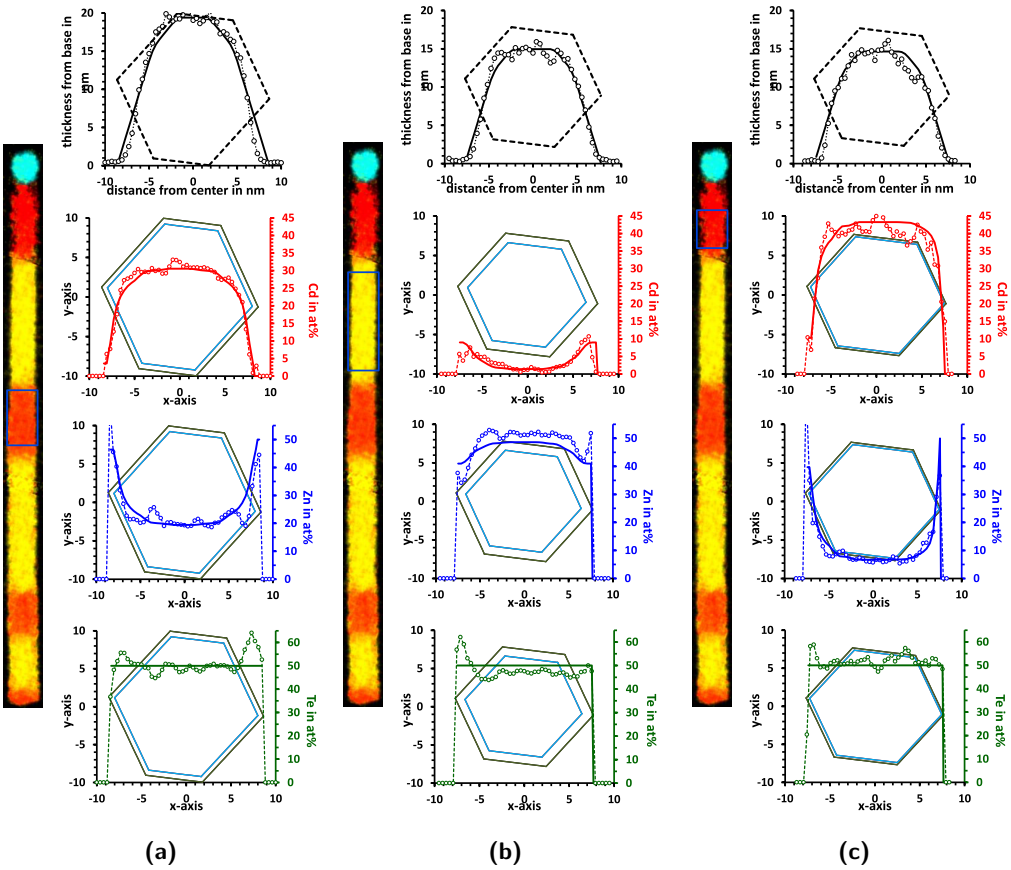

Figure 3.17: EDX radial profiles of the same NW from sample M3330 as in Fig. 3.15. Colored areas are those where the Cd (red), Zn (yellow), Au (cyan) or O (black) signal exceeds an arbitrary threshold. The element concentration are measured on HR-EDX hypermaps (integrated in the blue boxes). A geometrical model with hexagonal section and different shell is used to reconstruct the structure of the NW by fitting of the radial profiles for the different elements.

3.6 Discussion and conclusion

The experimental results on the growth of CdTe QDs show that there is a drastic effect of the temperature, in fact the growth is suppressed by a small increase of the temperature as shown by EDX results in section 3.4. This is confirmed by results of other groups of Warsaw [26, 43] and Würzburg [24] obtained at higher growth fluxes, as discussed at the end of this section.

From the size of the CdTe QD grown in different NW samples as a function of the growth time, shown in Fig. 3.18, we can estimate the growth rate of CdTe in NWs. There is a certain dispersion probably due to the difficulty to control the temperature in our MBE system. The black line is a linear fit of the experimental data, with slope of 10 nm/min i.e. in units of CdTe(100)ML, 0.5±0.2 ML/s; as the nominal growth rate (flux) of 0.5±0.02 ML/s was calibrated on CdTe (100) by RHEED oscillations, the catalyst effect is not obvious.

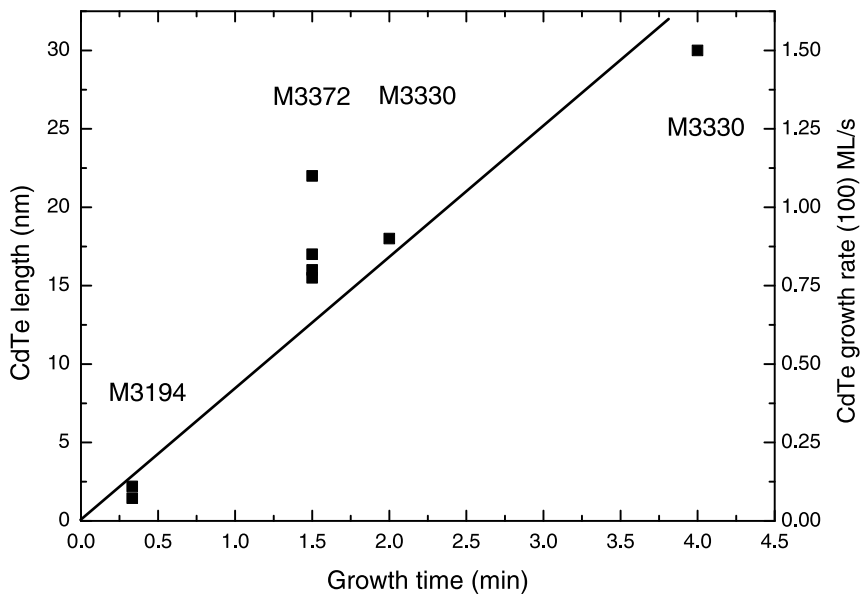

Figure 3.18: CdTe QD length as a function of the growth time for different samples.

The growth rate as a function of temperature for CdTe and ZnTe NWs is very different. The growth of ZnTe NWs was done in a temperature range from 350 to 400°C and we observed a slightly faster growth at 375°C, attributed to a longer diffusion length [31]. For CdTe the temperature dependence is extremely strong and opposite, and even a small difference of 10 degrees may affect the presence of CdTe QD.

In Fig. 3.25 we compare the growth rate of CdTe in sample M3372 and ZnTe NWs in stoichiometric and rich-Te conditions, as a function of temperature. Growth rate data are plotted with vertical scale normalized to the reference growth rate measured on (100) surface and are shown in units of ML/s instead of nm/min, for CdTe with respect to the nominal CdTe growth rate of 0.5ML/s (left vertical axis), and ZnTe with respect to the nominal ZnTe growth rate of 1ML/s (right vertical axis). The temperature error bars

correspond to the dispersion from growth to growth, thus from molyblock to molyblock. Data on CdTe QDs as a function of temperature were recorded on a single sample, so the relative temperature is well defined.

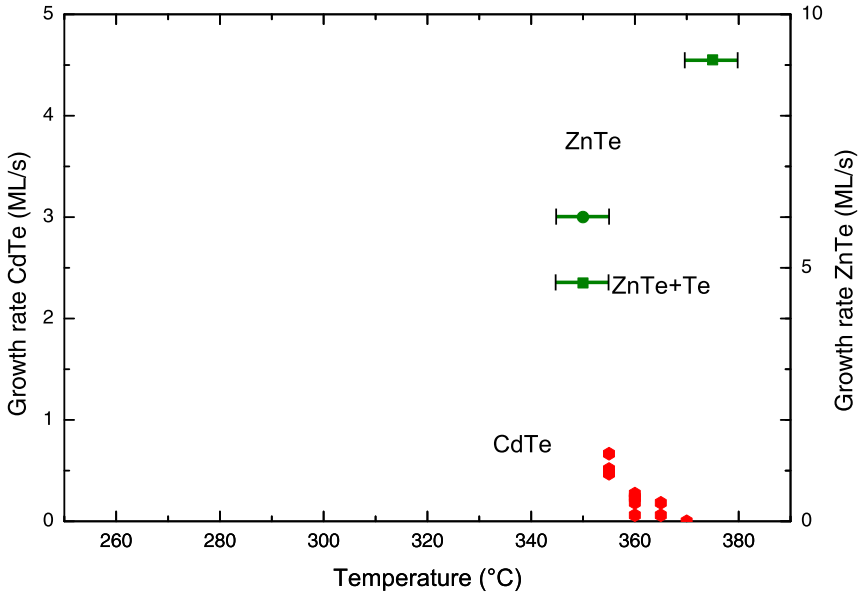

Figure 3.19: Growth rate for CdTe (red dots) with respect to the nominal CdTe growth rate of 0.5ML/s (left vertical axis), and ZnTe in stoichiometric (green dots) and rich-Te (green squares) conditions with respect to the nominal ZnTe growth rate of 1ML/s (right vertical axis).

As a first attempt to explain the different growth rates, we will now (1) discuss the effect of geometry, (2) introduce the evaporation and (3) introduce its temperature dependence. In Fig. 3.20 we summarize the contributions to growth rate for ZnTe and CdTe.

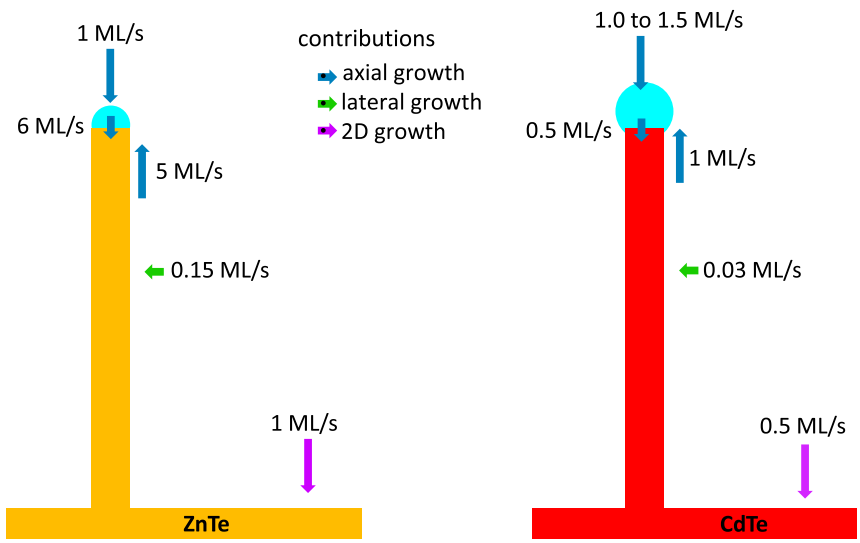

Figure 3.20: Summary of different flux contributions due to geometry of the MBE chamber for ZnTe and CdTe growth.

We define the growth rate V_0 as the nominal flux calibrated by RHEED oscillation on (100) surfaces, 0.5ML/s for CdTe and 1ML/s for ZnTe, also equal to the 2D growth contribution in Fig. 3.20 (purple arrows). The lateral flux, impinging with an angle α (between the NW axis and the flux direction), contributes by a factor $\tan\alpha$, and can diffuse to the catalyst within the diffusion length λ. Then the contribution to the growth rate by the lateral flux will be $V_r = \frac{4\lambda \tan\alpha}{\pi D_{NW}} V_0$.

The contribution from the direct impinging on the catalyst can change if we consider a half-sphere or a quasi-full-sphere catalyst. For the half-sphere catalyst, $V_{hNP} = V_0$, if we consider the diameter of the catalyst equal to the NW diameter $D_{NW} = D_{NP}$. For the quasi-full-sphere catalyst $V_{fNP} = \frac{V_0}{\cos\alpha}\left(\frac{D_{NP}}{D_{NW}}\right)^2$ with $D_{NW} = D_{NP}\sin\beta$, where β is the contact angle between the catalyst and the NW.

In summary, for ZnTe, $V_0 = 1$ML/s, $\tan\alpha = 0.48$ and $\cos\alpha = 0.90$, typical values for half-sphere catalyst $D_{NP} = D_{NW} = 10$nm:

- the contribution from the direct impinging on the catalyst is $V_0 = 1$ML/s and compensate the 2D regrowth;
- the lateral flux averaged over rotation is $V_0 \frac{\tan\alpha}{\pi} \simeq 0.15$ ML/s;
- the contribution from diffusion from NW sidewalls is $V_r = \frac{4\lambda \tan\alpha}{\pi D_{NW}} V_0 \simeq 5V_0 =$ 5ML/s, using for the diffusion length $\lambda = 80nm$ as determined in Chapter 2;
- if we assume a negligible re-evaporation from the catalyst and the NW sidewalls, the value obtained for the growth rate obtained with this value of the diffusion length fits the experimental value.

For CdTe instead we have $V_0 = 0.5$ML/s, $\tan\alpha = 0.21$ and $\cos\alpha = 0.98$:

- the catalyst is observed with a quasi-full-sphere shape, assuming a contact area as for ZnTe, the contribution from the direct impinging on the catalyst is $V_{fNP} = \frac{V_0}{\cos\alpha}\left(\frac{D_{NP}}{D_{NW}}\right)^2 \simeq 1.5$ML/s ;
- the lateral flux averaged over rotation, is $V_0 \frac{\tan\alpha}{\pi} \simeq 0.033$ ML/s;
- the contribution from diffusion from NW sidewalls, assuming the same value of the diffusion length λ =80nm as for ZnTe, is $V_r = \frac{4\lambda \tan\alpha}{\pi D_{NW}} V_0 \simeq 1$ML/s.

Since we observe a growth rate of 0.5 ML/s, much lower than the incoming flux (1 to 1.5ML/s), possible re-evaporation of Cd from the gold catalyst and re-evaporation rate of CdTe from the NW sidewalls and the substrate must be considered.

Let us consider first the re-evaporation of Cd from the Au catalyst. Cd is a volatile element with a high vapor pressure of p^0_{Cd}=40 Pa at 350°C, as compared to 2 Pa for ZnTe or 0.4 Pa for Te_2 at the same temperature.

For a half sphere particle, the evaporation flux J_e from its surface $2\pi D_{NP}^2/4$:

$$J_e = k_e \frac{p}{(2\pi M k_B T)^{1/2}} \tag{3.2}$$

where p is the vapor pressure of the element considered, for instance Cd, M its mass, k_B the Boltzmann constant, T is the temperature, and k_e is a factor representing barrier effects (in principle smaller than 1 but often omitted). This flux J_e corresponds to a decrease of the growth rate of:

$$V_{e,hNP} = k_e \frac{p}{(2\pi M k_B T)^{1/2}} \frac{a_0^2}{2} \frac{2\pi D_{NP}^2/4}{\pi D_{NP}^2/4} = k_e \frac{p}{(2\pi M k_B T)^{1/2}} a_0^2 \tag{3.3}$$

The evaporation rate for the quasi-full-sphere catalyst $V_{e,fNP} = V_{e,hNP} 2 \left(\frac{D_{NP}}{D_{NW}}\right)^2$.

To estimate the Cd evaporation rate, we will use the activity of Cd in Au. The gold catalyst will reduce the Cd vapor pressure to $p_{Cd} = a p_{Cd}^0$. The activity was measured in references [53] and [54]. Fig. 3.21 shows the activity of Cd in liquid Au at 1000K given in Table I of ref.[53]. Two regimes are present: at low Cd content, the Au-Cd interaction is dominant and the activity is small, while at high Cd content, the Cd-Cd interaction is dominant and the activity increases. The line is a fit for low activity values with equation $a_{Cd} = 0.014x$, hence for the concentration $x = 0.02$ (derived in section 3.3) we obtain $a_{Cd} = 2 \times 10^{-4}$ at 1000 K. This is an interpolation between 0 and the measured values, hence rather safe.

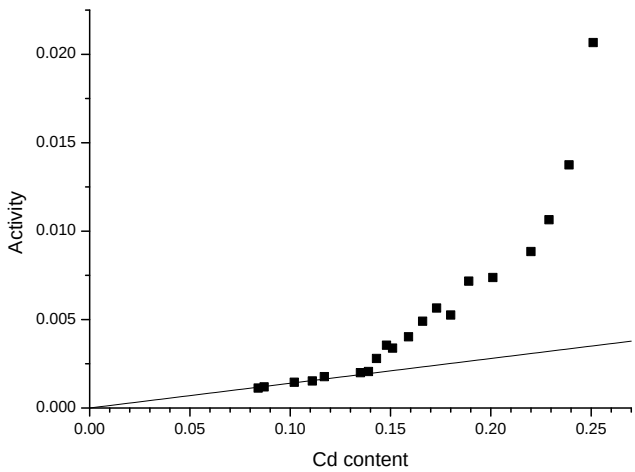

Figure 3.21: Activity of Cd in liquid Au at 1000K given in Table I of ref.[53]. The line is a fit for low activity values, with an interpolation between 0 and the measured values.

Reference [54] considers slightly lower temperatures for solid gold as shown in Fig. 3.22. The graph is qualitatively similar to the previous one, with a very low activity at low Cd content, followed by a rapid increase at rather high Cd content. The ideal line shows the case of non-interacting Au and Cd.

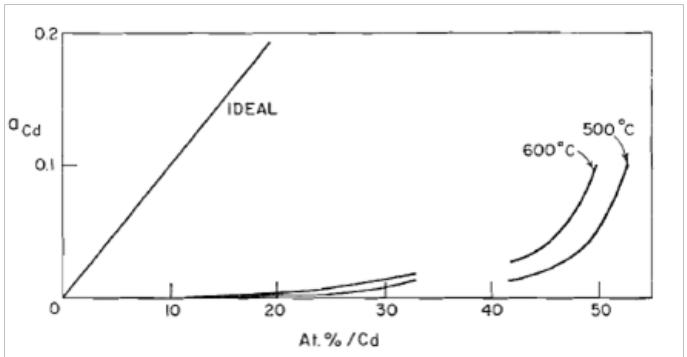

FIG. 7. The activities of cadmium at 500 and 600 °C.

Figure 3.22: Activity of Cd in solid Au at 650K given in ref. [54].

Using Table I of Ref. [54] the value $a_{Cd} = 2 \times 10^{-6}$ at $x = 0.02$ and $T = 650K$ is obtained. This is an extrapolation to our temperature range to be taken with care. Then V_e=1.6 ML/s at 650 K. This is of the same order as the impinging flux.

If one considers the exponential factors in the Cd vapor pressure ($p \sim \exp -\frac{12120}{T}$) and the activity from [54] ($a \sim \exp \frac{\Delta G}{RT}$ with ΔG =-15304 cal/g.atom at 8% of Cd, extrapolating to 17800 at 2% Cd, hence $a \sim \exp -\frac{8900}{T}$), the vapor pressure for Cd in gold is $\sim \exp -\frac{21000}{T}$ and one gets a factor of 3.6 between 350°C and 375°C, hence a strong effect of temperature over the relevant range. The activation energy is $E_{NP} = k_B T_0/q = 1.8$ eV. Hence as a function of temperature and if the concentration remains at 2%, $V_e = 1.6 \exp(-E_{NP}/k_b T) \exp(E_{NP}/k_b T_0)$ in ML/s, with T_0=650K.

The evaporation rate of CdTe is also significant. Fig. 3.23 shows the growth rate of 2D layer of CdTe (100) as a function of temperature [55] using a stoichiometric CdTe flux, compared with a new calibration in rich-Cd conditions. The evaporation rate is shown by open triangles [55], it was measured as 0.027ML/s at 350°C and 0.1ML/s at 375°C.

The low value of the growth rate of the 2D layer is the effect of two contributions, the sublimation of CdTe at a certain temperature indicated by open triangles (it can be measured by RHEED oscillations in the absence of incident flux at a certain temperature, shown in Fig. 3.23) and the desorption of adatoms that are not incorporated in the presence of flux [55], the nucleation efficiency being not unity [56]. In the presence of additional Cd, the desorption is almost suppressed (red squares).

Now Fig. 3.24 shows a complete sketch of all contributions to the NW growth rate considering also re-evaporation for CdTe:

- if we consider re-evaporation from NW sidewalls, the lateral flux probably contributes less than the direct flux to the catalyst and the lateral growth (shell) is

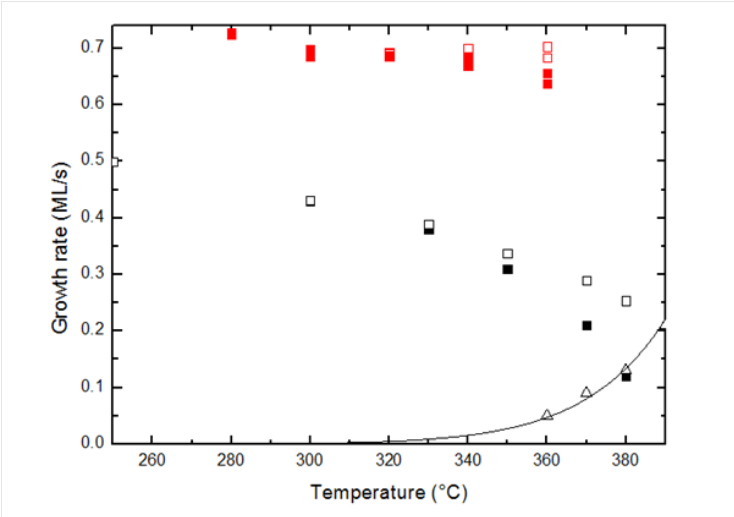

Figure 3.23: Growth and evaporation rates of CdTe measured by RHEED oscillations on CdTe(100) surface, as a function of the substrate temperature. Open triangles indicate the sublimation rate measured by RHEED oscillations in vacuum (absence of flux). Black closed squares indicate the growth rate measured using a stoichiometric CdTe flux (equal to 0.57 ML/s as measured under strong Cd excess at low temperature) from Ref. [55]. Red closed squares are measured in excess of Cd (present work). Closed symbols indicate the sum of growth rate and sublimation rate.

limited;

- the re-evaporation of Cd from the gold catalyst is important in the temperature range of interest, probably the Cd content in the catalyst is limited more by re-evaporation than NW growth;
- by stopping the CdTe flux, the CdTe NW can dissolve in the catalyst and the Cd can evaporate.

In this case the total balance for the NW growth is critical. We can then consider that a small change in temperature will modify the desorption and therefore the growth of the NW.

Experimental data on the growth rate as a function of the temperature can be fitted for ZnTe, by considering a temperature-dependent diffusion length λ; the result is the green curve shown in Fig. 3.25 (activation energy of 0.8 eV). The red line for CdTe, is instead obtained considering two features:

1. The effect of sublimation of CdTe on the sidewalls adatoms: Cd and Te adatoms are present on the sidewalls, resulting from the balance between the incident flux, the sublimation of CdTe, and a transfer to the nanoparticle from the sidewalls over a length equal to the diffusion length (or transfer from the sidewalls to the nanoparticle). The diffusion length is taken to be equal to that of ZnTe.

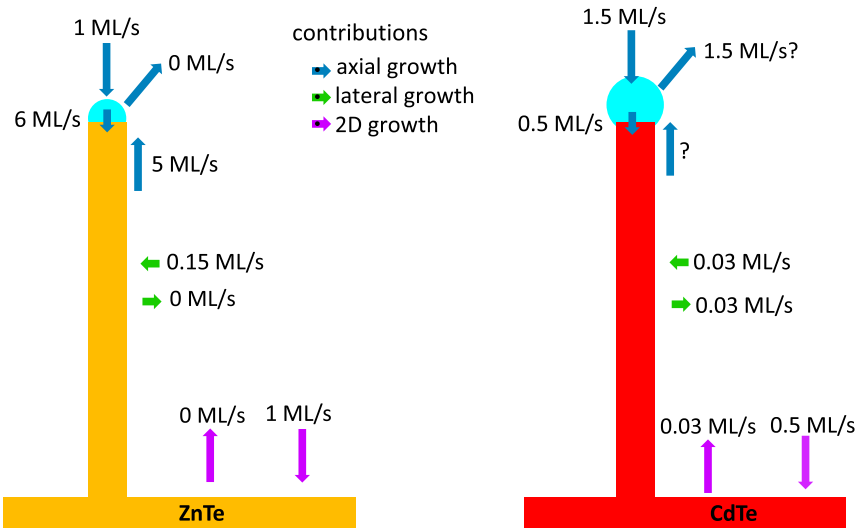

Figure 3.24: Summary of different flux contributions due to geometry of the MBE chamber and re-evaporation for ZnTe and CdTe growth.

2. The effect of Cd evaporation from the Au nanoparticle. Cd atoms are present in the nanoparticle:

   - A range of Cd content exists, where there is no nucleation at the tip of the nanowire (presence of a nucleation barrier); then the Cd content in the nanoparticle is fixed by the balance between three contributions, from the direct flux to the nanoparticle, the evaporation from the nanoparticle, and the transfer from / to the sidewalls.
   - If the temperature decreases, the evaporation slows down so that the Cd content increases and nucleation starts. As the nucleation rates increases very rapidly with the difference in chemical potential (exponential dependence), the growth rate rapidly adjusts to the available flux (balance between the three previous contributions). The red line in Fig. 3.25 is the result of this balance, neglecting any deviation of the Cd content in the nanoparticle from 2%, the value estimated from the interface shape.

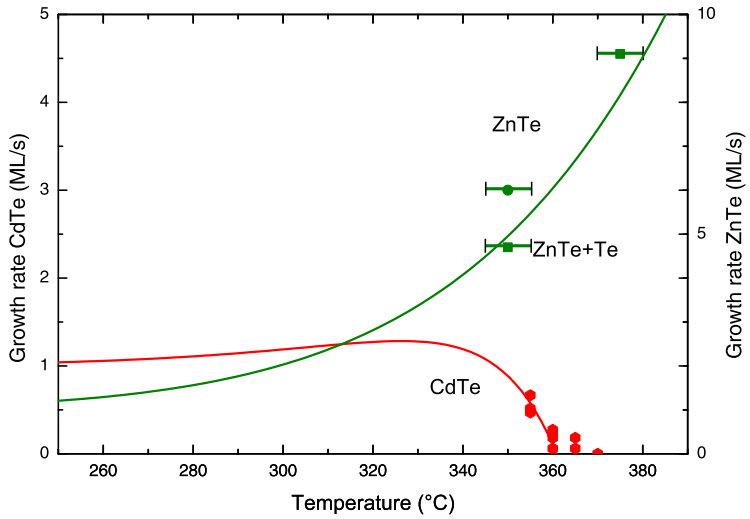

Figure 3.25: Growth rate for CdTe (red dots) with respect to the nominal CdTe growth rate of 0.5ML/s (left vertical axis), and ZnTe in stoichiometric (green dots) and rich-Te (green squares) conditions with respect to the nominal ZnTe growth rate of 1ML/s (right vertical axis).

Comparison with data from literature

To conclude we can compare our results with the literature. In particular in Ref. [43] from Warsaw group is reported the growth of gold catalyzed CdTe NWs with the VLS method. The temperature window in which the growth is possible is between 330 and 350°C. The growth rate of the CdTe NWs is 1500 nm for 40 min, corresponding to 2ML/s for comparison with the growth rates reported here. To compare these data with our results and our model, we have to consider how the fluxes are measured.

The beam equivalent pressure is measured at 1×10^{-6} mbar (or 1.34×10^{-6} Torr) from a Cd cell. The position of the cell is not specified. In our case, the reading is 0.45×10^{-6} Torr for 0.5 ML/s and a CdTe cell. The reading from a Bayard-Alpert gauge [57] is expected to be:

$$I = \alpha Z \sqrt{\frac{M}{T}} J \tag{3.4}$$

where J is the flux of particles of mass M, atomic number Z at temperature T. We have:

	M	Z	°C	K
Cd	112	48	120	390
Te_2	256	104	380	650
CdTe			500	770

Table 3.1

- The Cd flux from a Cd cell:

$$I_{Cd}^{Cd} = \alpha 48\sqrt{\frac{112}{390}} J_{Cd}^{Cd} \tag{3.5}$$

- The Cd flux from a CdTe cell:

$$I_{CdTe}^{Cd} = \alpha\left(48\sqrt{\frac{112}{770}} + \frac{1}{2}104\sqrt{\frac{256}{770}}\right) J_{CdTe}^{Cd} \tag{3.6}$$

Hence the flux from a Cd cell:

$$J_{Cd}^{Cd} = \frac{I_{Cd}^{Cd}}{I_{CdTe}^{Cd}} \frac{48\sqrt{\frac{112}{770}} + \frac{1}{2}104\sqrt{\frac{256}{770}}}{48\sqrt{\frac{112}{390}}} J_{CdTe}^{Cd} = \frac{I_{Cd}^{Cd}}{I_{CdTe}^{Cd}}\left[1 + \frac{1}{2}\frac{104}{48}\sqrt{\frac{256}{112}\frac{390}{770}}\right]0.5 = 2.3\text{ML/s} \tag{3.7}$$

So the range of temperature is similar to our growth conditions, but with a higher flux. The growth rate is larger, ∼2ML/s, suitable for the growth of NWs. In a previous article they have observed very diffused interfaces, greater than 100 nm [58, 59], not adapted to the formation of a QD.

In Ref. [24], they have a beam equivalent pressure between 0.5 and 1×10^{-6} mbar (similar to Ref. [43]). The growth rate at 395°C is up to 0.2 nm/s, which is close to our growth rate at lower temperature.

If we consider the Cd vapor pressure as a function of temperature,

$$\log_{10} p = 7.948 - \frac{5264}{T} \tag{3.8}$$

hence

$$\log_{10}\frac{p_1}{p_2} = -5264\left(\frac{1}{T_1} - \frac{1}{T_2}\right) \simeq -5264\frac{\Delta T}{T_2} \tag{3.9}$$

A factor of 5 in the flux means $\Delta T \simeq \frac{T^2}{5264}\log_{10}\frac{p_1}{p_2}$ =55 K in reasonable agreement with the shift from 350 to 395°C between our conditions and those of Wurzburg group [24].

To conclude, we have shown that:

- there is a good combination of temperature and flux for CdTe QD growth. In these conditions the growth rate is slow and we were able to realize QD with a sharp interface and weak lateral growth.The remaining problem is that a better control of the temperature is needed for sample reproducibility;
- under the same conditions we realize ZnTe NWs embedding CdTe QDs with controlled photoluminescence properties, in particular we minimize (1) the parasitic lateral regrowth (2) the effect of inter-diffusion of Cd to obtain pure CdTe QDs;
- we succeeded in the fabrication of quantum dots with various aspect ratios;
- the growth of long CdTe NWs requires instead an higher flux of CdTe;
- a complete model is missing accounting for a variable Cd content in the nanoparticle, the nucleation rate at the interface between the nanoparticle and the tip of the nanowire, and a proper description of steps and nucleation on the NW sidewalls.

CHAPTER 4

Doping of ZnTe nanowires with nitrogen Plasma

Contents

4.1 Overview **75**

4.2 Doping of ZnTe(100) 2D layers **75**

4.3 Effects of doping on the morphology of ZnTe NWs **77**

4.3.1 Growth of ZnTe:N NWs 77

4.3.2 Effects of the nitrogen plasma on the growth mechanism 79

4.3.3 Growth of core/shell ZnTe/ZnTe:N NWs 83

4.3.4 Photo-luminescence of core/shell ZnTe/ZnMgTe:N NWs 84

4.4 Fabrication of NW-FET **86**

4.5 Characterization of core/shell ZnTe/ZnTe:N NWs **90**

4.5.1 Model of the NW-FET 90

4.5.2 The 4-probe method 91

4.5.3 Resistance along a cone-shaped NW with 4 contacts 93

4.5.4 Growth conditions of ZnTe/ZnTe:N core/shell NWs 95

4.5.5 Measurements on the nominally undoped ZnTe NWs reference sample 95

4.5.6 Measurements on the ZnTe/ZnTe:N NWs with shell growth temperature of 350°C 97

4.5.7 Measurements on the ZnTe/ZnTe:N NWs with shell growth temperature of 290°C 99

4.6 Discussion and conclusion **103**

This Chapter is devoted to the growth by molecular beam epitaxy of nitrogen doped ZnTe NWs. A short introduction is given in section 4.1. Section 4.2 reviews the growth conditions for doping of 2D layers of ZnTe(100), and our Hall measurements on reference samples. Then I present the results of the growth of doped ZnTe:N NWs and

core/shell ZnTe/ZnTe:N NWs in section 4.3, giving complementary information about the photoluminescence properties of these structures. Some information on the fabrication of singe nanowire based field effect transistor (NW-FET) is given in section 4.4. Section 4.5 is devoted to the electrical characterization core/shell ZnTe/ZnTe:N NWs.

4.1 Overview

Doping of II-VI semiconductors by molecular beam epitaxy is challenging, with the exception of ZnTe when doped p-type using nitrogen plasma in the MBE chamber [60]. P-type doping in the diluted magnetic semiconductor (Zn,Mn)Te, obtained adding Mn for magnetic doping, has been demonstrated to induce ferromagnetism [2] due to the strong coupling between the carriers (electrons in the conduction band or holes in the valence band) with the localized magnetic moments of these magnetic impurities.

This chapter deals with the growth of p-type doped ZnTe NWs using N plasma, which is a fundamental step towards the control of the number of carriers in more complex samples embedding a diluted magnetic semiconductor.

The control of doping in semiconductor NWs still represents a challenge, due to growth issues, because the morphology of the NWs can be affected by the presence of dopants [61, 62], but also because quantitative measurement of the NW doping level is still a major challenge, in part due to NW dimensions but also depending on the semiconductor material considered. For instance, due to the different Fermi level pinning at the surface, the realization of ohmic contacts in GaAs NWs [63] is more challenging with respect to InAs NWs [64].

Electrical measurements have historically been the most widely used, but recently many groups have demonstrated quantitative measurements using other techniques, like EDX [30] and atom probe [65, 66]. It is important to distinguish between techniques that measure the dopant concentration (impurities in the crystal matrix) and techniques that measure the carrier concentration. Traditional Hall measurements have recently been demonstrated on InAs NWs with diameter of 250nm, but this technique is still challenging in the case of very small NWs because of lithography limitations in preparing the contacts [67, 68, 69].

The details of the different measurements techniques, are given in section 4.5.1 and 4.5.2 of this Chapter.

4.2 Doping of ZnTe(100) 2D layers

The nitrogen doping of ZnTe (100) 2D layers was first checked with the growth of two calibration samples characterized by Hall measurement.

The calibration samples were grown on $Cd_{0.96}Zn_{0.4}Te(100)$ substrates. The substrate was deoxidized using a bromine solution. The growth rate was calibrated by RHEED oscillations on a ZnTe(100) reference substrate at 0.5 ML/s. On (100) oriented substrates, the growth is more efficient when adding a Zn excess of 0.25ML/s to the stoichiometric flux from the ZnTe solid source effusion cell. After the growth of a buffer layer of 0.5μm, the doped layer of 0.5 μm thickness was grown. The best growth conditions for nitrogen doping of (100) ZnTe layers is obtained with a substrate temperature of 300°C.

For the doping, the nitrogen plasma was set in the chamber with the following parameters: power of the RF generator at 450 W and a nitrogen flux of 0.07 sccm adjusted with the mass flow, after the activation of the plasma as explained in section 1.2.2. The doping conditions result in a pressure in the chamber of 2.5×10^{-6} Torr. The same doping conditions will be used for the growth on ZnTe NWs as explained in the next section of this chapter.

The doping level of the reference sample was determined by Hall measurement using the Van der Pauw method. The Van der Pauw method can be applied to two-dimensional (much thinner than wide) samples of arbitrary shape. There are some requirements to satisfy [70]:

1. The sample must be homogeneous and isotropic, and of uniform thickness;
2. The surface of the sample must be singly connected, i.e. the sample must not have any hole;
3. Four ohmic contacts must be located at the corners of the sample as in Fig. 4.1;
4. The contacts must be sufficiently small, the area of contact being at least one order of magnitude smaller than the area of the entire sample.

To fabricate the 4 contacts, the sample was loaded in the UHV metal evaporator and after a treatment with Ar plasma to remove the oxide from the surface, 4 gold contact were realized, by the help of a molybdenum physical mask with 4 holes. The sample size is 5×5 mm, and the contact size is 1 mm.

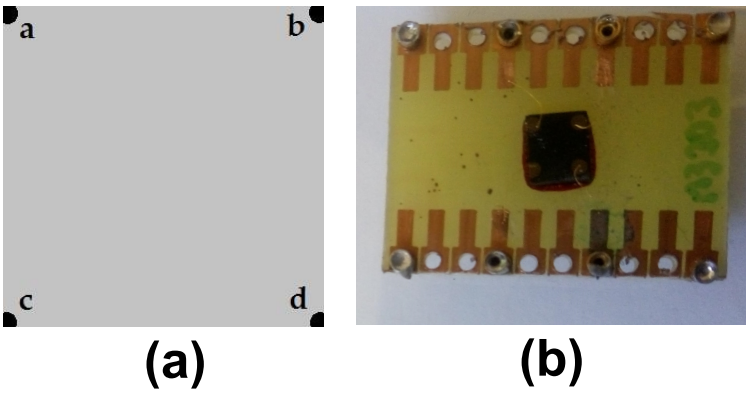

Figure 4.1: (a) sketch of the ideal sample geometry for the van der Pauw method; (b) picture of a ZnTe (100)calibration sample prepared for Hall measurements with 4 gold contacts. The sample size is 5×5 mm.

The setup used for the Hall measurements comprises a current generator, a multimeter and a cryostat equipped with an electromagnet to generate the magnetic field.

The following six measurements are made:

$V_1 = V_{ba}$ with I_{dc}

$V_2 = V_{ca}$ with I_{db}

$V_3 = V_{dc}$ with I_{ba}
$V_4 = V_{db}$ with I_{ca}
$V_5 = V_{da}$ with I_{bc} in the magnetic field +B
$V_6 = V_{da}$ with I_{bc} in the magnetic field -B

These measures are used to calculate the values of different resistances from which the following properties of the material can be obtained: the resistivity, the doping type, the 2D carrier density an the mobility of the majority carriers.

The calibration shows a p-type doping level of p=1.2 $\times 10^{19}$ holes/cm^3 and a mobility of 30 cm^2/Vs. This doping level is slightly lower than the record achieved in the group of 10^{20} holes/cm^3 range, for which transport measurements at 100 mK were realized [2], but still higher than the Mott critical density of 0.8 $\times$ 10^{19} holes/cm^3.

4.3 Effects of doping on the morphology of ZnTe NWs

The best conditions for p-type doping of a ZnTe(100) layer are markedly different from our growth conditions of NWs 2.1.3. Nevertheless, good p-type doped layers can be grown at 300°C[71] which is close to the NW standard growth temperature.

However doping is known to potentially impact the NW morphology. So far in the literature it has not been reported about the growth by molecular beam epitaxy of doped ZnTe NWs using N plasma. In the next section I will report the results of the growth of ZnTe NWs using N plasma under different growth conditions.

In the ideal case, for the ZnTe NW electrical characterization we would like to realize 4 probe measures. By electron-beam-lithography we would like to realize metal contacts with a width of 200 nm and spacing as high as possible depending on the NW length. Considering a minimum spacing between 250 and 300 nm, the minimum length required for the NWs is in the range of 1.5 - 1.7 μm. The NW diameter also has to be below 100 nm at the base to ensure the absence of breaks in the metal at the metal-NW interface.

4.3.1 Growth of ZnTe:N NWs

The first step was to test the growth of doped NWs by direct doping, using for the N plasma the same conditions as for the 2D reference sample, and for the NW growth a stoichiometric ZnTe flux of 0.5ML/s (as calibrated by RHEED oscillation on ZnTe(100)), growth temperature of 350°C and dewetting of gold under vacuum at 350°C.

The result of this growth is shown in the SEM images of Fig. 4.2. In the low magnification image we can observe the presence of few objects, that with higher magnification reveal to be badly formed NWs. The growth with direct doping is clearly affected. For comparison, see Fig. 2.14 (a) where two SEM images of NW grown for 40 min at 0.5ML/s are shown.

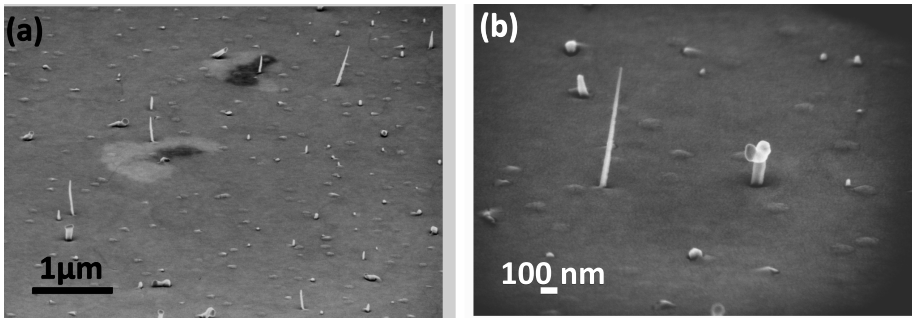

Figure 4.2: (a) low magnification and (b) high magnification 65° SEM image of NWs grown in standard conditions for 40 minutes (dewetting of gold under vacuum and substrate temperature of 350°C) in presence of N plasma (RF generator at 450 W and N_2 flux of 0.07 sccm).

The nitrogen plasma dramatically decreases the number of NWs and impacts the morphology of the few NWs that are present.

The second step was to start the sample growth in standard conditions (dewetting of gold under vacuum and substrate temperature of 350°C) for a short time of 7 minutes in order to not perturb the beginning of the growth which is a quite complicated step as explained in Chapter 2. After 7 minutes the growth was continued during 15 minutes for one sample and during 1 hour for the other, in presence of N plasma. For these samples, at the beginning of the growth, the pressure in the growth chamber was 5×10^{-8} Torr, two orders of magnitude higher than usual, even when the nitrogen flux was stopped. In fact it takes at least 12 hours to recover the usual background pressure 10^{-10} Torr.

As it can be observed in Fig. 4.3, we did not obtain NWs with a good morphology even after 1 hour of growth and with probably a lot of structural defects. This growth time was chosen in order to get sufficiently long NWs for contact fabrication and electrical characterization. Other samples were also prepared exploring different stoichiometry and growth temperatures, but the morphology was not good (not shown). In conclusion this two step growth method generates a reasonable density of NWs but it confirms that the morphology is strongly altered. It suggests that the axial growth of the ZnTe NWs is strongly reduced or interrupted by the presence of N in the growth chamber. The doping conditions result in a pressure in the chamber of 2.5 x 10^{-6} Torr, four orders of magnitude higher than the background pressure in the chamber.

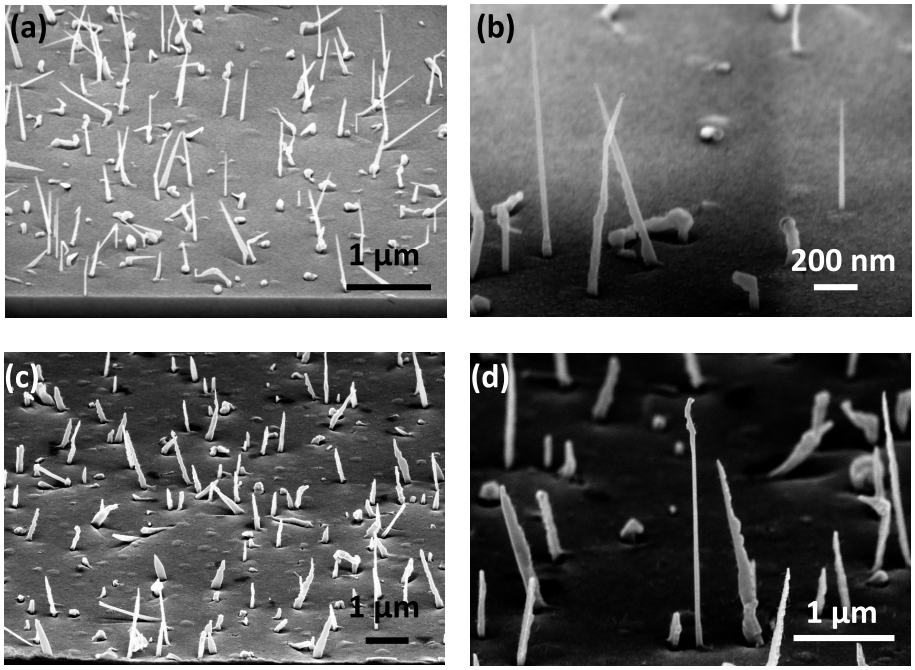

Figure 4.3: (a) and (c) low magnification and (b) and (d) high magnification SEM image of ZnTe NWs grown in the beginning for 7 minutes in standard conditions (dewetting of gold under vacuum and substrate temperature of 350°C) and after this time in presence of N plasma (RF generator at 450 W and N_2 flux of 0.07 sccm) (a) and (b) during 15 minutes and (c) and (d) during 1 hour.

4.3.2 Effects of the nitrogen plasma on the growth mechanism

The third series was prepared to investigate the effects of the N plasma on the growth. Fig. 4.4 is a sketch of the growth recipe for the samples of the series. All the 4 samples were prepared in the same way, the first part of the growth was done in standard conditions (during 10, 20 and 30 minutes in UHV) and the second part in presence of N plasma (during 30, 20 and 10 minutes, with a chamber pressure due to nitrogen of 2×10^{-6}Torr) in order to keep the same total growth time of 40 minutes. After gold dewetting for 5 minutes at 350°C under Zn flux of 0.4 ML/s, the growth of ZnTe was immediately started, then growth was stopped, the temperature lowered and the sample was stored into the transfer modulus for some hours (in the mean time the first part of the growth of the others three samples was done). After the interruption the reference sample was introduced back in the chamber, the temperature raised to the growth temperature of 350°C and the second part of the growth of 20 minutes was completed in the same standard conditions as before. After this, the same was done for the other three samples of the series, but in presence of the nitrogen plasma, during 30, 20 and 10 minutes to complete the 40 minutes of growth. A reference sample was also grown during 40 minutes in standard conditions of UHV without growth interruption. SEM images of this reference sample are shown in Fig.s 2.13 and 2.14.

SEM images of the other samples are shown in Fig. 4.6. We will refer to each sample

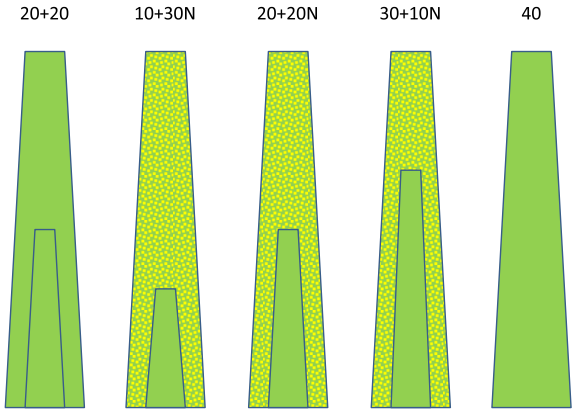

Figure 4.4: scheme of the growth recipe used for series 3. The total growth time for each sample is 40 minutes but the nitrogen doped growth time is changed from 0 to 10, 20 and 30 minutes.

using the names 10+30N and so on. The reference sample 20+20 shows a uniform morphology from SEM images 4.6(a) and (b). The growth interruption does not seem to alter the growth. Increasing the time of the doped part, instead we observe a difference in diameter and length of the cylinder-shaped NWs. In sample 10+30N the gold catalyst cannot be observed on top of the NWs as shown in Fig. 4.5.

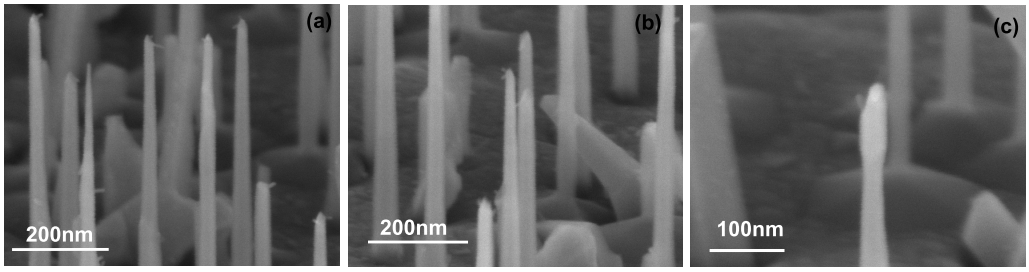

Figure 4.5: (a)-(c) SEM images of ZnTe/ZnTe:N NWs with growth time 10+30N. On top of the NWs the Au nanoparticles are not visible.

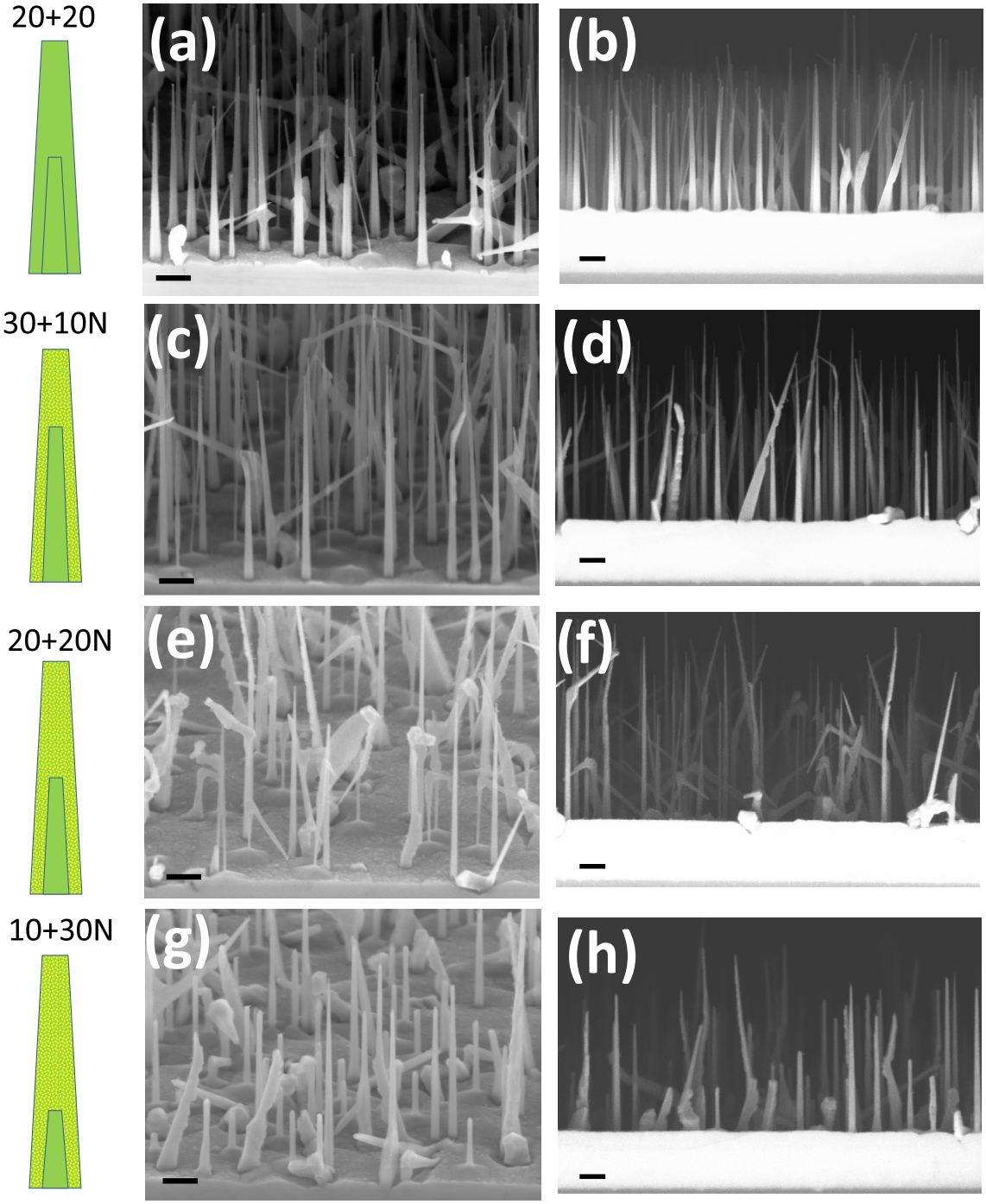

Figure 4.6: (a), (c), (e) and (g) 65° and (b), (d), (f) and (h) 90° SEM images of the samples of series 3, with a ZnTe/ZnTe:N growth recipe. The growth times are indicated in the sketch on the left. The scale bar is 200 nm for all images.

The morphology difference in this series can be estimated by a statistical analysis of the length and base diameter, shown in Fig. 4.7. The final NW length is smaller for the sample grown for 10+30N minutes and the diameter of the NWs increases. For the cone-shaped NWs (ZB) base diameter, this effect is less evident, even if the gold nanoparticle is no more observed on top of the NWs after the 30 min time of the doped growth, see Fig. 4.5. In fact for cone-shaped NWs the base diameter depends on the total growth time. The length dispersion of Fig. 4.7 (a) is of the same order as the statistics of the 40 min sample of chapter 3, shown in Fig. 2.13 (b). .

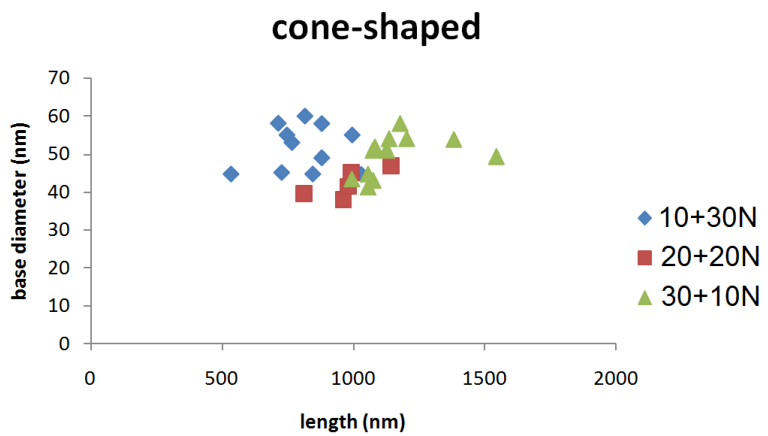

(a)

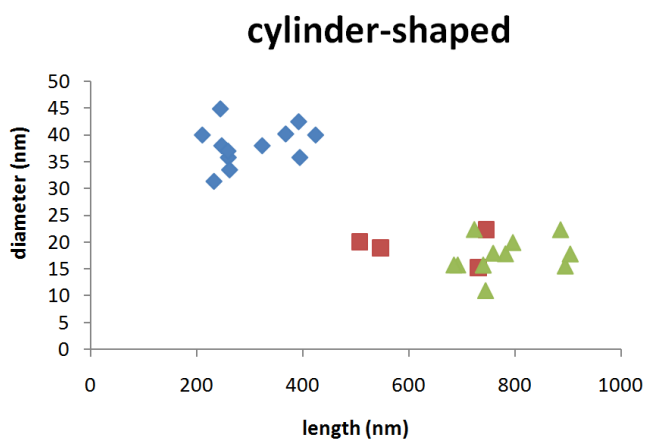

(b)

Figure 4.7: Statistical analysis of the length and base diameter of cone-shaped (a) and cylinder-shaped (b) NWs of samples of series 3.

Usually for the cylinder-shaped NWs , the NW diameter is equal to the gold catalyst diameter (no lateral growth is observed, like in Fig. 2.3 and 2.13, and in general the growth of a shell is very difficult). Instead in Fig. 4.7 (b) we clearly see an increase of the diameter up to 45 nm, while keeping a cylinder shape.

For each sample of the series with doped shell growth time of 10, 20 and 30 min and

the two reference samples grown for 40 min and 20+20 minutes, the average value of (a) the length and (b) the diameter as a function of the shell growth time (black points) are shown in the two graphs of Fig. 4.8. The black curves are obtained by integration of the expected growth rate function (axial or radial) defined as a constant without the presence of the nitrogen plasma, assuming then an exponential decrease (increase) when the doping is started, until an equilibrium regime is reached where it is again constant. The analytical expression is calculated by integration of the expected growth rate equation, and as parameter of the fitting of the experimental data it is possible to obtain: the value of the growth rate in the two regimes where it is constant and the transition time τ to pass from a regime to the other.

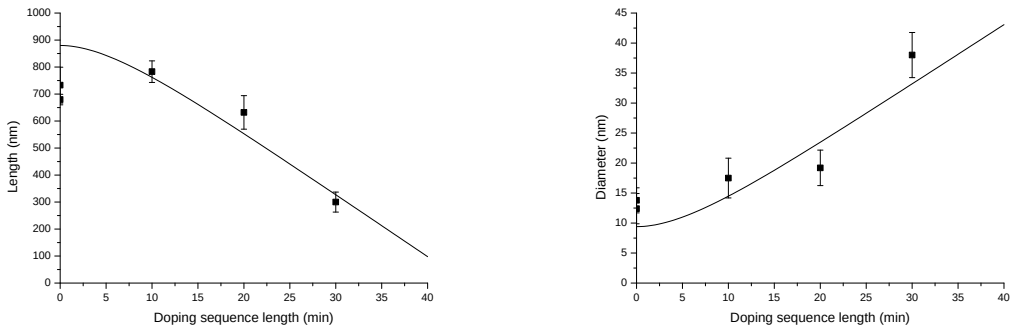

(a) **(b)**

Figure 4.8: Experimental points (black squares) are obtained from the statistical analysis of SEM images of Fig. 4.7 for the cylinder-shaped NWs, and represent (a) the average length and (b) the average diameter for each sample of the series as a function of the doped growth time. The error bars are given by the standard deviations. Black curves are obtained (as explained in the text) with values of the initial growth rate of (a) 22 nm/min and (b) 0.01 nm/min, final (a) 0.0 nm/min and (b) 1 nm/s and tau= 6 min.

In summary the presence of the nitrogen plasma in the growth chamber perturbs the growth. For ZB cone-shaped NWs the axial growth is strongly reduced with the increasing doping growth time. The radial growth does not seem affected. For the WZ cylinder-shaped NWs, the axial growth is strongly reduced but the radial growth is enhanced by the presence of the nitrogen plasma.

4.3.3 Growth of core/shell ZnTe/ZnTe:N NWs

To obtain NWs with length of about 2μm for the transport measurements, we decided to use the core-shell geometry, taking advantage that the radial growth is not affected during doping.

In Fig. 4.9 we show SEM images of the two samples of series 4, grown with an interruption between the undoped ZnTe part (in this series 1 hour) an the doped ZnTe:N part (in this series 30 minutes) like in series 3. The difference between the two samples

shown in Fig. 4.9, is the growth temperature of the undoped part (a) 350 and (b) 375°C. The doped part in both cases was grown at 350 °C.

For the sample with structure ZnTe(350)/ZnTe:N(350), the final length of the cone-shaped NWs is in the range 1 - 1.5 μm, while the base diameter is in average 170nm. While for the one with structure ZnTe(375)/ZnTe:N(350), the tapering angle is reduced in agreement with previous results, the NW final length is in the range 1.5 - 2 μm, while the base diameter is in average 100 nm.

Since the NWs are short and we are interested in realizing metal layers 200 nm wide on top of the NW, for geometrical reasons of the electron-beam lithography method this limits the maximum height of the metal pads to 160nm. So in this case, to avoid a possible break in the metal contact at the NW edge, the base diameter dimension of the NWs must be taken into account and should not be bigger than 100 nm.

As it can be observed from SEM images, the optimal morphology for the realization of contacts is obtained with the growth of the core at 375°C. This growth recipe will be used for the growth of the NWs for electrical characterization as explained in section 4.5.4.

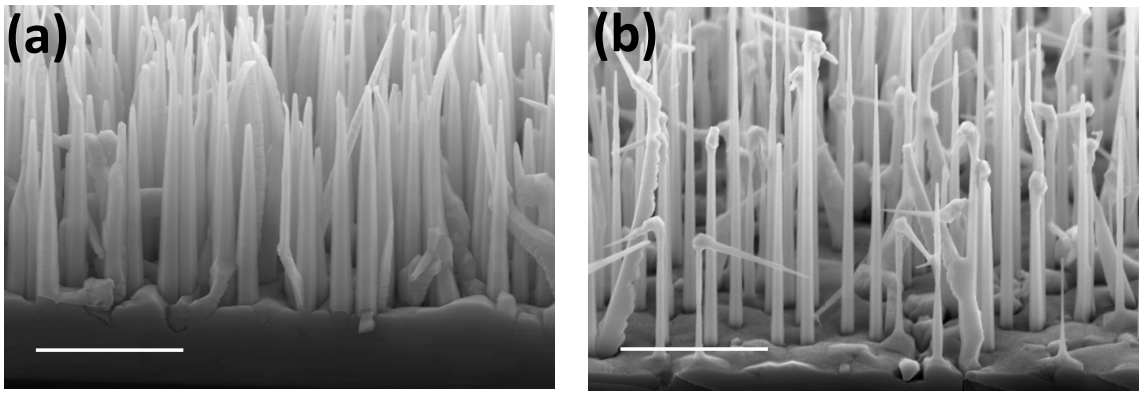

Figure 4.9: SEM images of two sample, grown with an interruption between the undoped ZnTe part (1 hour) an the ZnTe:N part (30 minutes), with parameters for nitrogen plasma: RF generator at 450 W and N_2 flux of 0.07 sccm. The growth temperature of the undoped part was (a) 350°C and (b) 375°C, and for the doped part it was 350°C. The scale bar is 1μm.

4.3.4 Photo-luminescence of core/shell ZnTe/ZnMgTe:N NWs

Sample M3265 was grown at 350°C with a ZnTe core (40 minutes) and a ZnMgTe shell (10 minutes) doped with nitrogen (usual conditions for the plasma), with ZnTe flux of 1ML/s as calibrated by RHEED oscillations on a ZnTe(100) reference sample, and a nominal Mg content of 10%. The luminescence of the sample was studied by Alberto Artioli during his PhD using the cathodoluminecence (CL) setup at Néel Institute. The CL signal (photon emission from a sample under electron beam excitation) is

collected with an off-axis aluminum parabolic mirror, focused onto the entrance slit of a spectrometer via an achromatic optical system using aluminum mirrors, and recorded as a function of the position (CL images) or of the emission wavelengths (spectra). The sample is placed on a cold finger at approximately 10K.

The two graphs in Fig.s 4.10 (a) and 4.11 (a) show the CL spectra from the NWs of sample M3265. The spectra are acquired from the e-beam excited area of the SEM image in the inset. The images in panels (c) are monochromatic CL mapping at the emission of the main peak form the CL spectra, identifying the spatial region from which the photons of the main peak of the CL spectra are emitted. It is mostly the base of the NWs.

In the CL spectra of panels Fig.s 4.10 (a) and 4.11 (a) the position of the main detected peak is blue shifted with respect to the free exciton in bulk ZnTe. In bulk ZnTe the free exciton is found at 2381 meV, while for ZnTe NWs is was found at 2383.7 meV[9]. In the presence of a passivation shell of ZnMgTe, the exciton energy of ZnTe is red shifted to 2350meV due to strain[9, 72]. The luminescence expected from the ZnMgTe shell with a 10% of Mg is indicated in the two graphs in Fig.s 4.10 (a) and 4.11 (a), with a greater blue shift with respect to our peak. two interpretations can explain the position of this peak: (1) the photoluminescence from a ZnMgTe shell with Mg content below 3% and (2) a bound-to-bound transition (D^0, A^0) in the ZnMgTe:N shell [60], with a red shift of 60 mV with respect to the exciton of $Zn_{0.90}Mg_{0.10}Te$.

Confirmation for our hypothesis would require a study as a function of the nominal Mg content in the ZnMgTe:N shell or of the doping level in the ZnMgTe:N shell. This goes beyond the aim of the present work.

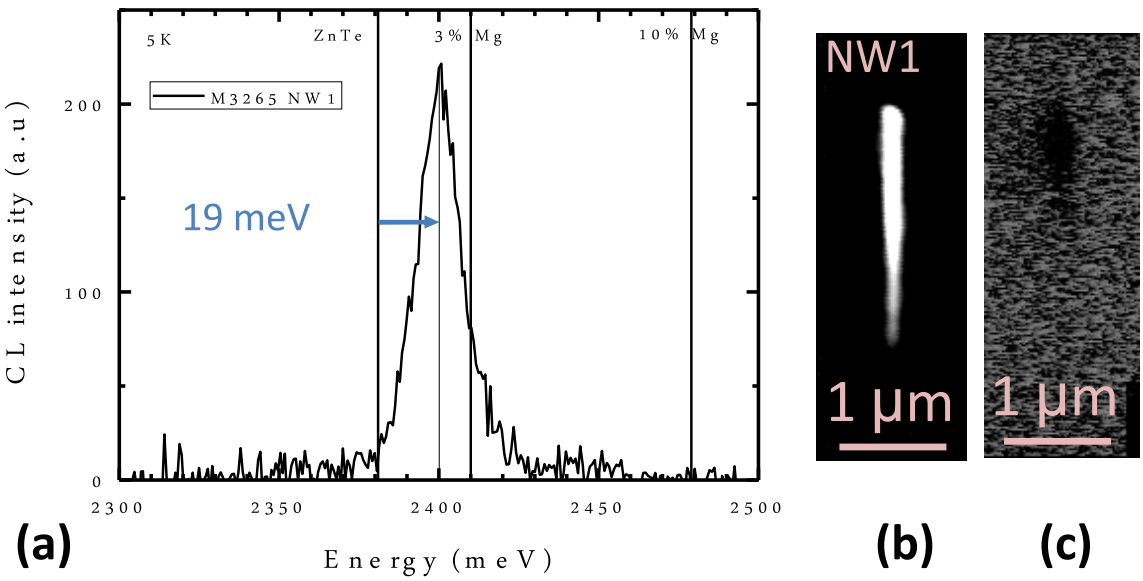

Figure 4.10: (a) CL spectra from a ZnTe/ZnMgTe:N NW of sample M3265, (b) SEM image and (c) CL mapping of the measured NW. In (a) from left to right, the energy of bulk ZnTe, bulk $Zn_{0.97}Mg_{0.03}Te$ and bulk $Zn_{0.90}Mg_{0.10}Te$ are indicated.

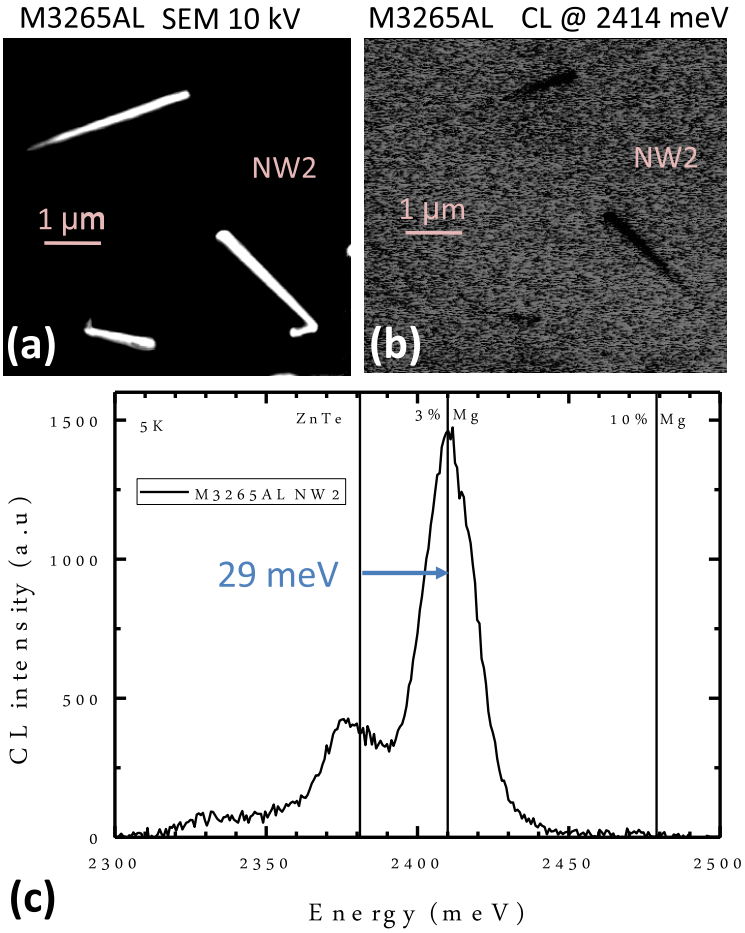

Figure 4.11: (a) CL spectra from ZnTe/ZnMgTe:N NWs of sample M3265, (b) SEM image and (c) CL mapping of the measured NWs. In (a) from left to right, the energy of bulk ZnTe, bulk $Zn_{0.97}Mg_{0.03}Te$ and bulk $Zn_{0.90}Mg_{0.10}Te$ are indicated.

4.4 Fabrication of NW-FET

For the fabrication of NW-FET, different chips were first prepared on a commercial 2 inch Si wafer doped p-type with on top a layer of 300 nm of SiO_2. The chip design of Fig. 4.13 is the motif repeated on the wafer, and it was patterned by laser lithography at Nanofab with the help of Thierry Crozes. After development, the resist residuals were cleaned by RIE (reactive ion etching) using O_2 plasma for 20 seconds. Then a multilayer of Ti(10 nm)/Au(70nm) was deposited by thermal evaporation. After lift-off, the wafer was cut to obtain the separated chips. The NWs were then mechanically transferred to the pre-patterned chip and localized at low magnification SEM, as shown in Fig. 4.12.

In Fig. 4.13 the design of the chip is shown. In the inner part there are 64 metal pads for NW connection, and in the outer part there are marks for manual alignment during electron beam lithography. In particular, the SEM is equipped with an interferometric stage, so once the manual alignment and calibration is done, all the positions on the inner part of the chip can be reached by an automatic routine by translation.

On the outer part, the crosses are used to calibrate the chip angle (rough alignment),

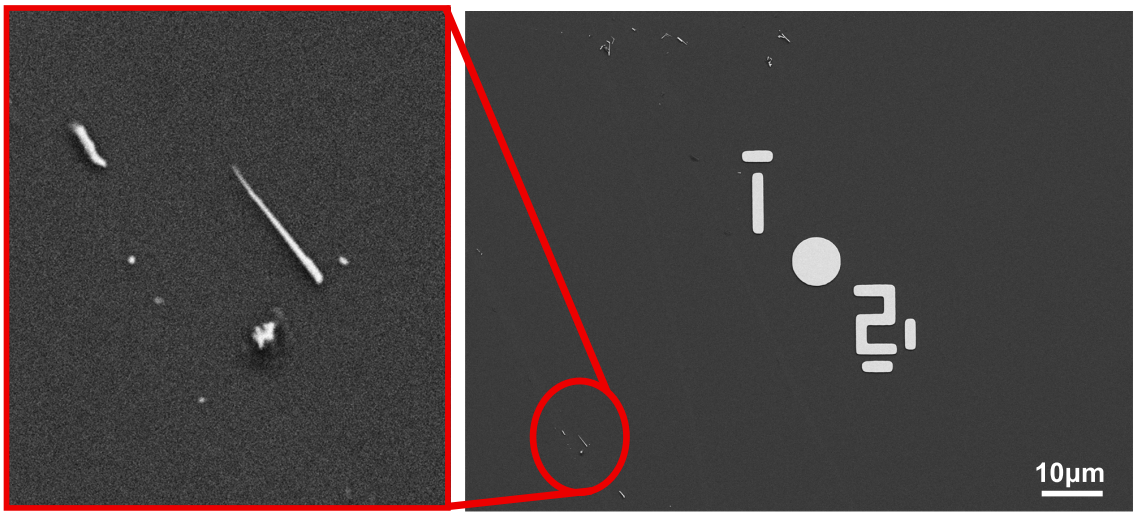

Figure 4.12: SEM image of a chip after the mechanical transfer of the ZnTe NWs. An image with higher magnification of the NW in the bottom-left part is shown as an example.

while on the bottom and on the left there are fine alignment patterns for the two SEM apertures needed for the exposure of the NW design. Once the chip is aligned, the chip patterning can start automatically.

In the inner part where the NWs are deposited, there are 9 big marks (in a 3 by 3 matrix) and a matrix of 16 by 16 small marks, all numbered by unique matrix reference to identify the position of the NW on the chip.

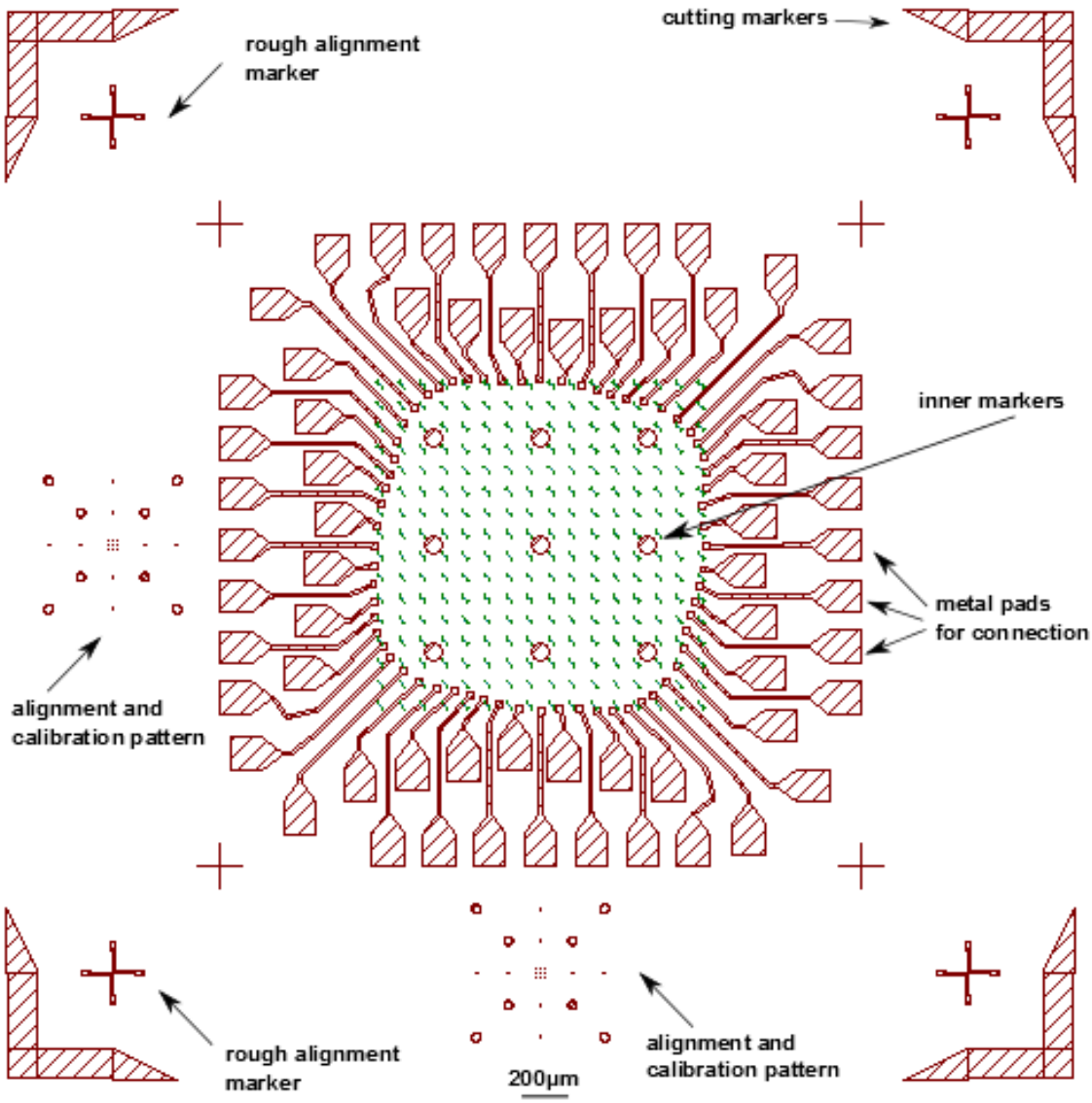

Figure 4.13: Chip design for the NW-FET fabrication.

The Elphy software was used to prepare the design for the electron beam lithography exposure pattern. For each NW the connection with the external pads (pre-patterned on the chip) are done in two steps (the design for each step is identified by a different layer): the smaller features (down to 200 nm) close to the NW are exposed with the 7.5 μm aperture of the SEM microscope, with a pitch of 28 nm, while bigger features are exposed with the 30 μm aperture and 150 nm pitch. The automatic routine uses the big mark closest to the NW position for the fine alignment and the exposure of the bigger features connecting up to the external pads, then it uses the small mark closest to the NW for the small features. In the design there are 4 contacts of 200 nm width on each NW. Each contact on the NW is connected with two pads of the chip to check electrical continuity or if a metal contact is interrupted.

After exposure and development, the resist residues are cleaned by RIE for 20 sec-

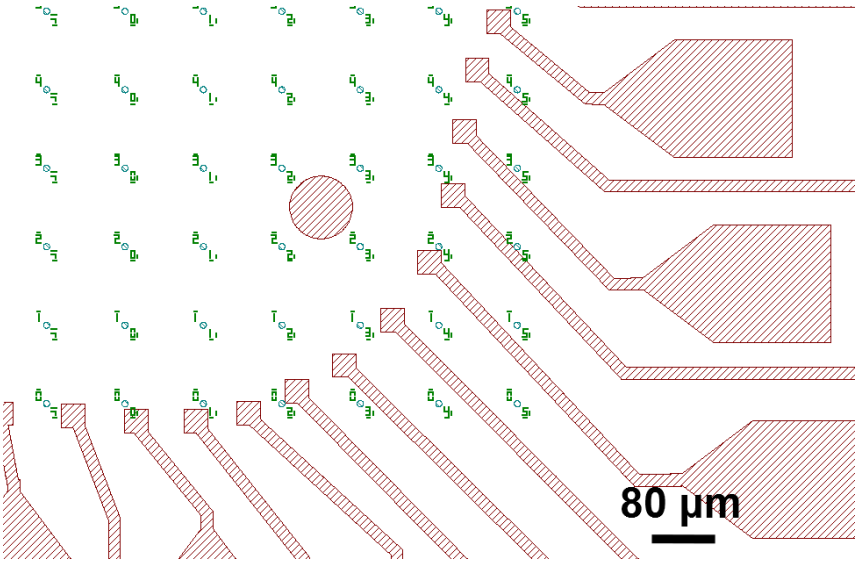

Figure 4.14: Chip design for the NW-FET fabrication. Higher magnification image showing the two kinds of inner markers, big and small.

onds of O_2 plasma. Then the sample is transferred into the UHV metal evaporator for gold deposition in the II-VI MBE facility. To remove the oxide layer from the NW surface, the sample is etched with Ar plasma before the gold deposition of 160 nm, as monitored using the in-situ thickness monitor. Gold was chosen because it is found to form ohmic contacts in doped ZnTe 2D layers [60].

After lift-off, the result is checked at optical microscope. The picture shows a SEM image of NW-FET based on single ZnTe NW.

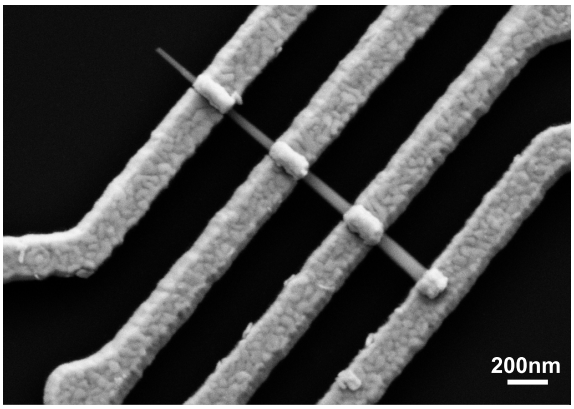

Figure 4.15: SEM image of a NW-FET based on a single core/shell ZnTe/ZnTe:N NW realized by electron beam lithography. The metal contacts are made of 160 nm of gold.

4.5 Characterization of core/shell ZnTe/ZnTe:N NWs

4.5.1 Model of the NW-FET

For the characterization of a FET, one usually measures the characteristic curves of the device: to measure the I_{SD}-V_{SD} curves, the current flowing from source to drain I_{SD} is measured while a voltage V_{SD} is applied between the source and drain keeping constant the voltage applied to the gate V_G (otherwise the drain source voltage is measured V_{SD} when a current I_{SD} is sourced between the drain and source contacts).

The other characteristic curve I_{SD}-V_G is obtained keeping constant V_{SD} while I_{SD} is measured as a function of V_G. From the analysis of the characteristic curves, using a model it is possible to deduce the majority carrier density and the mobility of the NW constituting the NW-FET.

Usually the NW-FET is modeled on the base of the MOSFET equations, even if there are many differences between the two devices. In a NW-FET the source and drain contacts are made of metal electrodes while in the MOSFET case are made of degenerately doped semiconductor [73]. Another difference is that generally the nanowire is uniformly doped along the axis, while in MOSFET the doping profile is varied along the channel in order to improve device performance. A uniform doping level of the nanowire will be assumed in this discussion. The following treatment is the widely most used in the literature to obtain the quantities of interest. It was first applied to the case of carbon nanotube field effect transistor (CNT-FET) [74] and we apply it to the ZnTe/ZnTe:N core/shell structures.

If a homogeneous doping level is assumed, the total charge Q in the NW is:

$$Q = CV_{th} \tag{4.1}$$

where V_{th} is the threshold voltage, i.e. the voltage to completely deplete the NW. It can be measured from the I_{SD}-V_G curves. To calculate the gate capacitance C, usually the *metallic cylinder on an infinite metal plate model* is used. This approximation is reasonable [75] if the charge density in the NW is so high that the semiconductor NW can be treated as a metal cylinder. According to this model the capacitance per unit length in the back gate geometry is:

$$\frac{C}{L} = \frac{2\pi\epsilon\epsilon_0}{\cosh^{-1}(h/r)} \tag{4.2}$$

with r and L being the NW radius and the effective length of the channel, h the distance between the gate electrode and (if one approximate the NW with a cylinder) the center of the NW and ϵ the dielectric constant of the insulating material ($\epsilon = 3.9$ for SiO_2). Usually h is approximated with the thickness of the oxide. In this model the metal cylinder is embedded all around with the insulating material. In Ref. [75] are reported the correction to ϵ that one has to consider for non-embedded NWs and with cross section different from the cylindrical one.

Eq. 4.2 can be further simplified if the quantity $x = h/r \gg 1$, because $\cosh^{-1}(x) = \ln(x + \sqrt{x^2 - 1}) \approx \ln 2x$:

$$\frac{C}{L} = \frac{2\pi\epsilon\epsilon_0}{\ln(2h/r)} \tag{4.3}$$

for $x \geq 6$ this approximation yields an error of 1%. In our case h=300 nm and r≃50, so we will not use this approximation. From the total charge Q, the one-dimensional carrier density can be evaluated as $n = Q/eL$.

In one-dimensional systems, such as NWs or CNT, two transport regime may be possible: ballistic or diffusive. If the carrier diffusion length is higher than the length of the channel, the transport is ballistic, if it is lower it is diffusive. Assuming a diffusive transport at room T, the mobility μ can be estimated from the transconductance of the FET in the linear regime, given by:

$$\frac{dI}{dV_G} = \mu(C/L^2)V_{SD} \tag{4.4}$$

4.5.2 The 4-probe method

The resistivity of the nanowires can be measured using a 4-probe technique[76], where the current I_{14} is sourced between the two end contacts, and the voltage drop between the two middle contacts V_{23} is measured. To avoid large measurement errors, the input impedance of the voltmeter must be much greater than the resistance of the nanowire, which can be achieved using a commercially available test equipment.

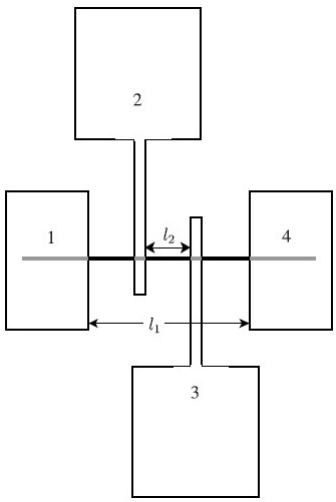

Figure 4.16: Four point test structure for the determination of the resistivity of NWs. The current is sourced between contacts 1 and 2, and the voltage is measured between contacts 2 and 3.

The resistivity of a cylindrical nanowire is then given by:

$$\rho = \frac{V_{23}}{I_{14}} \frac{\pi r^2}{l_2} \tag{4.5}$$

Then we can measure R_T between the two end contacts and determine the contact resistance R_c using:

$$R_T = 2R_c + \frac{\rho}{\pi r^2} l_1 \tag{4.6}$$

We assume in this analysis that the potential drop along the length of the nanowire is not altered by the presence of the two middle contacts. To avoid large measurement errors it is also necessary for the two middle contacts to be short with respect to the transmission length $L_T = \sqrt{\frac{r\rho_c}{2\rho_s}}$, with ρ_c equal to the contact resistivity and ρ_s the semiconductor resistivity. Otherwise a significant portion of the current may be transported through the middle contacts rather than the nanowire, making inaccurate the use of l_1 as length of the semiconductor NW [76].

The expected behavior of a cylindrical structure is a linear increase of the resistance with separation, determined by equation (4.7):

$$R = \frac{\rho L}{A}, \tag{4.7}$$

where L is the length of the wire measured (distance between the inner contacts), A is the cross-sectional area (constant for a uniform cylinder) and ρ is the electrical resistivity of the material.

However, for the cone-shaped nanowires, the variation of the resistance with length should be more complex as the cross-sectional area $A(L)$ varies as a function of length L. The resistance is now determined by equation (4.8):

$$R_{NW} = \int_0^{L_{NW}} \frac{\rho}{A(L)} \, dL, \tag{4.8}$$

where $A(L) = \pi r^2(L)$ and

$$r(L) = r_B - L\tan(\alpha) = r_B - L\frac{r_B - r_T}{L_{NW}} \tag{4.9}$$

r_B and r_T are bottom and top radius respectively, and α is the tapering angle, so that

$$R_{NW} = \frac{\rho}{\pi}\frac{L_{NW}}{r_B r_T} \tag{4.10}$$

If we now consider only a doped shell for a cone-shaped NW, then the section area is:

$$A(L) = \pi(r_o^2(L) - r_i^2(L)) \tag{4.11}$$

where the subscripts $_i$ and $_o$ indicates the core (inner) and outer radius of the cone respectively. Using equations 4.8 and 4.11, the NW resistance will be:

$$R_{NW} = \frac{\rho}{\pi}\int_0^{L_{NW}} \frac{1}{r_o^2(L) - r_i^2(L)} \, dL, \tag{4.12}$$

$$R_{NW} = \frac{\rho}{\pi}\int_0^{L_{NW}} \frac{1}{r_o(L)-r_i(L)}\frac{1}{r_o(L)+r_i(L)}\,dL, \tag{4.13}$$

$$R_{NW} = \frac{\rho}{\pi}\frac{1}{r_o(0)-r_i(0)}\frac{1}{r_o(0)+r_i(0)}\int_0^{L_{NW}} \frac{1}{1+\sigma L}\frac{1}{1+\delta L}\,dL, \tag{4.14}$$

with

$$\delta = \frac{[r_o(L)-r_i(L)]-[r_o(0)-r_i(0)]}{r_o(0)-r_i(0)}\frac{1}{L_{NW}} \tag{4.15}$$

and

$$\sigma = \frac{[r_o(L)+r_i(L)]-[r_o(0)+r_i(0)]}{r_o(0)+r_i(0)}\frac{1}{L_{NW}} \tag{4.16}$$

$$R_{NW} = \frac{\rho}{\pi}\frac{1}{r_o(0)-r_i(0)}\frac{1}{r_o(0)+r_i(0)}\frac{1}{\sigma-\delta}\int_0^{L_{NW}} \left[\frac{\sigma}{1+\sigma L}-\frac{\delta}{1+\delta L}\right]dL, \tag{4.17}$$

which can be integrated as:

$$R_{NW} = \frac{\rho}{\pi}\frac{1}{r_o(0)-r_i(0)}\frac{1}{r_o(0)+r_i(0)}\frac{1}{\sigma-\delta}\ln\frac{1+\sigma L_{NW}}{1+\delta L_{NW}}) \tag{4.18}$$

- if the shell has uniform thickness, then $\delta = 0$;
- If δL_{NW} and $\sigma L_{NW} \ll 1$,

$$\ln\frac{1+\sigma L_{NW}}{1+\delta L_{NW}} = (\sigma-\delta)L_{NW} \tag{4.19}$$

  then $R_{NW} = \frac{L_{NW}\rho}{A}$, with $A = \pi(r_o^2 - r_i^2)$

- in the limit of a uniform doping (no core)

$$\lim_{\sigma\to\delta}\frac{\ln(1+\sigma L_{NW})-\ln(1+\delta L_{NW})}{\sigma-\delta} = \frac{d}{d\sigma}\ln(1+\sigma L_{NW}) = \frac{L_{NW}}{1+\sigma L_{NW}} \tag{4.20}$$

  even for large values of σL_{NW}.

4.5.3 Resistance along a cone-shaped NW with 4 contacts

We consider in this section the case of a uniform cone-shaped NW with resistance given by Eq. 4.10, and r_B=2r_T. For small tapering angle α, we can define the radius $r(L) = r_T(1+\alpha\frac{x}{L})$, and Eq. 4.10 becomes:

$$R_{NW} = \frac{\rho}{\pi}\frac{L}{r_B r_T} = \frac{\rho}{\pi}\frac{L}{r_T^2}\frac{1}{1+\alpha} \tag{4.21}$$

In Fig. 4.17 we have the sketch of the NW with 3 sections:

- In section 1, the length is L/3, and the radius varies between r_T and $r_T(1+\frac{\alpha}{3})$, thus the resistance:

$$R_1 = \frac{\rho}{\pi}\frac{L}{r_T^2}\frac{1}{3}\frac{1}{1+\frac{\alpha}{3}} \tag{4.22}$$

and the ratio with the total resistance is:

$$\frac{R_1}{R_{NW}} = \frac{1}{3}\frac{1+\alpha}{1+\frac{\alpha}{3}} \tag{4.23}$$

- In section 2, the length is L/3 and the radius varies between $r_T(1+\frac{\alpha}{3})$ and $r_T(1+\frac{2\alpha}{3})$, thus the resistance:

$$R_2 = \frac{\rho}{\pi}\frac{L}{r_T^2}\frac{1}{3}\frac{1}{1+\frac{\alpha}{3}}\frac{1}{1+\frac{2\alpha}{3}} \tag{4.24}$$

and the ratio with the total resistance is:

$$\frac{R_2}{R_{NW}} = \frac{1}{3}\frac{1+\alpha}{(1+\frac{\alpha}{3})(1+\frac{2\alpha}{3})} \tag{4.25}$$

- In section 3, the length is L/3 and the radius varies between $r_T(1+\frac{2\alpha}{3})$ and $r_T(1+\alpha)$, thus the resistance:

$$R_3 = \frac{\rho}{\pi}\frac{L}{r_T^2}\frac{1}{3}\frac{1}{1+2\frac{\alpha}{3}}\frac{1}{1+\alpha} \tag{4.26}$$

and the ratio with the total resistance is:

$$\frac{R_3}{R_{NW}} = \frac{1}{3}\frac{1}{1+\frac{2\alpha}{3}} \tag{4.27}$$

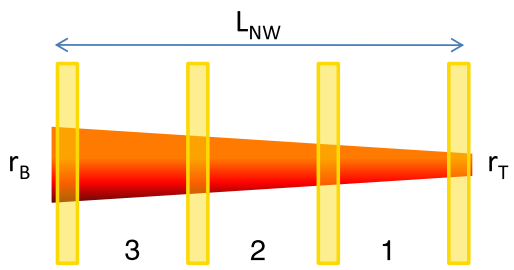

Figure 4.17: Sketch of a cone shape NW with 4 metal contacts.

For instance if we consider $\alpha = 1$, we will find $R_1 = \frac{6}{10}\frac{R_{NW}}{3}$, $R_2 = \frac{9}{10}\frac{R_{NW}}{3}$ and $R_3 = \frac{15}{10}\frac{R_{NW}}{3}$. Note that the value for section 2 is close to $\frac{R_{NW}}{3}$. For α very small, we will find $R_1 = R_2 = R_3 \simeq= \frac{R_{NW}}{3}$. Hence in the following, we will make use of the approximation of cylindrical NW, knowing that this leads to an error of less then 10% considering section 2 of the NW.

4.5.4 Growth conditions of ZnTe/ZnTe:N core/shell NWs

The ZnTe/ZnTe:N NWs prepared for electrical characterization are based on the recipe of sample of Fig. 4.9(b), with a core grown during 1 hour at 375°C (under UHV), and the N doped shell grown during 30 minutes at different temperatures of 290°C, 320°C and 350°C. An undoped sample was also grown at 320°C with the nitrogen flux in the growth chamber with the same pressure as for doping condition, equal to 2.6×10^{-6} Torr, but without plasma.

Fig. 4.18 shows the SEM pictures of the as grown NWs. SEM images of Fig. 4.18(a) and (c) show a similar morphology for the NWs even if the sample shown in (a) was grown without plasma. This confirms that the presence of a high pressure of nitrogen in the growth chamber affects the axial growth of ZnTe NWs.

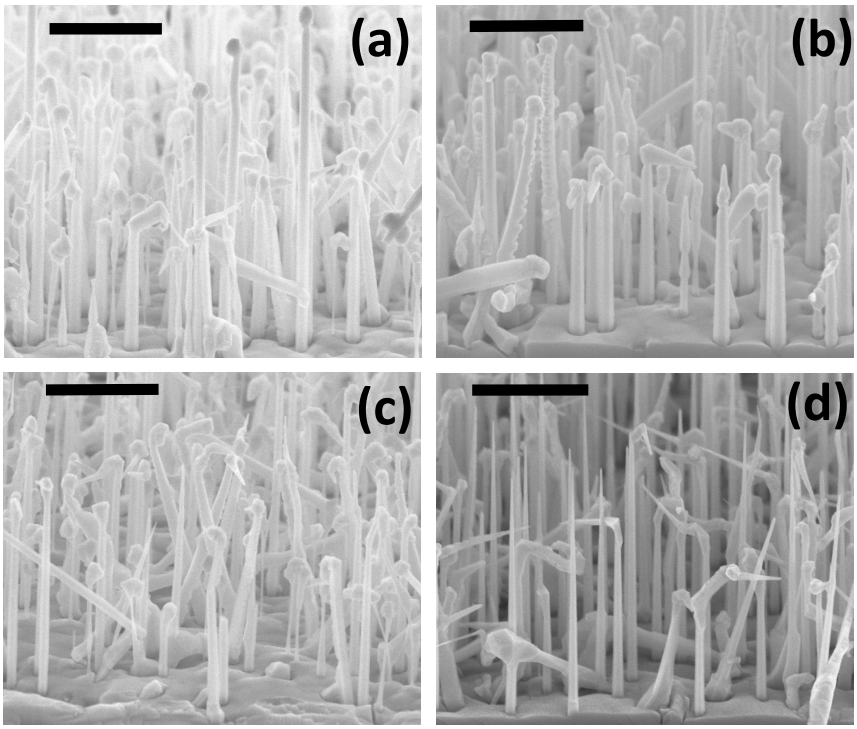

Figure 4.18: SEM images at 65° of ZnTe/ZnTe:N as grown NWs, the core was grown during 1 hour at 375°C with (a) nominally undoped and in presence of nitrogen plasma (RF generator at 450 W and N_2 flux of 0.07 sccm) with growth temperature of (b) 290°C, (c) 320°C, (d) 350°C shell growth temperature. The scale bar is 1μm.

4.5.5 Measurements on the nominally undoped ZnTe NWs reference sample

The devices were measured using the nanoprobe station inside the SEM microscope dedicated to cathodoluminescence (CL) in collaboration with Fabrice Donatini. A SEM image of the chip with the 4 needles is shown in Fig. 4.19. The needles are not on the measurement pads in this picture.

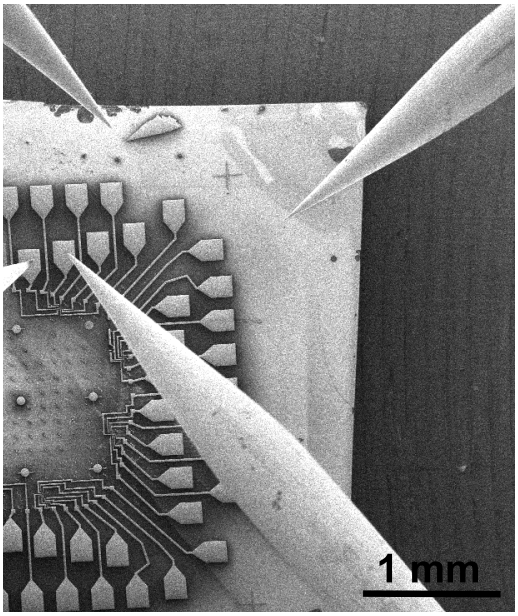

Figure 4.19: SEM image of a NW based device for electrical characterization in the CL setup. 4 needles used for 4-probe measurements are shown.

The reference sample shows a resistance too high to be measured with the 4 probe setup. A SEM picture 4.20 (a) was acquired during the electrical measurements and shows a NW device with an applied bias of 5V between the contacts. The contrast along the NW in Fig. 4.20 (b) shows a linear decrease along the NW. This means that the voltage drop (and the resistance) is uniformly distributed along the NW and there is no Schottky barrier between the NW and the metal contact, otherwise the voltage drop and then the image contrast would have been distributed at the NW-contact region. Note that the current was measured in the pA range and no conduction was observed up to 10V bias (resistance higher then the TΩ).

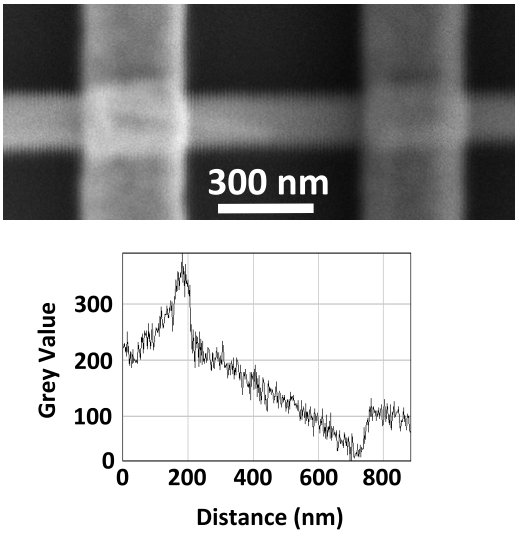

Figure 4.20: (a) SEM picture of a single ZnTe NW device of the undoped sample. A bias of 5V was applied between the contacts. (b) The contrast along the NW exhibits a linear decrease.

4.5.6 Measurements on the ZnTe/ZnTe:N NWs with shell growth temperature of 350°C

The NWs of sample shown in Fig. 4.18 (d) , with the doped shell grown at 350°C, was processed by electron beam lithography (as explained in the fabrication section 4.4) to realize 4 gold contacts for the 4-probe measurements.

The devices were tested at the probe station available at Néel Institute, a set-up for I-V characterization equipped with 2 metal needles used for electrical connection of the external pads. The measurements of the NW characteristics was not possible due to a leakage problem from the oxide caused by the force applied with the measurements needles. Instead it was possible to test the other devices from the same fabrication batch in collaboration with Fabrice Donatini, using the nanoprobe station inside the SEM microscope dedicated to cathodoluminescence (CL). In this case the 4 probes are much thinner and smaller, so less destructive. A SEM image of the chip with the 4 needles is shown in Fig. 4.19.

As explained in section 4.5.2, in the 4-probe method the current is sourced from the two external contacts of the ZnTe NW, while the voltage is measured from the two middle contacts. The set-up is composed of a voltage source to induce a current in the NW using the external contacts, a multi-meter for the current measurement, and another multimeter to measure the voltage from the middle contacts.

In Fig.s 4.21 and 4.22 the result of 2- and 4-probe measurements are shown for 2 different NWs of the same chip.

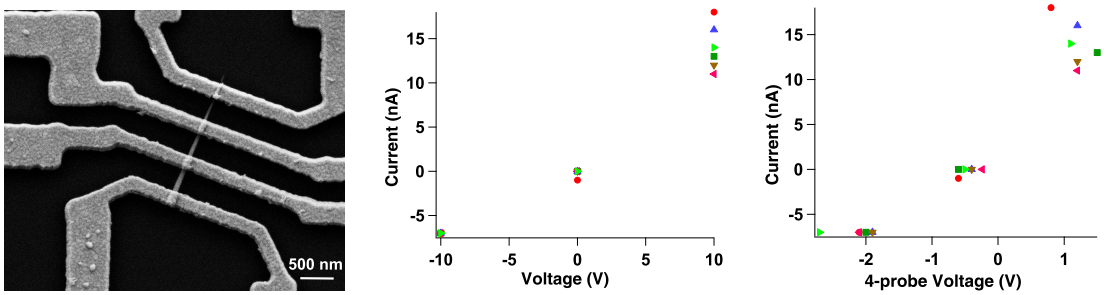

(a) (b) (c)

Figure 4.21: Device C2-NW1 characterization. (a) SEM image of a ZnTe NW with 4 gold contacts acquired after the electrical measurements. (b) I-V characteristics of the device measured between the external contacts acquired at the same time as (c) 4-probe I-V measurements, where the current was sourced between the external contacts and the voltage was acquired from the internal ones.

From the SEM image in Fig. 4.21 (a), acquired after the electrical measurements, we can obtain the dimension of NW1. The NW is cone-shaped with a bottom diameter, as measured close to the metal contact, of 83 nm and a top diameter of 37 nm, and length between the two external contacts of 1.4 μm and between the internal contacts of 330 nm.

Fig. 4.21 (b) shows the results of the 2-probe measurements on NW1. The experimental points are quite dispersed for repeated measurements, but it allows us to estimate the NW1 resistance as R_{TOT}=1.0$\pm$ 0.2 GΩ. The resistance of the middle section of the NW as measured using the 4-probe method, shown in Fig. 4.21 (c), is R_{4p} =0.20$\pm$0.04 GΩ.

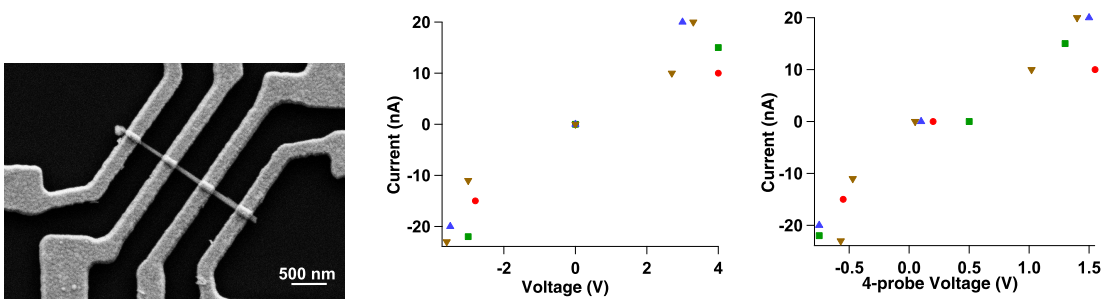

(a) (b) (c)

Figure 4.22: Device C2-NW7 characterization. (a) SEM image of a ZnTe NW with 4 gold contacts acquired after the electrical measurements. (b) I-V characteristics of the device measured between the external contacts acquired at the same time as (c) 4-probe I-V measurements, where the current was sourced between the external contacts and the voltage was acquired from the internal ones.

Similarly from the SEM image in Fig. 4.22(a), also acquired after the electrical measurements, we can obtain the dimension of NW7. The NW is cone-shaped with a bottom diameter, as measured close to the metal contact, of 77 nm and a top diameter of 36 nm, and length between the two external contacts of 1.6 μm and between the internal contacts of 375 nm.

Fig. 4.22 (b) shows the results of the 2-probe measurements on NW7. Again the experimental points are quite dispersed for repeated measurements, but it allows us to estimate the NW7 resistance as R_{TOT} =0.20±0.05 GΩ. The resistance of the middle section of the NW as measured using the 4 probe method, shown in Fig. 4.22 (c), is R_{4p} =0.06±0.01 GΩ.

The resistances found for the two NWs are different by one order of magnitude. Others NWs of the same sample were measured and the value of the resistance was found in the same range.

We can estimate the contact resistance R_c by assuming that the NW resistance is constant along the NW (as discussed in section 4.5.3, for a cone-shaped NW the resistance of the middle section is about 1/3 of the total reristance), using the equation:

$$2R_c + \frac{l_{TOT}}{l_{4p}} R_{4p} = R_{TOT} \tag{4.28}$$

For NW1 we find the contact resistance R_c ≃0.07GΩ while for NW7 R_c ≃0GΩ. Since the width of the contacts is of the same order as their spacing (NW length), we can give another estimate by considering that Eq. 4.6 is no longer valid, and that a significant portion of the current may be transported through the middle contacts rather than the nanowire [76]. We introduce an effective total length $\bar{l}_{TOT} = l_{TOT} - 2l_c$, subtracting the length of the two middle contacts from the NW total length. In this case, from Eq. 4.28 with $\bar{l}_{TOT}$, the effective contact resistance gives an high limit to the value as: for NW1 $\bar{R}_c$ ≤0.2GΩ and for NW7 $\bar{R}_c$ ≤0.01GΩ.

4.5.7 Measurements on the ZnTe/ZnTe:N NWs with shell growth temperature of 290°C

The NWs of sample of Fig. 4.18 (b) with the doped shell grown at 290°C were processed by electron beam lithography as explained in the fabrication section to realize 4 gold contacts for the 4-probe measurements. The measurements were done at INAC in collaboration with NM group. The NW were connected with the measurement set-up using a home-made package (similar to a dual-in-line) and the chip pads were connected to the package using the micro-bonding station at INAC.

From the SEM image in Fig. 4.23 acquired after the electrical measurements, we can obtain the dimension of NW2. The NW is slightly cone-shaped with a bottom diameter, as measured close to the metal contact, of 86 nm and a top diameter of 80 nm, length

between the two external contacts is 1.65 μm and between the internal contacts is 410 nm.

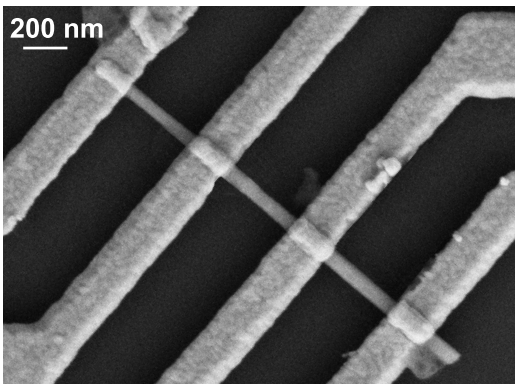

Figure 4.23: SEM image of the device C7-NW2, based on the sample ZnTe/ZnTe:N with the shell grown at 290°C. Gold metal contacts (thickness 160nm) were designed by EBL.

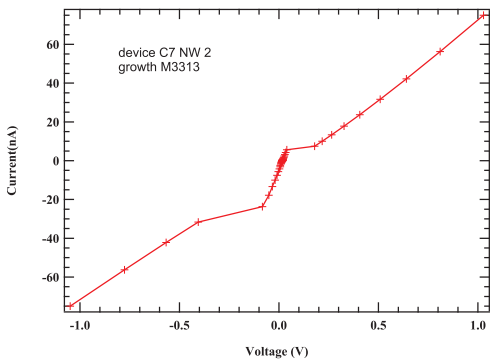

Figure 4.24: I-V curves of device C7-NW2 measured between the external contacts. The change of slope close to zero voltage is an artifact due to the resolution of the multimeter.

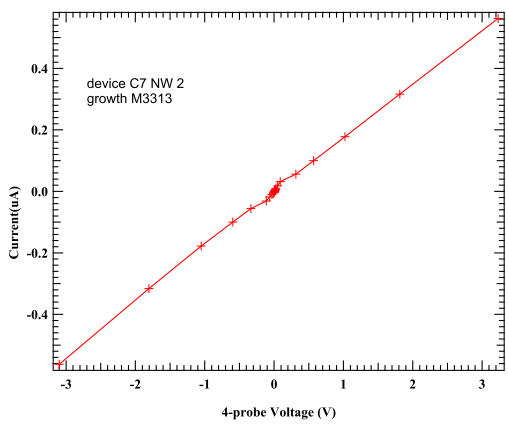

Figure 4.25: 4-probe I-V measurements of device C7-NW2, where the current was sourced between the external contacts and the voltage was acquired from the internal ones.

Fig. 4.24 shows the results of 2-probe measurements where the current was sourced between the external contacts and the corresponding voltage was measured. The change of slope close to zero voltage is an artifact due to the resolution of the multimeter for the voltage measurements. The total resistance (including the contact resistance) is $R_{TOT} = 14 \pm 1M\Omega$. The resistance of the middle section of the NW was measured using the 4-probe method, as shown in Fig. 4.25, where the current was sourced between the external contacts, and the voltage was acquired between the internal ones. The resistance found is $R_{4p} = 5.5 \pm 0.5M\Omega$.

Also in this case, we can estimate the contact resistance R_c by assuming that the NW resistance is constant along the NW (as discussed in section 4.5.3, for a cone-shaped NW the resistance of the middle section is about 1/3 of the total resistance), using Eq. 4.28, with the effective total length $\bar{l}_{TOT} = l_{TOT} - 2l_c$ (from the NW total length, we subtract the length of the two middle contacts, considering that Eq. 4.6 is no longer valid if a significant portion of the current was transported through the middle contacts rather than the nanowire [76]). In this case, from Eq. 4.28 with $\bar{l}_{TOT}$, the effective contact resistance calculated is $0 \pm 2M\Omega$. The contact resistances are probably in the 0.1 M Ω range, and cannot be estimated more precisely.

Fig. 4.26 shows the result of 2-probe measurements at the inner contacts of the NW. The current is sourced between the external contacts and the voltage is measured using a multimeter. The I-V curves are shown as a function of the gate voltage V_g, applied using the back-gate of the device. The current is reduced by increasing the gate voltage, showing a p-type conductivity as expected for nitrogen doping in ZnTe.

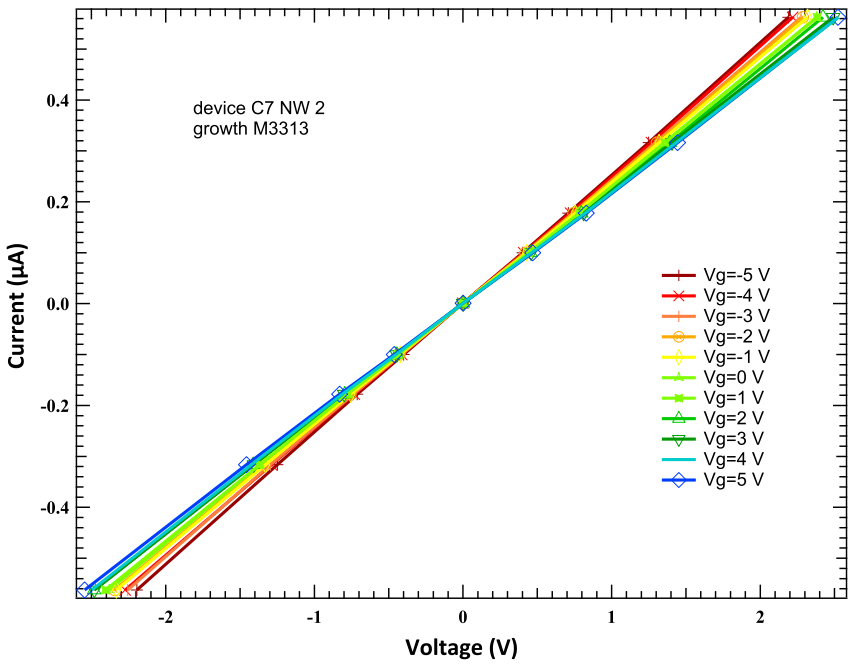

Figure 4.26: I-V curves of device C7-NW2, measured from the inner contacts, as a function of the gate voltage

The threshold voltage V_{th} can be estimated by extrapolation from the measured I-V curves as a function of the gate voltage, as shown in Fig. 4.27. At a drain source voltage of 1.5 V, the threshold voltage can be estimated as 70±5 V.

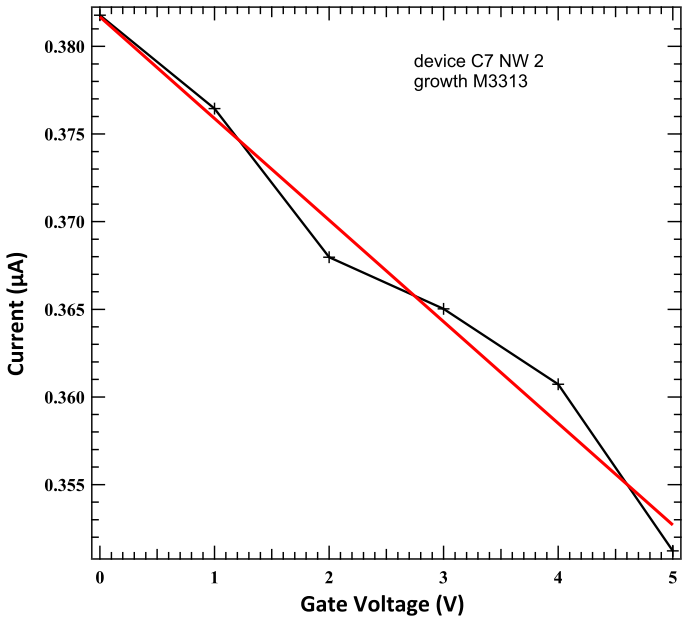

Figure 4.27: Drain source current of device C7-NW2, as a function of the Gate Voltage when the drain source bias is 1.5V

The carrier concentration can be estimated using the model explained in section 4.5.1. From Fig. 4.23, the NW2 is cone-shaped, but the tapering angle is small, we will thus consider the NW as a cylinder with radius r =41.5 nm. As effective length of the channel, I will consider the distance between the internal contacts L =410 nm. The distance between the gate electrode and the center of the NW is $h = 341.5$ nm (the SiO_2 thickness is 300 nm) and ϵ the dielectric constant of the insulating material ($\epsilon = 3.9$ for SiO_2).

According to this model the capacitance per unit length in the back gate geometry:

$$\frac{C}{L} = \frac{2\pi\epsilon\epsilon_0}{\ln(2h/r)} = 8 \times 10^{-11}\text{F/m} \tag{4.29}$$

The total charge Q in the NW:

$$Q = CV_{th} \tag{4.30}$$

where $V_{th} = 70 \pm 5$ V.

From the total charge Q, the carrier density per unit volume can be evaluated as:

$$p = \frac{Q}{e}\frac{1}{\pi r^2 L} = 6 \times 10^{18}\text{holes/cm}^3 \tag{4.31}$$

This value is an estimate in the case in which the charge is distributed uniformly in the NW with a cylinder shape, and is probably underestimated because the doped part of the NW is constituted by its shell. At the moment, we do not dispose of structural

characterization of nitrogen doped NWs. However, we can roughly estimate the shell thickness from the growth recipe as 11 nm, calculated as the difference of the NW radius and the radius of a typical catalyst (about 15 nm, equivalent of the radius of the NW at the beginning of the growth) to obtain the total radial regrowth, this is then divided by 3 since the growth time in presence of nitrogen plasma was 30 minutes over 1 hour and 30 minutes. This would give a factor 1.2 in the calculated carrier density, that is of the same order of magnitude as the value estimated with the uniform cylinder approximation.

Assuming a diffusive transport at room T, the mobility μ can be estimated from the transconductance of the FET in the linear regime, given by:

$$\frac{dI}{dV_G} = \mu(C/L^2)V_{SD} \tag{4.32}$$

We obtain for the mobility μ =0.2 cm^2/Vs. This value is quite low, two orders of magnitude smaller than what found in the reference 2D layer. Other measurements on ZnTe NWs based FET reveal also low mobility: 1.9×10^{-3} cm^2/Vs in Ref. [77], 1 cm^2/Vs in Ref. [15] and 0.11 cm^2/Vs in Ref. [78]. In Ref. [79], the values of the mobility found for n-type GaAs NWs were also small, between 0.2 and 20 cm^2/Vs. In that case, the contact resistance was not taken into account, and typically for GaAs displays a certain variability due to the presence of residual Schottky barriers. In Ref. [80] the mobility of InAs NW-FET is analyzed as a function of temperature and of the surface state of the NWs. They refer to the Hall effect measurements carried out on InAs nanowires [81], [68] showing that immobile interface charge accounts for an appreciable fraction of the total gate-induced charge, meaning that field-effect measurements tend to underestimate the true mobility. The NW surface state is also important, in fact low mobility was observed in nanowires exposed to wet etching conditions [81], [82], [80] probably due to changes in surface states, increased surface roughness, or a combination of the two. In our case, Ar ion etching to remove the native oxide, could have increase the surface roughness of the NWs.

In Appendix B are reported supplementary measurements from the samples of Fig. 4.18, showing the difficulties encountered during electrical characterization. Table 4.1 shows that there is a dependence on the growth temperature for the ZnTe:N shell on the resistance of the devices. This can be interpreted as a dependence of the doping level with the shell growth temperature, but to confirm this, further measurements are required.

4.6 Discussion and conclusion

In summary we have shown that:

- the presence of a nitrogen pressure in the growth chamber affects the morphology of ZnTe NWs: with a delay, we observe the formation of shell and the stop of the axial growth. Better morphology results are obtained with the growth of a ZnTe:N

Sample	resistance range (Ω)
undoped	$>10^{12}$
350°	$1 \div 0.2 \times 10^{9}$
320°C	1×10^{7}
290°C	$1 \div 5 \times 10^{6}$

Table 4.1: Resistance range of measured ZnTe/ZnTe:N NW samples.

shell over an undoped core grown in standard conditions (UHV in the growth chamber, and at substrate temperature of 375°C);

- light emission is preserved for ZnTe/ZnMgTe:N core/shell structures. The interpretation of the luminescence data requires further measurements. This could be a good starting point for modulation doping of CdMnTe QDs;
- electrical measurements on ZnTe/ZnTe:N NWs are challenging. Some devices degrade quite fast for repeated measurements as shown in Appendix B. In Ref. [83], the ZnTe NWs breakdown under Joule heating is studied. No attempt has been done at low temperature. Despite this, table 4.1 shows that there is a dependence on the growth temperature of the ZnTe:N shell on the resistance of the devices;
- the prepared contacts are of good quality and show a Ohmic behavior with very small contact resistances;
- we were able to obtain ZnTe/ZnTe:N(290°C) core/shell NWs and NW-FET room temperature characterization shows a carrier density of 6 $\times 10^{18}$ holes/cm^3. This is slightly smaller than what was found in the 2D ZnTe calibration layers of section 4.2, but of the order of the approximation done on the distribution of the charge (since the entire volume of the NW was considered in the calculation while we know that the core is undoped). The value is probably slightly underestimated, but of the same order as the Mott critical density in ZnTe.

Conclusions and Prospects

The aim of my PhD project was the fabrication of well-controlled, doped II-VI nanowires incorporating CdTe-based quantum dots, the fabrication of contacts and electrical characterization of these II-VI nanowires. The final goal was to incorporate diluted magnetic semiconductors (CdMnTe) and to study the (combined) magneto-optical and transport properties, and the manipulation of these magnetic objects.

At the beginning of this PhD work, it was strongly suspected that the large dispersion of nanowire length which was systematically observed, was due to the presence of an incubation time which was largely responsible of the length dispersion. We could confirm this assumption using a marker technique. Subsequently, we could solve this problem of the incubation time by developing a new process for the formation of the gold nanoparticle which serves as a catalyst for the growth of the nanowires.

It has been shown in Chapter 2 that exposing the gold catalyst to Zn flux during dewetting, is an efficient method to reduce the incubation time difference from NW to NW. A further result is that the method leads to an improvement of the yield of vertical NWs from 20% to 80%.

The experimental results have been analyzed using a diffusion-driven growth model describing the growth. Our growth conditions (low temperature on a ZnTe buffer layer) differ from those of other groups. They imply a growth in the so-called vapor-solid-solid mode (VSS). A usual consequence is the opportunity to form sharp interfaces, as the concentration of elements in the catalyst remains small. A less studied consequence is the formation of a crystalline interface between the nanowire and the nanoparticle. Our preliminary X-ray diffraction study gave further information about the relative orientation between the Au catalysts and the ZnTe(111)B growth substrate. Several orientations are observed but in the presence of Zn, the dominant orientation is parallel to the substrate: this is also the only gold orientation found on top of ZnTe NWs. More detailed studies, both experimental and theoretical (modeling of the Au-ZnTe interface by F. Lançon), are currently performed.

The growth of CdTe QDs is also an important step toward the fabrication of more complicated devices combining magnetic doping (CdMnTe QD) with p-type doping. In particular the control of the ground state wavefunction of the QD (light hole or heavy hole) relies on the possibility to change the aspect ratio L/D. We have shown in Chapter 3 the results of the growth of multi-QD CdTe/ZnTe NWs coupled to a systematic EDX study revealing that in our growth condition the growth temperature has a drastic effect on the growth rate of the CdTe insertions, suppressing completely the growth for a difference of 10°C. The control of the temperature from sample to sample within 10°C limits the reproducibility of the samples. This is very different from the case of ZnTe NWs where the growth temperature range is of several tens of degrees.

To explain the experimental results, we propose a model of the dependence of the CdTe growth rate with temperature, based on the comparison (1) between our system and experimental data on the activity of Cd in solid Au, and (2) with the re-evaporation rate of CdTe from CdTe(100) surfaces as a function of temperature. Further samples with multi-QD CdTe/ZnTe NWs need to be prepared to study the temperature dependence in a lower temperature range to confirm the model. Also, the model by itself must be developed by incorporating the temperature dependence of the Cd content in the nanoparticle, the behavior of Te, the mechanisms of nucleation at the gold-nanowire interface and at the nanowires sidewalls. An important consequence of these results is that our present growth conditions are quite appropriate for the fabrication of CdTe or CdMnTe dots with sharp interfaces and adjustable shape. We must implement a more precise control of the substrate temperature, for instance a system based on the temperature dependence of the gap of the substrate.

Recent samples incorporating a CdTe QD have been grown recently using the processes developed in this PhD work, which exhibit single-photon photoluminescence with no parasitic luminescence due to lateral growth.

We have shown in Chapter 4 that, even if 2D layers of ZnTe(100) are easily doped p-type using nitrogen plasma, the doping of ZnTe NWs using nitrogen is challenging. In particular the nucleation of the NWs is inhibited if the growth is started in presence of nitrogen plasma. Better morphology results are obtained with the growth of a nitrogen doped ZnTe:N shell over an undoped ZnTe core grown in standard conditions (UHV in the growth chamber, and at substrate temperature of 375°C). Indeed the growth is strongly modified in the presence of Nitrogen, up to the point that the nanowires with the wurtzite structure, on which the growth of a shell has proven to be impossible up to now, feature a rapid evolution from totally axial to totally radial growth. Here again, a model of the creation of steps and nucleation islands on the sidewalls has to be developed.

In Chapter 4 we have also shown that electrical measurements on ZnTe/ZnTe:N NWs are challenging due to fast degradation of the NWs. Despite this, we have shown

a dependence of the resistance of the devices on the growth temperature of the ZnTe:N shell. We were able to obtain ZnTe/ZnTe:N(290°C) core/shell NWs and NW-FET room temperature characterization showing a carrier density of 6 $\times 10^{18}$ holes/cm^3, probably underestimated, but of the same order as the Mott critical density in ZnTe. The prepared contacts are of good quality and show a Ohmic behavior with very small contact resistances. There is still a low success rate and dispersion of data probably due to a difference form NW to NW of the same sample or to technical issues.

The growth of electrically doped II-VI nanowires including diluted magnetic semiconductors will open the way towards rather ambitious programs:

- Simultaneous magneto-optical and magneto-transport studies of small magnetic objects: magnetic polarons (resulting from the orientation of the Mn spins by a carrier or an exciton); multi-polarons (involving a small number of carriers) as a magnetic object intermediate between the Mn - exciton single object;
- The manipulation of such objects by an applied bias in a FET structure such as that we have realized;
- Magneto-transport in magnetic ZnMnTe nanowires. The nature of the magnetic order in such a 1D system is an open question, and the transport properties are even more open. This is limited by the doping level that can be achieved in the NWs and on the stability of the material.

Appendices

Appendix A: Gold catalyst size distribution in ZnTe NWs

In this appendix we report a summary on the statistical analysis on the SEM images of the samples of series A of Chapter 2. SEM image of the as grown samples are shown in Fig. 28. The Fig. 29(a) show that when dewetting is done under Zn, the size of the catalyst is lower in average and with a narrower distribution with respect to the vacuum-dewetting case in Fig. 29(e).

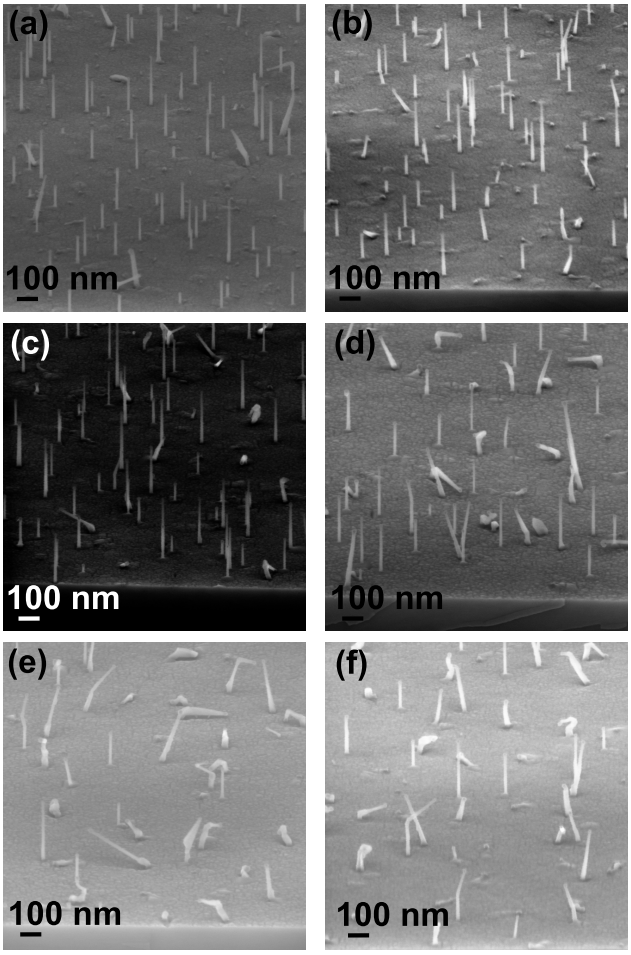

Figure 28: SEM images of the samples of series A of Chapter 2. (a) Zn 0.8 ML/s; (b) Zn 0.4 ML/s; (c) Zn 0.2 ML/s; (d) Zn 0.1 ML/s; (e) vacuum; (f) Te 0.5ML/s.

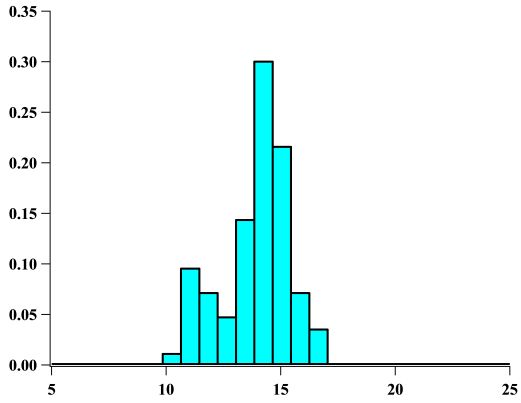

(a) Zn 0.8 (ML/s)

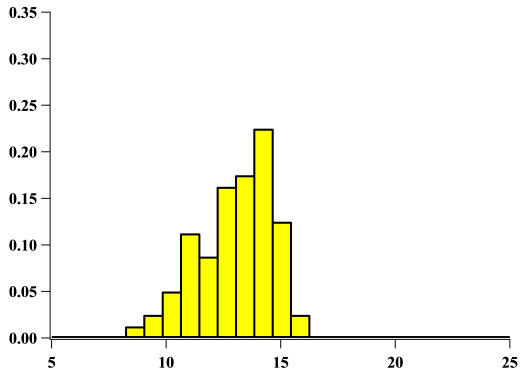

(b) Zn 0.4 (ML/s)

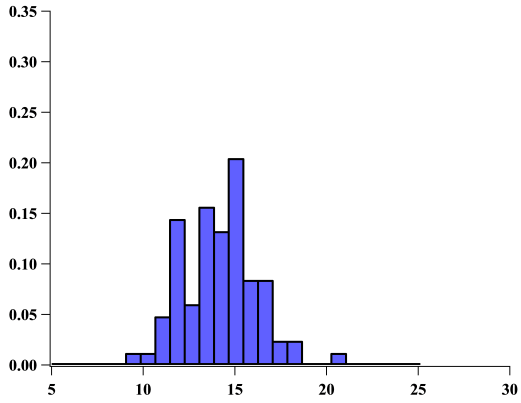

(c) Zn 0.2 (ML/s)

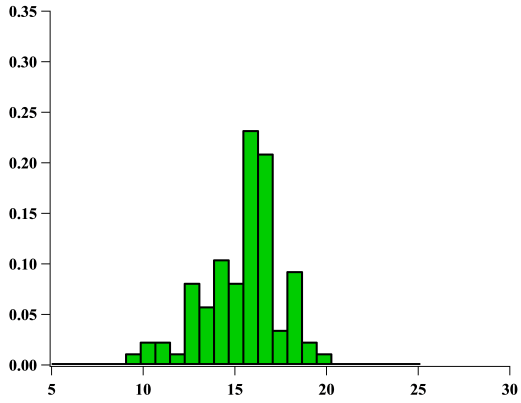

(d) Zn 0.1 (ML/s)

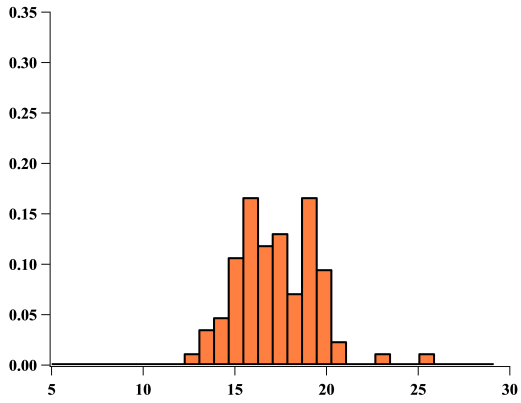

(e) vacuum

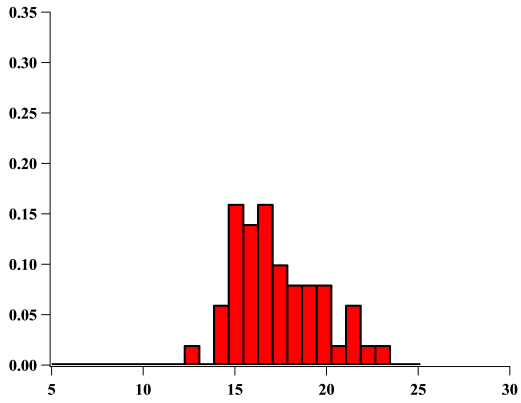

(f) Te 0.5 (ML/s)

Figure 29: Series of histograms showing the evolution of the gold nanoparticle diameter on top of vertical NWs with the dewetting condition, as measured from SEM images. The vertical axis is the normalized to 1 occurrence, while the horizontal axis is the nanoparticle diameter measured in nm.

Appendix B: Difficulties in electrical measurements on ZnTe/ZnTe:N core shell NWs

In this appendix we report about the difficulties encountered during electrical characterization of devices based on ZnTe/ZnTe:N core/shell NW.

Measurements on the ZnTe/ZnTe:N NWs with shell growth temperature of 350°C

Fig. 30 shows results of 4-probe characterization (with needles at CL setup) for a ZnTe/ZnTe:N(350°C) NW showing a diode behavior in the I-V and a big dispersion for repeated measurement.

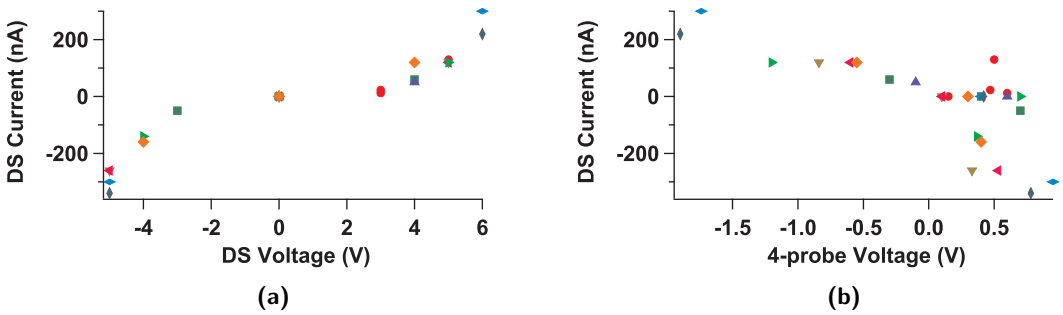

Figure 30: Device C2-NW3 characterization. (a) I-V characteristics of the device measured between the external contacts. (b) results of the 4 probe I-V measurements, where the current was sourced between the external contacts and the voltage was acquired from the internal ones.

Measurements on the ZnTe/ZnTe:N NWs with shell growth temperature of 320°C

Fig. 31 shows results of 2 probe measurements of devices for ZnTe/ZnTe:N(320°C) NWs showing a diode behavior in the I-V. During the test of all the 2-probe I-V (for different couples of contacts) all NWs systematically melted. For instance one of them is shown in Fig. 32.

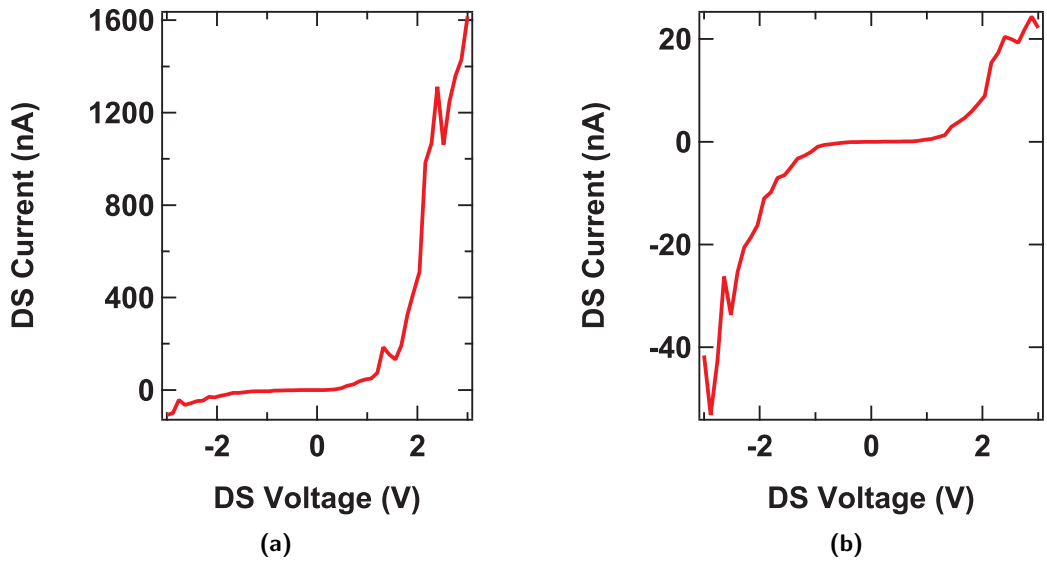

Figure 31: Device

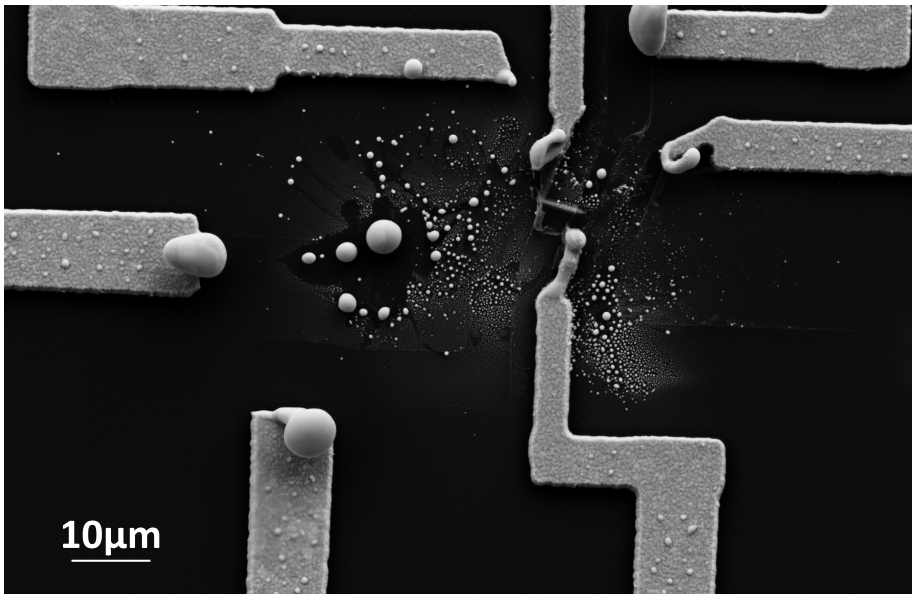

Figure 32: SEM image of a device where the NW (or the metal pads) melted during electrical measurements.

Bibliography

[1] T. Jungwirth, P. Horodyská, N. Tesařová, P. Němec, J. Šubrt, P. Malý, P. Kužel, C. Kadlec, J. Mašek, I. Němec, M. Orlita, V. Novák, K. Olejník, Z. Šobáň, P. Vašek, P. Svoboda, and Jairo Sinova. Systematic Study of Mn-Doping Trends in Optical Properties of (Ga,Mn)As. *Phys. Rev. Lett.*, 105:227201, Nov 2010.

[2] D. Ferrand, J. Cibert, A. Wasiela, C. Bourgognon, S. Tatarenko, G. Fishman, T. Andrearczyk, J. Jaroszyński, S. Koleśnik, T. Dietl, B. Barbara, and D. Dufeu. Carrier-induced ferromagnetism in p-Zn(1-x)Mn(x)Te. *Phys. Rev. B*, 63:085201, Feb 2001.

[3] P. Rueda-Fonseca, E. Bellet-Amalric, R. Vigliaturo, M. den Hertog, Y. Genuist, R. André, E. Robin, A. Artioli, P. Stepanov, D. Ferrand, K. Kheng, S. Tatarenko, and J. Cibert. Structure and morphology in diffusion-driven growth of nanowires: The case of ZnTe. *Nano Lett.*, 14(4):1877–1883, 2014.

[4] P. Stepanov. *Spectroscopie magnéto-optique de nanostructures semiconductrices magnétiques*. PhD thesis, Université de Grenoble, Grenoble, 2013.

[5] G. Bacher, A. Maksimov, H. Schömig, V. Kulakovskii, M. Welsch, A. Forchel, P. Dorozhkin, A. Chernenko, S. Lee, M. Dobrowolska, and J. Furdyna. Monitoring Statistical Magnetic Fluctuations on the Nanometer Scale. *Phys. Rev. Lett.*, 89(12):127201, aug 2002.

[6] T. Clément, D. Ferrand, L. Besombes, H. Boukari, and H. Mariette. Dynamical equilibrium between magnetic ions and photocarriers in low Mn-doped single quantum dots. *Phys. Rev. B*, 81(15):155328, apr 2010.

[7] L. Besombes, K. Kheng, L. Marsal, and H. Mariette. Few-particle effects in single CdTe quantum dots. *Phys. Rev. B*, 65(12):121314, mar 2002.

[8] L. Besombes, Y. Leger, J. Bernos, H. Boukari, H. Mariette, J. P. Poizat, T. Clement, J. Fernández-Rossier, and R. Aguado. Optical probing of spin fluctuations of a

single paramagnetic Mn atom in a semiconductor quantum dot. *Phys. Rev. B*, 78:125324, Sep 2008.

[9] A. Artioli. *Magnetic Magnetic Polaron in (Cd,Mn)Te quantum dot inserted in ZnTe nanowire*. PhD thesis, Université Grenoble Alpes, Grenoble, 2016.

[10] P. Rueda-Fonseca. *Magnetic quantum dots in II-VI semiconductor nanowires*. PhD thesis, Université Grenoble Alpes, Grenoble, 2015.

[11] M. Szymura, Ł .Klopotowski, P. Wojnar, G. Karczewski, T. Wojtowicz, and J. Kossut. Identifcation of Optical Transitions from CdTe and CdMnTe Quantum Dots Embedded in ZnTe Nanowires. *ACTA PHYSICA POLONICA A*, 124(5), 2013.

[12] Keivan Devami, Daegun Kang, Jeong-Soo Lee, and M. Meyyappan. Synthesis of ZnTe nanostructures by vapor–liquid–solid technique. *Chemical Physics Letters*, 504(1):62 – 66, 2011.

[13] Qingfang Meng, Chuanbin Jiang, and Scott X. Mao. Temperature-dependent growth of zinc-blende-structured ZnTe nanostructures. *Journal of Crystal Growth*, 310(20):4481 – 4486, 2008.

[14] So Ra Moon, Jung Hyuk Kim, and Yong Kim. Znte nanowires with oxygen intermediate band grown by bismuth-catalyzed physical vapor transport. *The Journal of Physical Chemistry C*, 116(18):10368–10374, 2012.

[15] H B Huo, L Dai, C Liu, L P You, W Q Yang, R M Ma, G Z Ran, and G G Qin. Electrical properties of Cu doped p-ZnTe nanowires. *Nanotechnology*, 17(24):5912, 2006.

[16] Zhong Li, Joseph Salfi, Christina De Souza, Ping Sun, Selvakumar V. Nair, and Harry E. Ruda. Room temperature single nanowire znte photoconductors grown by metal-organic chemical vapor deposition. *Applied Physics Letters*, 97(6):063510, 2010.

[17] K.B. Kahen, Irene A. Goldthorpe, and John Minter. Low temperature ii–vi nanowire growth using au–sn catalysts. *Journal of Crystal Growth*, 322(1):57 – 62, 2011.

[18] Liang Li, Youwen Yang, Xiaohu Huang, Guanghai Li, and Lide Zhang. Fabrication and characterization of single-crystalline znte nanowire arrays. *The Journal of Physical Chemistry B*, 109(25):12394–12398, 2005.

[19] E. Janik, J. Sadowski, P. Dłużewski, S. Kret, L. T. Baczewski, A. Petroutchik, E. Łusakowska, J. Wróbel, W. Zaleszczyk, G. Karczewski, T. Wojtowicz, and A. Presz. Znte nanowires grown on gaas(100) substrates by molecular beam epitaxy. *Applied Physics Letters*, 89(13):133114, 2006.

[20] E Janik, P Dłużewski, S Kret, A Presz, H Kirmse, W Neumann, W Zaleszczyk, L T Baczewski, A Petroutchik, E Dynowska, J Sadowski, W Caliebe, G Karczewski, and T Wojtowicz. Catalytic growth of ZnTe nanowires by molecular beam epitaxy: structural studies. *Nanotechnology*, 18(47):475606, 2007.

[21] Valentina Zannier, Faustino Martelli, Vincenzo Grillo, Jasper R. Plaisier, Andrea Lausi, and Silvia Rubini. Strong blue emission from ZnSe nanowires grown at low temperature. *physica status solidi (RRL) – Rapid Research Letters*, 8(2):182–186, 2014.

[22] Piotr Wojnar, Elżbieta Janik, Lech T. Baczewski, Sławomir Kret, Elżbieta Dynowska, Tomasz Wojciechowski, Jan Suffczyński, Joanna Papierska, Piotr Kossacki, Grzegorz Karczewski, Jacek Kossut, and Tomasz Wojtowicz. Giant spin splitting in optically active ZnMnTe/ZnMgTe core/shell nanowires. *Nano Letters*, 12(7):3404–3409, 2012.

[23] Vladimir G Dubrovskii, Alexey D Bolshakov, Benjamin L Williams, and Ken Durose. Growth modeling of CdTe nanowires. *Nanotechnology*, 23(48):485607, 2012.

[24] M. Kessel, J. Hajer, G. Karczewski, C. Schumacher, C. Brüne, H. Buhmann, and L. W. Molenkamp. CdTe-HgTe core-shell nanowire growth controlled by RHEED. *arXiv*, arXiv:1703.09106, 2017.

[25] Piotr Wojnar, Elżbieta Janik, Lech T. Baczewski, Sławomir Kret, G. Karczewski, Tomasz Wojtowicz, Mateusz Goryca, Tomasz Kazimierczuk, and Piotr Kossacki. Growth and optical properties of CdTe quantum dots in ZnTe nanowires. *Applied Physics Letters*, 99(11):113109, 2011.

[26] P. Wojnar, J. Plachta, W. Zaleszczyk, S. Kret, Ana M. Sanchez, R. Rudniewski, K. Raczkowska, M. Szymura, G. Karczewski, L. T. Baczewski, A. Pietruczik, T. Wojtowicz, and J. Kossut. Coexistence of optically active radial and axial CdTe insertions in single ZnTe nanowire. *Nanoscale*, 8:5720–5727, 2016.

[27] M. I. den Hertog. *Characterization of silicon nanowires by transmission electron microscopy*. PhD thesis, Université Joseph-Fourier, Grenoble, 2009.

[28] Martien I. den Hertog, Heinz Schmid, David Cooper, Jean-Luc Rouviere, Mikael T. Björk, Heike Riel, Pierrette Rivallin, Siegfried Karg, and Walter Riess. Mapping active dopants in single silicon nanowires using off-axis electron holography. *Nano Letters*, 9(11):3837–3843, 2009.

[29] M. Watanabe and D. B. Williams. The quantitative analysis of thin specimens: a review of progress from the Cliff-Lorimer to the new ζ-factor methods. *Journal of Microscopy*, 221(2):89–109, 2006.

[30] P. Rueda-Fonseca, E. Robin, E. Bellet-Amalric, M. Lopez-Haro, M. Den Hertog, Y. Genuist, R. André, A. Artioli, S. Tatarenko, D. Ferrand, and J. Cibert. Quantitative reconstructions of 3D chemical nanostructures in nanowires. *Nano Letters*, 16(3):1637–1642, 2016. PMID: 26837636.

[31] P. Rueda-Fonseca, M. Orrù, E. Bellet-Amalric, E. Robin, M. Den Hertog, Y. Genuist, R. André, S. Tatarenko, and J. Cibert. Diffusion-driven growth of nanowires by low-temperature molecular beam epitaxy. *J. Appl. Phys.*, 119(16), 2016.

[32] H. Okamoto and T. B. Massalski. *Binary Alloy Phase Diagrams*. 1984.

[33] Frank Glas. Critical dimensions for the plastic relaxation of strained axial heterostructures in free-standing nanowires. *Phys. Rev. B*, 74:121302, Sep 2006.

[34] V. G. Dubrovskiĭ, N. V. Sibirev, R. A. Suris, G. É. Cirlin, V. M. Ustinov, M. Tchernysheva, and J. C. Harmand. The role of surface diffusion of adatoms in the formation of nanowire crystals. *Semiconductors*, 40(9):1075–1082, 2006.

[35] V. G. Dubrovskii, N. V. Sibirev, G. E. Cirlin, I. P. Soshnikov, W. H. Chen, R. Larde, E. Cadel, P. Pareige, T. Xu, B. Grandidier, J.-P. Nys, D. Stievenard, M. Moewe, L. C. Chuang, and C. Chang-Hasnain. Gibbs-Thomson and diffusion-induced contributions to the growth rate of Si, InP, and GaAs nanowires. *Phys. Rev. B*, 79:205316, May 2009.

[36] S. Breuer, M. Hilse, A. Trampert, L. Geelhaar, and H. Riechert. Vapor-liquid-solid nucleation of GaAs on Si(111): Growth evolution from traces to nanowires. *Phys. Rev. B*, 82:075406, Aug 2010.

[37] F. Dhalluin, T. Baron, P. Ferret, B. Salem, P. Gentile, and J.-C. Harmand. Silicon nanowires: Diameter dependence of growth rate and delay in growth. *Appl. Phys. Lett.*, 96(13), 2010.

[38] Colm O'Regan, Subhajit Biswas, Curtis O'Kelly, Soon Jung Jung, John J. Boland, Nikolay Petkov, and Justin D. Holmes. Engineering the growth of germanium nanowires by tuning the supersaturation of Au/Ge binary alloy catalysts. *Chem. Mat.*, 25(15):3096–3104, 2013.

[39] Prasana Sahoo, Sandip Dhara, S. Amirthapandian, and M. Kamruddin. Evolution of GaN nanowire morphology during catalyst-induced growth process. *J. Mater. Chem. C*, 1:7237–7245, 2013.

[40] F. Jabeen, G. Patriarche, F. Glas, and J.-C. Harmand. GaP/$GaAs_{1-x}P_x$ nanowires fabricated with modulated fluxes: A step towards the realization of superlattices in a single nanowire. *Journal of Crystal Growth*, 323(1):293 – 296, 2011.

[41] Faebian Bastiman, Hanno Küpers, Claudio Somaschini, and Lutz Geelhaar. Growth map for Ga-assisted growth of GaAs nanowires on Si(111) substrates by molecular beam epitaxy. *Nanotechnology*, 27(9):095601, 2016.

[42] M. Orrù, M. den Hertog, E. Robin, Y. Genuist, R. André, J. Cibert, and E. Bellet-Amalric. Control of the incubation time in the vapor-solid-solid growth of semiconductor nanowires. *Applied Physics Letters*, 110(26):263107, 2017.

[43] P Wojnar, J Płachta, S Kret, A Kaleta, W Zaleszczyk, M Szymura, M Wiater, L T Baczewski, A Pietruczik, G Karczewski, T Wojtowicz, and J Kossut. Growth and optical investigations of high quality individual CdTe/(Cd,Mg)Te core/shell nanowires. *Nanotechnology*, 28(4):045207, 2017.

[44] R. Daudin, T. Nogaret, T. U. Sch´ulli, N. Jakse, A. Pasturel, and G. Renaud. Epitaxial orientation changes in a dewetting gold film on Si(111). *Phys. Rev. B*, 86:094103, Sep 2012.

[45] Faebian Bastiman, Hanno Küpers, Claudio Somaschini, and Lutz Geelhaar. Growth map for Ga-assisted growth of GaAs nanowires on Si (111) substrates by molecular beam epitaxy. *Nanotechnology*, 27(9):95601, 2016.

[46] Yann-Michel Niquet and Dulce Camacho Mojica. Quantum dots and tunnel barriers in InAs/InP nanowire heterostructures: Electronic and optical properties. *Phys. Rev. B*, 77:115316, 2008.

[47] M. Zielinski. Fine structure of light-hole excitons in nanowire quantum dots. *Phys. Rev. B*, 88:115424, Sep 2013.

[48] Giacomo Priante, Gilles Patriarche, Fabrice Oehler, Frank Glas, and Jean-Christophe Harmand. Abrupt GaP/GaAs interfaces in self-catalyzed nanowires. *NanoLetters*, 15:6036, 2015.

[49] Giacomo Priante, Frank Glas, Gilles Patriarche, Konstantinos Pantzas, Fabrice Oehler, and Jean-Christophe Harmand. Sharpening the interfaces of axial heterostructures in self-catalyzed AlGaAs nanowires: Experiment and theory. *NanoLetters*, 16:1917, 2016.

[50] C.-Y. Wen, M. C. Reuter, J. Bruley, J. Tersoff, S. Kodambaka, E. A. Stach, and F. M. Ross. Formation of compositionally abrupt axial heterojunctions in silicon-germanium nanowires. *Science*, 326(5957):1247–1250, 2009.

[51] Mathieu Jeannin, Alberto Artioli, Pamela Rueda-Fonseca, Edith Bellet-Amalric, Kuntheak Kheng, Régis André, Serge Tatarenko, Joel Cibert, David Ferrand, and Gilles Nogues. Light-hole exciton in a nanowire quantum dot. *Phys. Rev. B*, 95:035305, Jan 2017.

[52] M. Jeannin. *Control of the emission properties of semiconducting nanowire quantum dots using plasmonic nanoantennas*. PhD thesis, Université Grenoble Alpes, Grenoble, 2016.

[53] J. D. Filby and J. N. Pratt. Thermodynamic measurements on gold + cadmium liquid and solid solutions. *Trans. Faraday Soc.*, 60:1934–1940, 1964.

[54] L. J. Bartha and W. A. Alexander. The thermodynamic properties and phase diagram of the gold-cadmium system by the isopiestic method. *Canadian Journal of Chemistry*, 43(8):2319–2327, 1965.

[55] A. Arnoult and J. Cibert. Surface dynamics during CdTe growth by molecular beam epitaxy. *Applied Physics Letters*, 66(18):2397–2399, 1995.

[56] Alberto Pimpinelli and Philippe Peyla. Deposition and growth with desorption in molecular-beam epitaxy. *Journal of Crystal Growth*, 183(3):311 – 322, 1998.

[57] C. Bodin, J. Cibert, W. Grieshaber, Le Si Dang, F. Marcenat, A. Wasiela, P. H. Jouneau, G. Feuillet, D. Hervé, and E. Molva. Growth, structural, and optical properties of II-VI layers: (001) CdMnTe grown by molecular-beam epitaxy. *Journal of Applied Physics*, 77(3):1069–1081, 1995.

[58] P. Dluzewski, E. Janik, S. Kret, W. Zaleszczyk, D. Tang, G. Karczewski, and T. Wojtowicz. Tem characterization of mbe grown CdTe/ZnTe axial nanowires. *Journal of Microscopy*, 237(3):337–340, 2010.

[59] H. Kirmse, I. Häusler, S. Kret, E. Janik, G. Karczewski, and T. Wojtowicz. Tem analysis of the container effect of au-based catalyst droplets during vapour-liquid-solid growth of axial znte/cdte nanowires. *Crystal Research and Technology*, 44(10):1047–1053, 2009.

[60] M. Grün, A. Haury, J. Cibert, and A. Wasiela. The nitrogen acceptor energy in ZnTe measured by Hall effect and optical spectroscopy. *Journal of Applied Physics*, 79(9):7386–7388, 1996.

[61] S. Suomalainen, T. V. Hakkarainen, T. Salminen, R. Koskinen, M. Honkanen, E. Luna, and Mircea Guina. Te-doping of self-catalyzed gaas nanowires. *Applied Physics Letters*, 107(1):012101, 2015.

[62] Leonardo Viti, Miriam S. Vitiello, Daniele Ercolani, Lucia Sorba, and Alessandro Tredicucci. Se-doping dependence of the transport properties in CBE-grown InAs nanowire field effect transistors. *Nanoscale Research Letters*, 7(1):159, Feb 2012.

[63] S. Wirths, M. Mikulics, P. Heintzmann, A. Winden, K. Weis, Ch. Volk, K. Sladek, N. Demarina, H. Hardtdegen, D. Grützmacher, and Th. Schäpers. Preparation of ohmic contacts to GaAs/AlGaAs-core/shell-nanowires. *Applied Physics Letters*, 100(4):042103, 2012.

[64] Tuanwei Shi, Mengqi Fu, Dong Pan, Yao Guo, Jianhua Zhao, and Qing Chen. Contact properties of field-effect transistors based on indium arsenide nanowires thinner than 16 nm. *Nanotechnology*, 26(17):175202, 2015.

[65] Ravi Agrawal, Rodrigo A. Bernal, Dieter Isheim, and Horacio D. Espinosa. Characterizing atomic composition and dopant distribution in wide band gap semiconductor nanowires using laser-assisted atom probe tomography. *The Journal of Physical Chemistry C*, 115(36):17688–17694, 2011.

[66] Sichao Du, Timothy Burgess, Baptiste Gault, Qiang Gao, Peite Bao, Li Li, Xiangyuan Cui, Wai Kong Yeoh, Hongwei Liu, Lan Yao, Anna V. Ceguerra, Hark Hoe Tan, Chennupati Jagadish, Simon P. Ringer, and Rongkun Zheng. Quantitative dopant distributions in GaAs nanowires using atom probe tomography. *Ultramicroscopy*, 132:186 – 192, 2013. IFES 2012.

[67] Olof Hultin, Gaute Otnes, Lars Samuelson, and Kristian Storm. Simplifying nanowire hall effect characterization by using a three-probe device design. *Nano Letters*, 17(2):1121–1126, 2017.

[68] Ch. Blömers, T. Grap, M. I. Lepsa, J. Moers, St. Trellenkamp, D. Grützmacher, H. Lüth, and Th. Schäpers. Hall effect measurements on InAs nanowires. *Applied Physics Letters*, 101(15):152106, 2012.

[69] K. Storm, F. Halvardsson, M. Heurlin, D. Lindgren, A. Gustafsson, P. M. Wu, B. Monemar, and L. Samuelson. Spatially resolved Hall effect measurement in a single semiconductor nanowire. *Nature Nanotechnology*, 7:718–722, 2012.

[70] L. J. van der Pauw. A method of measuring specific resistivity and Hall effect of discs of arbitrary shape. *Philips Res.Rep*, 13(1), 1958.

[71] D Ferrand, J Cibert, C Bourgognon, S Tatarenko, A Wasiela, G Fishman, A Bonanni, H Sitter, S Koleśnik, J Jaroszyński, A Barcz, and T Dietl. Carrier-induced ferromagnetic interactions in p-doped Zn(1-x)Mn(x)Te epilayers. *Journal of Crystal Growth*, 214:387 – 390, 2000.

[72] P. Wojnar, M. Zielinski, E. Janik, W. Zaleszczyk, T. Wojciechowski, R. Wojnar, M. Szymura, Ł. Kłopotowski, L. T. Baczewski, A. Pietruchik, M. Wiater, S. Kret, G. Karczewski, T. Wojtowicz, and J. Kossut. Strain-induced energy gap variation in znte/znmgte core/shell nanowires. *Applied Physics Letters*, 104(16):163111, 2014.

[73] S. M. Sze. *Physics of Semiconductor Devices*. second edition, John Wiley & Sons, 1981.

[74] R. Martel, T. Schmidt, H. R. Shea, T. Hertel, and Ph. Avouris. Single- and multi-wall carbon nanotube field-effect transistors. *Applied Physics Letters*, 73(17):2447–2449, 1998.

[75] Olaf Wunnicke. Gate capacitance of back-gated nanowire field-effect transistors. *Applied Physics Letters*, 89(8):083102, 2006.

[76] S.E. Mohney, Y. Wang, M.A. Cabassi, K.K. Lew, S. Dey, J.M. Redwing, and T.S. Mayer. Measuring the specific contact resistance of contacts to semiconductor nanowires. *Solid-State Electronics*, 49(2):227 – 232, 2005.

[77] Y. L. Cao, Y. B. Tang, Y. Liu, Z. T. Liu, L. B. Luo, Z. B. He, J. S. Jie, R. Vellaisamy, W. J. Zhang, C. S. Lee, and S. T. Lee. Coaxial nanocables of p-type zinc telluride nanowires sheathed with silicon oxide: synthesis, characterization and properties. *Nanotechnology*, 20:455702, 2009.

[78] Shanying Li, Yang Jiang, Di Wu, Binbin Wang, Yugang Zhang, Junwei Li, Xinmei Liu, Honghai Zhong, Lei Chen, and Jiansheng Jie. Structure and electrical properties of p-type twin ZnTe nanowires. *Appl. Phys. A*, 102:469–475, 2011.

[79] Marta Orrù, Eva Repiso, Stefania Carapezzi, Alex Henning, Stefano Roddaro, Alfonso Franciosi, Yossi Rosenwaks, Anna Cavallini, Faustino Martelli, and Silvia Rubini. A Roadmap for Controlled and Efficient n-Type Doping of Self-Assisted GaAs Nanowires Grown by Molecular Beam Epitaxy. *Advanced Functional Materials*, 26:2836–2845, 2016.

[80] Nupur Gupta, Yipu Song, Gregory W Holloway, Urbasi Sinha, Chris M Haapamaki, Ray R LaPierre, and Jonathan Baugh. Temperature-dependent electron mobility in inas nanowires. *Nanotechnology*, 24(22):225202, 2013.

[81] Kristian Storm, Gustav Nylund, Lars Samuelson, and Adam P. Micolich. Realizing lateral wrap-gated nanowire fets: Controlling gate length with chemistry rather than lithography. *Nano Letters*, 12(1):1–6, 2012.

[82] Sajal Dhara, Shamashis Sengupta, Hari S. Solanki, Arvind Maurya, Arvind Pavan R., M. R. Gokhale, Arnab Bhattacharya, and Mandar M. Deshmukh. Facile fabrication of lateral nanowire wrap-gate devices with improved performance. *Applied Physics Letters*, 99(17):173101, 2011.

[83] Keivan Davami, Hessam M Ghassemi, Reza S Yassar, and Jeong-soo Lee. Thermal Breakdown of ZnTe Nanowires. *ChemPhysChem*, 13:347–352, 2012.

Index

M3121, 39
M3176, 77
M3194, 21, 22, 26, 28, 29, 46, 49, 51, 52, 64
M3203, 77
M3216, 78
M3217, 79
M3218, 79
M3262, 19, 25
M3265, 84–86
M3275, 32, 112
M3277, 32, 39, 112
M3278, 32, 112
M3279, 32, 112
M3280, 32
M3283, 32, 112
M3284, 32, 112
M3285, 81–83
M3286, 82
M3287, 81–83
M3288, 81–83
M3301, 84, 87, 89, 95–98, 113
M3302, 84, 87, 89
M3308, 20, 39
M3309, 39
M3311, 88, 89, 95, 97
M3312, 95
M3313, 95, 99–102
M3330, 48, 49, 62–64
M3372, 46, 47, 54, 55, 57–59, 64, 65, 71

Abstract: Semiconductor nano-spintronics requires combining magnetism and nanoelectronics functions into a single semiconductor nanostructure. An attractive method consists in preparing diluted magnetic semiconductors (DMS), where hole-mediated ferromagnetism appears with p-type doping. II-VI DMS allow to control separately the carriers and the Mn concentrations, since the Mn ions are not electrical dopants. II-VI semiconductor nanowires (NWs) are a model system offering the possibility to engineer the wavefunction and the strain in well-chosen heterostructures containing the magnetic impurities. This requires an optimal growth of NW-based heterostructures, and the possibility to control the doping level, which is a major challenge in present NW research.
In this context, my PhD project has been devoted to three main investigation axis: the growth by molecular beam epitaxy (MBE) of Au-catalyzed ZnTe NWs, the control of the aspect ratio of CdTe quantum dots (QDs) embedded in ZnTe NWs, and the nitrogen doping of ZnTe NW.
Concerning the growth of ZnTe NWs, the problem of an incubation time different from NW to NW has been studied using a marker technique. A new method involving the preparation of Au catalyst under Zn flux has been demonstrate to efficiently suppress differences in the incubation times, reducing the length dispersion in the same sample from a factor of 10 to 2 and giving a yield of vertical NWs of 80% instead of 20%.
Complementary XRD experiments gave further information about the relative orientation between the Au catalysts and the ZnTe(111)B growth substrate.
The aspect ratio of CdTe QDs is an important way to control the QD ground state (between light hole and heavy hole). This can be achieved by changing the growth time of the QDs, but requires (1) the suppression of the lateral growth (giving parasitic QDs) and (2) reproducibility from a sample to another which relies on a precise control of the growth temperature within 10°C. This was demonstrated in our growth conditions with a coupled study of growth of multi-QD-NW CdTe-ZnTe heterostructures and TEM and EDX characterization.
Then the results of the growth by molecular beam epitaxy and characterization of nitrogen doped ZnTe/ZnTe:N core/shell NWs will be presented. Single NW based field effect transistor were realized by electron beam lithography for electrical characterization. We were able to obtain ZnTe/ZnTe:N core/shell NWs showing a p-type carrier density of 6×10^{18} holes/cm^3 at room temperature, of the same order as the Mott critical density in ZnTe.

Résumé: La nanospintronique basée sur les semi-conducteurs implique la combinaison des fonctions nanoélectroniques et magnétiques au sein d'une nanostructure unique. Une méthode intéressante consiste en la préparation d'un semi-conducteur magnétique dilué (DMS), dans lequel le ferromagnétisme induit par les trous est obtenu par le dopage de type P. Les DMS II-VI permettent de contrôler séparément les porteurs et la concentration du Mn, puisque les ions de Mn ne sont pas des dopants électriques. Les nanofils (NW) de semi-conducteurs II-VI représentent un système modèle permettant de concevoir la fonction d'onde et la déformation au sein d'hétérostructures parfaitement contrôlées et contenant les impuretés magnétiques. Ceci nécessite une croissance optimale d'hétérostructures dans la géométrie des nanofils et un contrôle précis du niveau du dopant, ce qui constitue une des difficultés majeures dans l'état actuel des recherches.
Dans ce contexte, mon travail de Thèse s'est focalisé sur trois principaux axes de recherche : la croissance par épitaxie par jets moléculaires de nanofils de ZnTe catalysés par nanoparticules d'Au, la maîtrise du rapport de forme des boites quantiques de CdTe insérées dans les fils de ZnTe, et le dopage azote des fils de ZnTe.
Concernant la croissance des fils de ZnTe, le problème de la variabilité des temps d'incubation d'un fil à l'autre a été étudié à l'aide de la technique des marqueurs. Une nouvelle méthode basée sur la préparation du catalyseur d'Au sous flux de Zn a démontré son efficacité dans la suppression de variabilité des temps d'incubation, réduisant la dispersion des longueurs sur un même échantillon d'un facteur 10 à un facteur 2, et augmentant le taux de succès des fils verticaux de 20% à 80%. Des mesures complémentaires de diffraction des rayons X ont fourni des informations supplémentaires sur l'importance de l'orientation relative entre le catalyseur d'Au et le substrat ZnTe(111)B.
Le rapport de forme des boites quantiques de CdTe est un moyen pour maîtriser leur état fondamental (entre trou léger et trou lourd). Ceci peut être obtenu en contrôlant le temps de croissance des boite quantiques, mais demande (1) la suppression de la croissance latérale (responsable de la formation de boites parasites) et (2) la reproductibilité d'un échantillon à l'autre, basée sur une maîtrise de la température de croissance avec une précision meilleure que 10 degrés. Ceci a été validé dans nos conditions de croissance par une étude croisée de croissance d'heterostructures de ZnTe avec multiples boites quantiques de CdTe et de caractérisation par microscopie électronique.
Je présenterai les résultats des croissances par épitaxie par jets moléculaires et des caractérisations des nanofils de ZnTe /ZnTe:N cœur/coquille avec dopage azoté. Des transistors à effet de champ basé sur des nanofils isolés ont été fabriqués pour la caractérisation électrique. Nous avons obtenu des fils de ZnTe/ZnTe:N cœur/coquille présentant des densités de charges de 6×10^{18} trous/ cm^3 à température ambiante, du même ordre que la densité critique de Mott pour le ZnTe.